

Air Force Institute of Technology

AFIT Scholar

---

Theses and Dissertations

Student Graduate Works

---

6-9-2008

## Laser-Induced Fluorescence and Performance Analysis of the Ultra-Compact Combustor

Patrick J. Lakusta

Follow this and additional works at: <https://scholar.afit.edu/etd>



Part of the [Heat Transfer, Combustion Commons](#), and the [Propulsion and Power Commons](#)

---

### Recommended Citation

Lakusta, Patrick J., "Laser-Induced Fluorescence and Performance Analysis of the Ultra-Compact Combustor" (2008). *Theses and Dissertations*. 2668.

<https://scholar.afit.edu/etd/2668>

This Thesis is brought to you for free and open access by the Student Graduate Works at AFIT Scholar. It has been accepted for inclusion in Theses and Dissertations by an authorized administrator of AFIT Scholar. For more information, please contact [richard.mansfield@afit.edu](mailto:richard.mansfield@afit.edu).



**LASER-INDUCED FLUORESCENCE AND PERFORMANCE  
ANALYSIS OF THE ULTRA-COMPACT COMBUSTOR**

THESIS

Patrick J. Lakusta, Ensign, USN

AFIT/GAE/ENY/08-J03

**DEPARTMENT OF THE AIR FORCE  
AIR UNIVERSITY  
***AIR FORCE INSTITUTE OF TECHNOLOGY*****

---

**Wright-Patterson Air Force Base, Ohio**

APPROVED FOR PUBLIC RELEASE; DISTRIBUTION UNLIMITED

The views expressed in this thesis are those of the author and do not reflect the official policy or position of the United States Air Force, Department of Defense, or the United States Government.

AFIT/GAE/ENY/08-J03

**LASER-INDUCED FLUORESCENCE AND PERFORMANCE ANALYSIS OF  
THE ULTRA-COMPACT COMBUSTOR**

THESIS

Presented to the Faculty

Department of Aeronautics and Astronautics

Graduate School of Engineering and Management

Air Force Institute of Technology

Air University

Air Education and Training Command

In Partial Fulfillment of the Requirements for the  
Degree of Master of Science in Aeronautical Engineering

Patrick J. Lakusta, BS

Ensign, USN

June 2008

APPROVED FOR PUBLIC RELEASE; DISTRIBUTION UNLIMITED.



## Abstract

The AFIT Combustion Optimization and Analysis Laser (COAL) lab's modular design and state-of-the-art diagnostic systems make it a flexible and important facility for the analysis of combustion processes. The objectives of the current research are to install several enhancements in the lab, validate the laser diagnostic system, characterize the igniter for AFIT's Ultra-Compact Combustor (UCC) sections, and perform a non-intrusive laser diagnostic, performance, and high-speed video analysis of a flat-cavity UCC section. Validation of the laser system was accomplished using OH Planar Laser-Induced Fluorescence (PLIF) in a laminar hydrogen-air flame produced by a Hencken burner. Results are compared to previous research to show improvements. Both ratios of intensities and excitation scans in the OH (A-X) (1-0) electronic transition system are used to measure temperature and species concentrations. Igniter characterization was accomplished using open-air flammability and flame height observations to select an anticipated operating condition. That condition was validated by attaching the igniter to the UCC section and observing its performance. An operating procedure is recommended. A PLIF flame location study using optically-clear quartz windows on the combustor was performed in the cavity-vane area. Performance measurements and high-speed video footage were also acquired in order to analyze the system. Results are compared to previous experimental and Computational Fluid Dynamics (CFD) research. Future work will include instantaneous two-color PLIF and other laser diagnostic studies of several different locations inside AFIT's flat- and curved-cavity UCC sections.

## **Acknowledgements**

First I would like to thank my family for being so incredibly supportive of me during my entire academic career. They have always given me the encouragement I need to accomplish the goals set before me, and I am truly blessed to call such strong and caring people my family.

I want to thank my adviser, Major Rich Branam, for his guidance and flexibility. He taught me everything I know about combustion, from the fundamentals learned in class to actual systems in the lab. His ability to keep me calm and encourage me to keep pushing has made this research, and my graduation, possible.

I also want to especially thank Stanislav Kostka, an exchange Ph.D. student on loan to AFIT from UConn. Stan taught me volumes about combustion laser diagnostics and was able to show me the physical application of the theory. Most importantly, he kept the lab an entertaining place with his Top Gun quotes and Borat references.

Huge thanks go out to lab technicians John Hixenbaugh and Chris Zickafoose for all of their hard work and Friday lunches. Without their efforts, none of the testing would have been possible and the lab would have remained in pieces. Thanks also go to Keith Grinstead for saving me multiple times when I was out of gases, short on equipment, or in need of guidance on the laser. Additional thanks to Dr. Joe Zelina and Dr. Julian Tishkoff for their crucial role in funding the research.

Finally and above all, I want to thank my Lord and Savior, Jesus Christ. He brought me here and has led me to accomplish something I am proud of. I know that through good times and bad, He will continue to guide me through my life and career.

Patrick J. Lakusta

## Table of Contents

	Page
Abstract.....	iv
Acknowledgements.....	v
Table of Contents.....	vi
List of Figures.....	viii
List of Tables.....	xiv
List of Symbols.....	xv
List of Abbreviations.....	xvii
I. .... Introduction.....	1
1.1 Research and Design Perspective.....	1
1.2 Description of the Ultra Compact Combustor.....	2
1.3 Combustor Design Parameters.....	5
1.4 Thesis Objectives.....	6
1.5 Methods.....	8
II. .... Theory and Background.....	12
2.1 Combustion.....	12
Chemistry.....	12
Stoichiometry and Equivalence Ratio.....	13
Flame Speed and Flameholding.....	14
2.2 Conventional Combustors.....	16
Design.....	16
Thermodynamic Cycle.....	18
2.3 UCC Development.....	19
Centrifugally-Enhanced Combustion.....	20
Trapped Vortex Combustion.....	20
Design of the UCC.....	22
Computational Fluid Dynamics Research.....	22
Experimental Research.....	24
2.4 Use of the UCC as an Inter-Stage Turbine Burner.....	26
2.5 Combustor Performance Parameters.....	29
Combustion Efficiency.....	30
Pressure Loss.....	30
Thrust Specific Fuel Consumption and Specific Thrust.....	31
2.6 2-D Sectional Design.....	31
2.7 Laser Diagnostics.....	34
Planar Laser-Induced Fluorescence.....	34
PLIF Thermometry.....	36
Quenching and Power Corrections.....	41
Laser Structure.....	42
III. .... Methodology.....	43



	Page
3.1	Objective Achievement..... 43
3.2	Major Laboratory Alterations ..... 44
3.3	Operation of Combustive Systems..... 50
	Lab-View ..... 51
	Theoretical Calculations ..... 52
	Mass Flow Controller Calibration and Operation..... 56
	Hencken Burner Operation ..... 60
	Igniter Operation..... 63
	UCC Section Operation ..... 65
3.4	Laser Operations ..... 69
	Set-Up and Operation ..... 70
	Calibration..... 73
	LIFBASE ..... 77
	PLIF Image Collection..... 79
	Quenching Correction..... 81
3.5	High-Speed Camera Operations ..... 83
IV. ....	Results and Discussion ..... 85
4.1	Hencken Burner OH PLIF Results ..... 85
	General Calibration Work..... 85
	Intensity Ratio Method ..... 91
	Excitation Scan Method..... 96
	OH Concentration ..... 103
4.2	Igniter Characterization ..... 106
4.3	UCC Section Test Results..... 111
	OH PLIF in the Cavity-Vane Area ..... 111
	Dual-Vortex Observations ..... 122
	Performance Analysis ..... 124
V.....	Conclusions..... 130
5.1	Project Overview ..... 130
5.2	Future Work and Recommendations ..... 131
	Appendix A: Tank Farm Configuration..... 133
	Appendix B: COAL Lab Operational Procedures ..... 134
	Appendix C: Example STANJAN Calculation..... 138
	Bibliography ..... 145
	VITA..149

## List of Figures

	Page
<b>Figure 1.</b> TVC utilizing vortices shed from the main flow into a circumferential cavity (Greenwood, 2005:2).....	3
<b>Figure 2.</b> Primary design elements of the Ultra-Compact Combustor (Anthenien et al., 2001:6). .....	4
<b>Figure 3.</b> AFIT's 2-D planar sectional model of the UCC (Anderson, 2007:72). .....	7
<b>Figure 4.</b> Laminar flame produced by a Hencken burner. ....	9
<b>Figure 5.</b> The AFIT 2-D sectional UCC model exhibiting "dual-vortex" behavior using JP-8 as fuel (photo by C. Zickefoose). .....	10
<b>Figure 6.</b> Two views of AFIT's UCC model exhibiting "dual-vortex" behavior using hydrogen (H <sub>2</sub> ) as fuel.....	11
<b>Figure 7.</b> Diagram of a turbojet using a conventional combustor (Mattingly, 1996). .....	16
<b>Figure 8.</b> Typical design for a conventional gas-turbine combustor (Adapted from Mattingly, 1996).....	17
<b>Figure 9.</b> Engine cycle for a typical gas-turbine combustor (Adapted from Liu et al., 2000:9). .....	19
<b>Figure 10.</b> A design for a TVC experimental research rig (Roquemore et al., 2001). .....	22
<b>Figure 11.</b> Curved UCC sectional rig developed by Moenter for CFD analysis. The plot shows temperature contours (K), with airflow to the right in the cavity and out of the page in the main vane (Moenter, 2006:112).....	24
<b>Figure 12.</b> Schematic of the original UCC experimental rig. The support spider did not include an RVC design. Flow path is from left to right (Zelina et al., 2004).....	25
<b>Figure 13.</b> Thermodynamic cycle for an engine using an inter-stage turbine burner (solid line) overlayed on an example of a traditional gas-turbine cycle (dashed line) (Adapted from Liu et al., 2000:9). .....	28
<b>Figure 14.</b> CFD designs of various radial-vane cavity shapes (Mawid et al., 2006). .....	29
<b>Figure 15.</b> Cut-away view of the curved cavity for AFIT's UCC sectional model (Hankins, 2008:7).....	32
<b>Figure 16.</b> The AFIT 2-D sectional UCC model with quartz viewing windows installed at several locations. ....	33

	Page
<b>Figure 17.</b> The X and A energy states with sub vibrational levels shown. Rotational levels are not shown. Vertical arrows designate increasing and decreasing energy (Adapted from Eckbreth et al., 1998).....	37
<b>Figure 18.</b> An example of the rotational structure of a vibrational level (Adapted from Eckbreth et al., 1998). .....	38
<b>Figure 19.</b> Illustration of the full-width, half-maximum method for excitation scan analysis. Image generated by LIFBASE (Hankins, 2008:66).....	41
<b>Figure 20.</b> One of the 16” Dayton exhaust fans. ....	45
<b>Figure 21.</b> Asco electronically-operated solenoid valve used for remote fuel shut-off. ....	46
<b>Figure 22.</b> Electric damper switch and actuator. ....	47
<b>Figure 23.</b> Original design (left) of the COAL lab’s test stand next to the new configuration (right) with wheels eliminated (Anderson, 2007:70).....	48
<b>Figure 24.</b> New configuration of the UCC section (left), with cavity exhaust oriented straight up into ventilation system, compared to the old configuration (right) which used an extension to redirect the exhaust from the cavity (Hankins, 2008). ....	49
<b>Figure 25.</b> The incorporation of filtration units at two different locations in AFIT’s COAL lab. ....	50
<b>Figure 26.</b> Central control station for AFIT's COAL lab. ....	51
<b>Figure 27.</b> Lab-View VI control interface. Arrow points to new fuel toggle switch. ....	52
<b>Figure 28.</b> Several of the MKS ALTA digital mass flow controllers used in the COAL lab. The black arrow points to the zero reset button (Hankins, 2008:48). ....	56
<b>Figure 29.</b> MKS Type 247 4-Channel Readout used to operate the MKS ALTA digital mass flow controllers (Hankins, 2008:49). ....	57
<b>Figure 30.</b> BIOS International Corporation Definer 220-H flow meter used for calibration of the MKS ALTA digital mass flow controllers (Hankins, 2008:50). ....	58
<b>Figure 31.</b> Calibration plot of hydrogen settings and corresponding flow rates on a 30 SLPM MKS ALTA digital mass flow controller. ....	60
<b>Figure 32.</b> The Hencken burner used for calibration of AFIT's COAL lab laser systems. ....	62
<b>Figure 33.</b> Hencken burner and laser optics used for laser calibration in AFIT's COAL lab. The red arrows denote the path of the laser sheet. ....	63

	Page
<b>Figure 34.</b> Two views of the open-air configuration used for igniter characterization. ....	65
<b>Figure 35.</b> New fuel injectors developed for the use of gaseous fuels in AFIT's UCC sections. ....	67
<b>Figure 36.</b> A view of AFIT's flat-cavity UCC section showing the use of ceramic fiber as a sealant. ....	68
<b>Figure 37.</b> A view of AFIT's flat-cavity UCC section showing the location of state measurements on the combustor (Hankins, 2008:94). ....	69
<b>Figure 38.</b> Diagram of the COAL lab's PLIF laser system and beam path. ....	71
<b>Figure 39.</b> The laser operating station in AFIT's COAL lab (Hankins, 2008:43). ....	72
<b>Figure 40.</b> This image shows the placement of the heat shield between any hot exhaust and the laser optics. The red arrow represents the UCC's exhaust flow. ....	73
<b>Figure 41.</b> This image shows the beam-alignment process using adjustable irises. ....	74
<b>Figure 42.</b> The graph paper and metal plate alignment aid used for Hencken burner tests. ....	75
<b>Figure 43.</b> The plastic sleeve designed for beam alignment in the UCC section. ....	76
<b>Figure 44.</b> A screenshot of the LIFBASE program used for calculations in the OH (A-X) (1-0) vibrational level. Wavelengths are given in Angstroms (Hankins, 2008:57). ....	78
<b>Figure 45.</b> The Princeton Instruments ICCD camera used for image collection in AFIT's COAL lab. ....	79
<b>Figure 46.</b> Screenshot of the Win-View 32 software used for image analysis (Hankins, 2008:45). ....	80
<b>Figure 47.</b> Laser optics mounted on one of two Universal motion control tracks in AFIT's COAL lab. ....	81
<b>Figure 48.</b> Integrated Design Tools, Inc. X-Stream XS-4 high-speed camera used for image collection in AFIT's COAL lab. ....	84
<b>Figure 49.</b> Results of the timing process for the COAL lab's Princeton Instruments ICCD camera. A hydrogen-air flame created by a Hencken burner at $\phi = 1$ was used to produce OH. ....	86
<b>Figure 50.</b> Results of the saturation check on the hydrogen-air Hencken burner flame in AFIT's COAL lab. ....	86
<b>Figure 51.</b> Screenshot of Win-View 32 showing the ROI used for the PLIF system calibration on the Hencken burner. ....	87
<b>Figure 52.</b> Results of the signal per accumulation check. ....	88

	Page
<b>Figure 53.</b> Experimental results for the initial peak search at the P <sub>1</sub> (5), Q <sub>2</sub> (8), and Q <sub>1</sub> (9) rotational variation lines.....	90
<b>Figure 54.</b> Experimental results for the initial peak search at the P <sub>1</sub> (7) rotational variation line. ....	90
<b>Figure 55.</b> LIFBASE theoretical predictions for three candidates for the temperature-insensitive line used in PLIF thermometry.....	91
<b>Figure 56.</b> LIFBASE theoretical predictions for the eight temperature-sensitive lines used in PLIF thermometry. ....	92
<b>Figure 57.</b> Theoretical temperature trends with intensity ratio based on LIFBASE calculations. The black lines are trend lines.....	93
<b>Figure 58.</b> Temperature readings generated using the intensity ratio method of PLIF thermometry. Theoretical data was calculated by STANJAN.....	94
<b>Figure 59.</b> LIFBASE simulations of the Q <sub>1</sub> (5) rotational line at a range of temperatures. The red arrow indicates the direction of increasing temperature, and the secondary peak is well below the half-maximum point. ....	97
<b>Figure 60.</b> An example of the theoretical FWHM calculation method. This LIFBASE data was calculated for the Q <sub>1</sub> (5) line at 2400 K. ....	98
<b>Figure 61.</b> Theoretical FWHM trend with temperature for the Q <sub>1</sub> (5) line based on LIFBASE calculations. The black line is the trend line used for thermometry. ....	99
<b>Figure 62.</b> Experimental intensity data gathered for the Q <sub>1</sub> (5) line at an equivalence ratio of one plotted over theoretical data generated by LIFBASE. ....	100
<b>Figure 63.</b> The curve-fitting plot used for FWHM calculation for the Q <sub>1</sub> (5) line at $\phi = 1$ . ....	101
<b>Figure 64.</b> Theoretical FWHM trend with temperature for the Q <sub>1</sub> (14) line based on LIFBASE calculations. The black line is the trend line used for thermometry. ....	102
<b>Figure 65.</b> The curve-fitting plot used for FWHM calculation for the Q <sub>1</sub> (14) line at $\phi = 1$ . ....	102
<b>Figure 66.</b> Signal counts for power-corrected intensity relative to power- and quenching-corrected intensity. ....	104
<b>Figure 67.</b> OH concentration and power- and quenching-corrected signal versus equivalence ratio. ....	105
<b>Figure 68.</b> Raw and fully corrected signal counts versus OH concentration. Error bars represent the standard deviation of the raw signal in the ROI. ....	106

	Page
<b>Figure 69.</b> Flame height observations with changing equivalence ratio for open-air igniter operation at multiple air flow rates.....	108
<b>Figure 70.</b> Flame height observations with changing air flow rate for open-air igniter operation at $\phi = 2.1$ .....	109
<b>Figure 71.</b> A single-accumulation image of OH PLIF in AFIT's flat-cavity UCC section using hydrogen as fuel. Screenshot produced using Win-View 32.....	112
<b>Figure 72.</b> An average of 20 images of OH PLIF in AFIT's flat-cavity UCC section using hydrogen as fuel. Screenshot produced by Win-View 32.....	113
<b>Figure 73.</b> A 20-image series shown in pseudo-color of OH PLIF in AFIT's flat-cavity UCC section. For reference to combustor location, the images are overlaid on the focusing image used for camera tuning.....	114
<b>Figure 74.</b> Win-View 32 screenshot showing the ROI used for image analysis in the UCC PLIF study. The image used is the camera-focus image, selected for the presence of the calibration aid. The red arrow points to the trailing edge of the RVC. ....	115
<b>Figure 75.</b> Screenshot of an averaged image of OH PLIF in AFIT's flat-cavity UCC section using hydrogen fuel. The green box overlaid on the image is the ROI used for analysis and comparison. Produced using Win-View 32.....	116
<b>Figure 76.</b> PLIF results of varying cavity equivalence ratio at several main flow rates in AFIT's flat-cavity UCC. Images taken in cavity-vane area. ....	117
<b>Figure 77.</b> PLIF results of varying the main flow rate at several laser sheet locations across the cavity-vane area in AFIT's flat-cavity UCC section. Test was conducted at $\phi = 1$ with cavity flow rate held constant. ....	118
<b>Figure 78.</b> A pseudo-color 20-image average OH PLIF screenshot overlaid on the focusing image used for camera tuning. Main flow rate was 1 kg/min, cavity flow rate was 0.1 kg/min, and overall $\phi = 0.091$ . The red line points to the trailing edge of the RVC. ....	119
<b>Figure 79.</b> A pseudo-color 20-image average OH PLIF screenshot overlaid on the focusing image used for camera tuning. Main flow rate was 3 kg/min, cavity flow rate was 0.1 kg/min, and overall $\phi = 0.032$ . The red line points to the trailing edge of the RVC. ....	119
<b>Figure 80.</b> PLIF results of varying the laser location at several main flow rates in AFIT's flat-cavity UCC section. Test was conducted at cavity $\phi = 1$ with cavity flow rate held constant. Error bars represent one standard deviation from the mean.....	121

	Page
<b>Figure 81.</b> Screenshot of high-speed footage of the UCC exhibiting dual-vortex behavior at a high overall equivalence ratio. The red ovals circle the two tongues of flame.....	123
<b>Figure 82.</b> Screenshot of high-speed footage of the UCC operating at a low overall equivalence ratio, with only one flame exiting the cavity. ....	123
<b>Figure 83.</b> Raw temperature data taken from the UCC and compiled by Lab-View. Main flow and cavity flow were constant at 1 kg/min and 0.1 kg/min, respectively. ....	125
<b>Figure 84.</b> Combustion efficiency averages calculated from UCC performance data gathered by Lab-View at varying cavity equivalence ratios. Error bars represent one standard deviation from the mean. ....	127
<b>Figure 85.</b> Combustion efficiency averages calculated from UCC performance data gathered by Lab-View at varying overall equivalence ratios. Error bars represent one standard deviation from the mean. ....	128
<b>Figure 86.</b> Combustion efficiency averages calculated from UCC performance data gathered by Lab-View at varying overall equivalence ratios. Error bars represent one standard deviation from the mean. ....	128

## List of Tables

	Page
<b>Table 1.</b> Hankins' experimental efficiency and emissions data compared with that predicted by Moenter's CFD analysis at select conditions (Hankins, 2008:120). .....	26
<b>Table 2 .</b> Wavelength spectra open to fluorescent absorption for species of interest in combustion diagnostics (Eckbreth et al., 1979:260-265). .....	35
<b>Table 3.</b> Equivalence ratio and fuel flow rate data for a hydrogen-air flame with the air flow rate held constant at 40 SLPM. ....	54
<b>Table 4.</b> Equivalence ratio and fuel flow rate data for an ethylene-air flame with the air flow rate held constant at 10 SLPM. ....	55
<b>Table 5.</b> Constant values needed for quenching correction factor calculations (Hankins, 2008:63). ....	82
<b>Table 6.</b> Empirical values for quenching correction factor calculations (Tamura et al., 1998:502-514). ....	82
<b>Table 7.</b> Rotational variations and wavelengths of the OH (A-X) (1-0) vibrational level investigated for use in PLIF thermometry. ....	89
<b>Table 8.</b> Experimental temperature accuracies for the Q <sub>1</sub> (14)/Q <sub>1</sub> (5) line pair compared to theoretical data and previous research. ....	95
<b>Table 9.</b> UCC performance data recorded by Lab-View at a range of operational conditions. ....	126



## List of Symbols

Symbol

$a$	Mols of air
$A$	Area, OH spontaneous emissions constant: $1.45 \times 10^6 \text{ s}^{-1}$
Ar	Argon
$A/F$	Air-to-fuel ratio
cm	Centimeters
CO	Carbon Monoxide
CO <sub>2</sub>	Carbon Dioxide
$C_p$	Constant-pressure specific heat
$C_xH_y$	General formula of a hydrocarbon
C <sub>2</sub> H <sub>4</sub>	Ethylene
G	Multiples of the gravitational constant
hr	Hour
H <sub>C</sub>	Heat of combustion of fuel
Hz	Hertz
H <sub>2</sub>	Hydrogen
H <sub>2</sub> O	Water
J	Joules
$k$	Boltzman's constant: $1.38065 \times 10^{-23} \frac{\text{m}^2\text{kg}}{\text{s}^2\text{K}}$
K	Degrees Kelvin
kg	Kilograms
kJ	Kilojoules
$m, m$	Mass, meter
$\dot{m}$	Mass flow rate
mJ	Millijoules
mm	Millimeters
ms	Millisecond
mW	Milliwatt

min	minute
$MW$	Molecular Weight
nm	Nanometer
ns	Nanosecond
$N_2$	Nitrogen
$NO_x$	Oxides of Nitrogen
OH	Hydroxyl
$O_2$	Oxygen
$P$	Pressure
$Q, Q$	Heat, quenching rate
$R$	Intensity ratio
$s, s$	Entropy, second
$S_B$	Buoyant flame speed
$S_L$	Laminar flame speed
SLPM	Standard liters per minute
$T$	Temperature, thrust
$U$	Combustor inlet velocity
$v$	Velocity
$x$	Number of carbon atoms
$y$	Number of hydrogen atoms
(A-X)	OH energy states
$\text{Å}$	Angstroms
$\frac{dP}{P}$	Pressure drop
$\beta, \gamma$	Exponents for laminar flame speed calculation
$\frac{\varepsilon}{\kappa}$	Quenching temperature factor
$\phi$	Equivalence Ratio
$\eta_b$	Combustion efficiency
$\rho$	Density
$\sigma_Q$	Quenching rate coefficient

## List of Abbreviations

### Abbreviation

AFIT	Air Force Institute of Technology
AFRL	Air Force Research Laboratory
CARS	Coherent anti-Stokes Raman-Scattering
CIAC	Cavity-in-a-cavity
CFD	Computational Fluid Dynamics
CT	Constant-temperature
COAL	Combustion Optimization and Analysis Laser
CTB	Continuous turbine burner
FWHM	Full-width, half-maximum
HPT	High-pressure turbine
ICCD	Intensifying charge-coupled device
IDT	Integrated Design Tools
ISSI	Innovative Scientific Solutions Inc.
ITB	Inter-stage turbine burner
JP-8	Jet fuel
KDP	Potassium dideuterium phosphate
LBO	Lean Blowout
LDV	Laser Doppler Velocimetry
LHV	Lower heating value
LII	Laser-induced incandescence
LPT	Low-pressure turbine
Nd:YAG	Neodymium-doped yttrium aluminium garnet
PIV	Particle imaging velocimetry
PLIF	Planar Laser Induced Fluorescence
ROI	Region of interest
RVC	Radial Vane Cavity
ST	Specific thrust

TSFC	Thrust specific fuel consumption
TVC	Trapped Vortex Combustion
UCC	Ultra Compact Combustor
UHC	Unburned hydrocarbons
UV	Ultra-violet
VI	Virtual Instrument
2-D	Two dimensional

# LASER-INDUCED FLUORESCENCE AND PERFORMANCE ANALYSIS OF THE ULTRA-COMPACT COMBUSTOR

## I. Introduction

### 1.1 *Research and Design Perspective*

The United States is the world's largest consumer of petroleum-based fuels (United, 2008) with about 20% of that consumption providing for aviation-related needs, both military and commercial (Fuel, 2005). The demand for commercial air travel is not likely to decrease in the near future, and with today's volatile and wide-spread threat environment, military sorties are certain to continue at their high operational rate. However, the cost of these fuels continues its alarming rise, triggering financial woes for not just the average American citizen, but also for those organizations charged with their protection. With mounting environmental concerns adding to the economic pressure for more efficient fuel usage, the drive for increased speed, altitude, endurance, and payload will necessarily focus on improved combustion technology. Improved combustion methods would exhibit increased thrust-to-weight ratios and decreased thrust-specific fuel consumptions (TSFC), and have the potential added benefits of decreased maintenance and operational costs, as well. In order for American forces to continue their dominance of the skies and for the commercial airline industry to thrive, it is vital that future propulsion research focus on better and more efficient combustion.

One major research effort undertaken by the Air Force Institute of Technology (AFIT) and the Air Force Research Laboratories (AFRL) involves removing the traditional in-line combustor of gas-turbine engines and replacing it with a burner

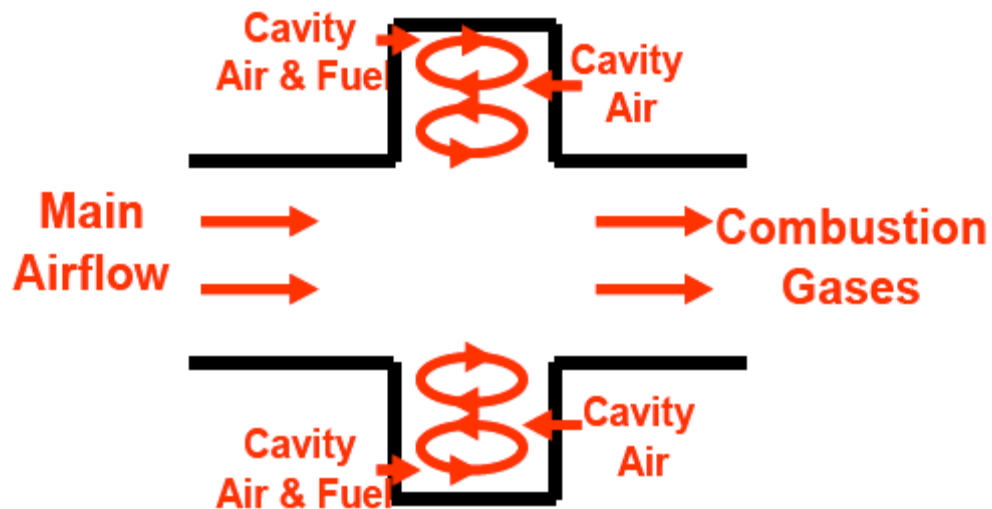
wrapped circumferentially around the turbine section. This technology, called the Ultra-Compact Combustor (UCC), will allow the turbine to be moved directly behind the compressor while also burning fuel more efficiently, thus increasing thrust-to-weight ratio. Computational Fluid Dynamics (CFD) simulations of various UCC configurations have shown significant potential toward achieving the goals discussed above. Only recently, however, has experimental research begun to validate these theoretical predictions.

### ***1.2 Description of the Ultra Compact Combustor***

Conventional combustor designs are limited by the fact that combustion reactions require a finite amount of time for completion and the flow through these devices is moving at a finite velocity. By necessity, traditional combustors are long and compose a significant portion of a gas-turbine engine's volume. In order to sustain a flame, many of these designs induce a swirl in the mixing area which maintains a region of steady combustion, a method called swirl-stabilization. While effective at this task, swirl-stabilization does not significantly shorten the length needed in the combustor for a complete reaction of the fuel and air. In order to address this basic limitation of combustors, the UCC is designed to increase the residence time of the flame by lengthening its flow path while still significantly reducing the length of the combustion section.

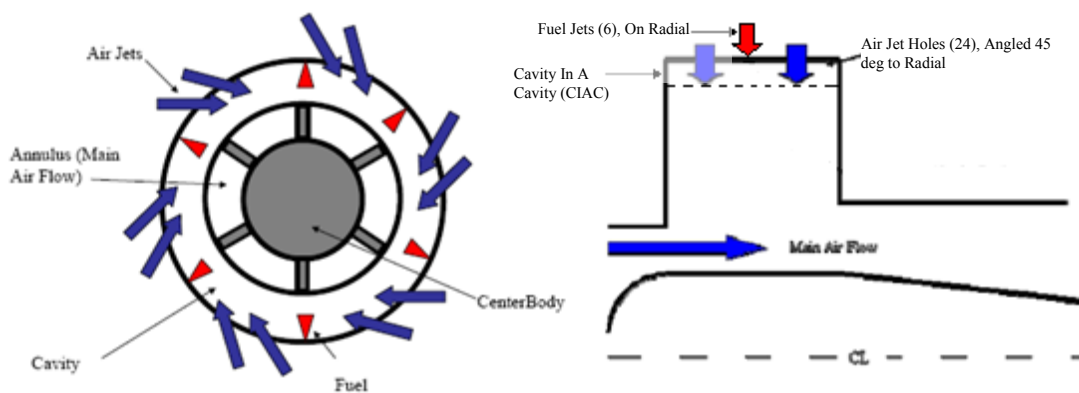
The two principle concepts which drive these improvements are the utilization of centrifugal force to improve mixing, and trapped vortex combustion (TVC). By spinning a flow at high velocities, centrifugal force can be imparted on the components of the flow. This force, also known as a "G-load," enhances component mixing and increases

the flame propagation rate. Lewis showed that there exist three primary flame-spreading mechanisms: 1) laminar flames, with a flame speed around 0.3 meters per second in hydrocarbons, 2) turbulent flames, which burn at about 6 meters per second, and 3) buoyant bubble flames, which can range from 18 to 30 meters per second. He also showed the buoyant bubble condition only exists in a flow subjected to more than 500 G's (Lewis, 1973:413-419). Yonezawa supported this theory with his Jet-Swirl High Loading Combustor research in 1990 (Yonezawa et al., 1990:1-7). Trapped vortex combustion is an improved version of conventional swirl-stabilization, and involves the creation of standing vortices in cavities within the combustor. When induced correctly, this technique has been more successful as a flame-stabilization method, while also acting as the primary combustion zone for a burner. Previous research indicates a cavity air flow rate of about 10% of the main flow creates the best conditions for TVC (Sturgess et al.). Figure 1 shows one method of TVC which utilizes vortex shedding from the main flow into a cavity.



**Figure 1.** TVC utilizing vortices shed from the main flow into a circumferential cavity (Greenwood, 2005:2).

To capitalize on these theories, the UCC is designed as a cavity built around the circumference of the engine's axis. Around the outside of the UCC, fuel and air are injected through 6 fuel nozzles and 24 air holes, separated as 12 pairs with two pairs between each fuel injector. In order to induce high velocity spinning in the cavity, the air holes are drilled at a 45-degree angle. The inner side of the UCC cavity is left open to the main flow to facilitate the exhaust's escape from the combustor and adding a third dimension to the vortices and swirl created along the outer wall. The angled injection of air results in tangential velocities in the combustor of 3 to 14 meters per second, resulting in G-loads from 300 to 4000 G's. This high G-load and the induced buoyant bubble combustion result in a density stratification in the combustor, in which the cold, unreacted fuel and air stay along the outer wall and the hot, less dense combustion products are transported to the inside and to the main flow. Figure 2 shows the major design elements of the UCC.



**Figure 2.** Primary design elements of the Ultra-Compact Combustor (Anthenien et al., 2001:6).

Supporting the cavity are 6 radial vanes, each with their own cavity built in.

These radial-vane cavities (RVC) support the movement of the exhaust products into the



main flow by creating a low pressure wake and vortex, and also provide an intermediate combustion zone for any unburned fuel (Moenter, 2006:3). Finally, at the fuel injection points, an additional axially-oriented cavity, or cavity-in-a-cavity (CIAC), provides the flame stabilization region inherent in TVC.

The benefits derived from the employment of the UCC are great. Its much smaller size allows the UCC to be used as both the primary combustor as well as an inter-stage turbine burner (ITB). As the main combustor, the UCC shortens the combustion section by 66% while maintaining up to 99% combustion efficiency. In this manner, a smaller engine using less fuel could provide the same thrust as a larger engine without the weight, thus increasing the thrust-to-weight ratio by up to 25%. With a second UCC added as an ITB, a reheat cycle would be created, more closely mimicking a constant temperature (CT) engine cycle. This configuration would increase specific thrust (ST) without the high TSFC of conventional afterburners (Sirignano, 1999:111-118). The UCC also exhibits decreased pressure drop across the combustor and lower levels of pollutants in the exhaust due to the increased burning efficiency.

### **1.3 Combustor Design Parameters**

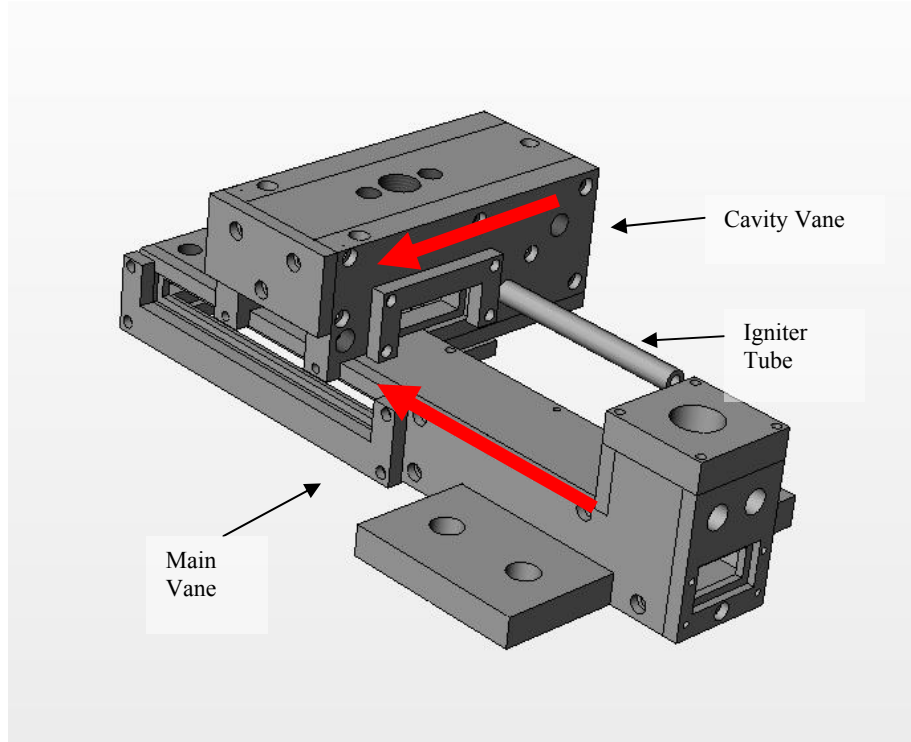
Lefebvre outlines 11 combustion parameters which quantifiably evaluate a combustor's performance, two of which will be measured in this thesis. Combustion efficiency ( $\eta_b$ ) and pressure drop ( $\frac{dP}{P}$ ) can be used to experimentally evaluate the UCC model. In addition, the UCC operating temperature range and flame locations can be determined and comparatively analyzed using non-intrusive laser diagnostic techniques.

#### **1.4 Thesis Objectives**

The UCC study being conducted by AFRL and AFIT has three main purposes. The first is to investigate the effect of body forces on the combustion process in a true UCC design. As mass flow in the cavity is increased, the turbulent Reynolds number in the main flow path has been shown to decrease. This research area is intended to discover whether this behavior is an effect of body forces or flow shear by holding velocity constant while altering the radius of curvature, and thus the G-load. The effects of altering air jet geometry, equivalence ratio, and main air flow velocity will all be investigated. The second purpose is to investigate the effectiveness of performing Trapped Vortex Combustion in the UCC. Using CFD models supported by experimental data, the best conditions for extracting mass from the cavity into the main flow will be determined. The effect of trapping a vortex in the cavity on performance and range of operation will also be investigated. Finally, the reactions between the cavity and vane cavity must be observed and understood in order to ensure optimal mass transfer from the cavity to the main flow. CFD studies will focus on variations of the geometry of the radial vanes and their cavities and the effects on combustor performance parameters. Experimental models will be based on optimum geometries found using CFD analysis.

This thesis will focus on advancing the second and third research areas by investigating combustor performance and the cavity-vane interactions. Research will be conducted in AFIT's Combustion Optimization and Analysis Laser (COAL) lab, and investigation techniques will include Planar Laser-Induced Fluorescence (PLIF) thermometry, emissions analysis, and high-speed visual recording. The geometry of the full UCC design precludes any direct, non-intrusive measurements of the conditions

inside the cavity, and particularly in the cavity-vane region. In order to circumvent this problem, a 2-D planar section of the UCC will be used. Figure 3 shows its design, with red arrows showing the direction of flow in each component.



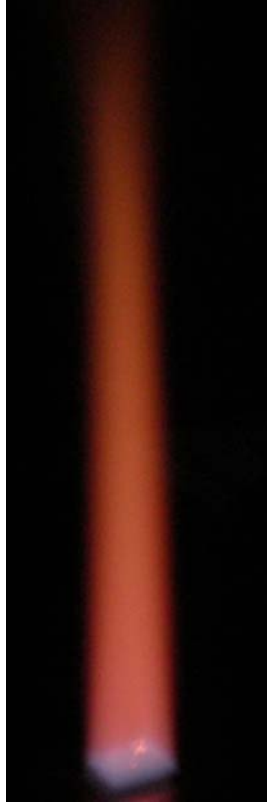
**Figure 3.** AFIT's 2-D planar sectional model of the UCC (Anderson, 2007:72).

This apparatus will simulate a section of the design with infinite radius. No G-loading effects will influence the flow field, but TVC and cavity-vane characteristics are still present and are more easily observed. Specific objectives for this thesis include lab enhancements, calibration and validation of the PLIF laser system, igniter characterization, visual analysis of the “dual-vortex” behavior reported by Hankins, PLIF analysis of the cavity-vane area, and a performance analysis of the planar sectional system.

## 1.5 *Methods*

Before further testing could be performed, the COAL lab received noted improvements. During Hankins' testing, several areas of improvement were identified in the lab's equipment, and methods for optimizing the test environment were discovered. Hankins has recommended increasing the ventilation capabilities and adding an electric fuel shutoff-valve at the combustor which would be operated from the main control screen. Additional work needed includes removing the test stand from its wheeled base and mounting it directly to the lab deck, reorienting the combustor so the cavity exhaust exits directly into ventilation, filtering all incoming gas lines, reorganizing the tank farm, and linking all lab computers using KVM switches. With this lead-up work complete, experimentation can once again begin.

The first objective of this thesis will be to calibrate the PLIF laser diagnostic system using the laminar hydrogen-air flame produced by a Hencken burner, shown in Figure 4.

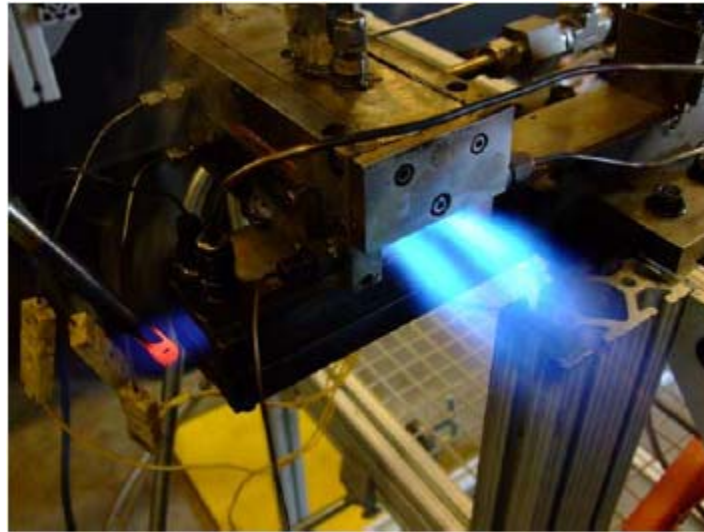


**Figure 4.** Laminar flame produced by a Hencken burner.

As recommended by Hankins, the Hencken burner will be operated at higher flow rates than previously studied in order to lift the flame from the burner's surface and prevent heat transfer to the device (Hankins, 2008:123). During this calibration, the laser suite's ability to perform two methods of PLIF thermometry (intensity ratio and excitation scan analysis) will be validated. The second objective is to characterize the igniter used in the UCC. During previous testing, a steady ethylene torch was not able to be maintained which may have contributed to uncertainties when tabulating the UCC's ignition conditions. By discovering a steady operating regime, operators can ensure a quick start every time.

With this task complete, work on the UCC section can begin. The next objective will be to confirm the functionality of the seals on the combustor and install optically-clear quartz viewing windows to facilitate laser and visual diagnostics. In order to evaluate the laser diagnostic methods and the window concept, hydrogen will first be used as the fuel for the UCC. This will prevent any carbon soot from clouding the windows and allow for further evaluation of starting conditions without optical interference. Starting conditions will need to be verified for each fuel.

Next, with a hydrogen flame established in the UCC, visual analysis of the “dual-vortex” condition noted by Hankins can be conducted. Figures 5 and 6 show this condition with both JP-8 and hydrogen as fuel.



**Figure 5.** The AFIT 2-D sectional UCC model exhibiting "dual-vortex" behavior using JP-8 as fuel (photo by C. Zickefoose).



**Figure 6.** Two views of AFIT's UCC model exhibiting "dual-vortex" behavior using hydrogen ( $H_2$ ) as fuel.

Using a high-speed camera, images of this behavior can be recorded and the conditions at which it exists can be deduced. During this process, PLIF imagery of the turbulent flame inside the UCC will be taken in order to determine flame location and operating characteristics. By correlating these results with STANJAN, species concentrations can also be estimated. During these measurements, a limited performance analysis must be conducted in order to determine the combustion efficiency and pressure drop of the cavity. Finally, validation of the igniter characterization will be accomplished by lighting JP-8 repeatedly and consistently in the UCC model.

## II. Theory and Background

### 2.1 Combustion

Combustion is the general term used to describe the rapid oxidation of a fuel, which converts the energy stored in chemical bonds to heat and light (Turns, 2006:6). This process provides approximately 85% of U.S. energy, and is the method by which gas-turbine engines are powered (Turns, 2006:1).

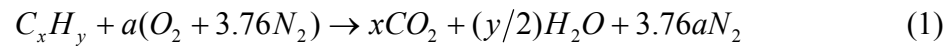
#### *Chemistry*

Combustion processes generally proceed in either flame or non-flame modes, with the flame mode comprising both premixed and diffusion flames (Turns, 2006:6-7). The propagation method, determined by temperature, fuel concentration and composition, and pressure dictates the type of chemical products released (Lefebvre, 1999:317). When considered in an equilibrium relationship, the products of hydrocarbon-fueled combustion will include many chemical species; but Turns defines several of most concern in today's environmentally-conscious world. Of these products, gas-turbine engines are typically producers of unburned hydrocarbons (UHC), oxides of nitrogen ( $\text{NO}_x$ ), carbon monoxide (CO), and soot particles (Turns, 2006:3). In conventional combustors, a high power (fuel-rich) condition tends to produce more  $\text{NO}_x$  and soot, while low power (fuel-lean) produces more UHC and CO (Quaale, 2003:27). While the UCC operates as a turbulent diffusion flame similar to conventional combustors, its added mixing and residence time characteristics reduce these emissions greatly.



### Stoichiometry and Equivalence Ratio

For the purposes of determining the relationship between the amount of air, or oxidizer, and the amount of fuel present, stoichiometric relationships must first be used. When burning at stoichiometric conditions, the fuel in the area of interest has just enough oxidizer present to react completely (Turns, 2006:18). Combustion is said to be fuel-lean if there is more oxidizer than needed, and fuel-rich if there is less than needed for the reaction of all of the fuel (Hankins, 2008:23-24). If complete combustion at sea level is assumed, a short, balanced chemical reaction can be used to determine the stoichiometric air-to-fuel ratio:



Balancing this reaction yields  $a = x + y/4$ . With this relationship established, the mass stoichiometric air-to-fuel ratio is found using the following equation (Turns, 2006:19):

$$\left(\frac{A}{F}\right)_{ST} = \frac{4.76a}{1} \frac{MW_{Air}}{MW_{Fuel}} \quad (2)$$

Where  $MW_{Air}$  and  $MW_{Fuel}$  are the molecular weights of the air and fuel in kg/kmol, respectively. Frequently in the lab, however, volumetric air-to-fuel ratio is needed.

Based on the following relationship:

$$\rho = \frac{m}{V} \quad (3)$$

Equation 2 could be written as  $mass\ ratio = volume\ ratio * density\ ratio$ . This shows that the volumetric air-to-fuel ratio at stoichiometric conditions is found by Equation 4:

$$\left(\frac{A}{F}\right)_{ST} = 4.76a \quad (4)$$

In order to quantify and measure the fuel-lean and fuel-rich states, the equivalence ratio, defined in Equation 5, is used. This ratio relates a combustion state in terms of air-to-fuel ratio to stoichiometric conditions.

$$\phi = \frac{(A/F)_{ST}}{(A/F)_{Used}} \quad (5)$$

Using this relationship, fuel-rich combustion is defined as having  $\phi > 1$ , fuel-lean combustion has  $\phi < 1$ , and for stoichiometric combustion,  $\phi$  equals 1. When equivalence ratio is varied, Equation 6 must be used to determine the mols of reactants present for theoretical calculations.

$$a = \frac{x + y/4}{\phi} \quad (6)$$

Given a fuel type and  $\phi$ , and assuming one mol of fuel is used in the reaction, the number of mols of air needed can be determined as  $a$  (Turns, 2006:48).

### *Flame Speed and Flameholding*

Flame speed can be defined as the rate at which a flame front moves through a reacting substance. This speed is a function of temperature, pressure, reactant composition, and equivalence ratio, and varies for every fuel-oxidizer mixture. For a laminar flame, Equation 7 shows the relationship between flame speed, temperature, pressure, and equivalence ratio. Here  $S_{L,ref}$  is a reference flame speed found at  $\phi = 1$  and room temperature (for ethylene,  $C_2H_4$ ,  $S_{L,ref} = 67$  cm/s), and  $\gamma$  and  $\beta$  are functions of  $\phi$ . Speeds are in cm/s, temperature is in degrees Kelvin, and pressure is in atmospheres (Turns, 2006:281).

$$S_L = S_{L,ref} \left( \frac{T}{298} \right)^\gamma \left( \frac{P}{1} \right)^\beta \quad (7)$$

In the case of a turbulent diffusion flame, this concept relates directly to the mass flow rate of reactants into the combustion zone. If density ( $\rho$ ) and the area of the path taken by the reactants ( $A$ ) are held constant, then increased mass flow results in increased velocity ( $v$ ), according to Equation 8.

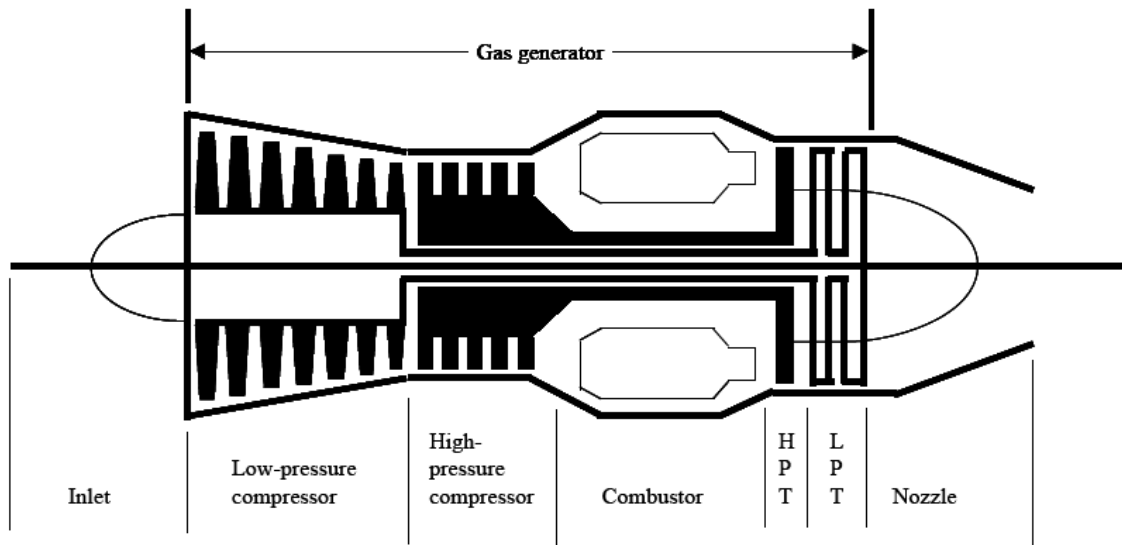
$$\dot{m} = \rho v A \quad (8)$$

As the velocity of the incoming reactants increases, the combustion zone will extend further from the location from which the mixture emanates. This condition, called liftoff, can be desirable in that it minimizes heat transfer to the burner surface for the Hencken flame. However, if the velocity is raised too far above the flame speed, blowout can result (Turns, 2006:294).

Complications in real-world combustion devices arise because it is not always possible to hold the velocity of the reactant mixture below a given flame speed. A technique called flame holding has been devised as a method of avoiding this physical reality. A flame holder is some type of obstruction in a small portion of the flow path generating a stagnant area, keeping a portion of the flame in one spot. As the fuel-oxidizer mixture rushes by, this held flame propagates to the still-moving flow, maintaining a flame even though the velocity of the reactant mixture may be above the flame speed. Flame holding is utilized in the UCC's ethylene-air ignition torch, where in order to achieve a flame of the correct length, flow rates which surpass ethylene's flame speed are necessary.

## 2.2 Conventional Combustors

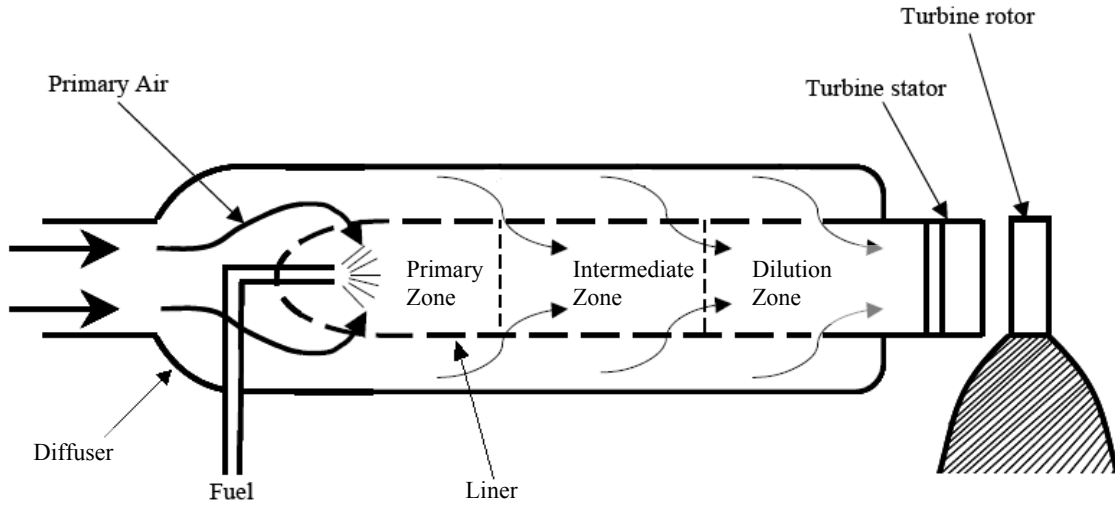
Modern gas-turbine engines utilize a combustor placed in the axial flow path behind the compression section and in front of the power turbines. Figure 7 shows this arrangement. Combustor length provides the residence time needed for the reaction of the fuel without allowing hot flames to enter the turbine, and generally increases with the designed operational altitude. Thus, these systems tend to make up a large percentage of the engine's structure. The layout and thermodynamics of this type of combustor are described below.



**Figure 7.** Diagram of a turbojet using a conventional combustor (Mattingly, 1996).

### *Design*

Typical combustors for gas-turbine engines, like the one shown in Figure 8, are composed of a diffuser built around the reaction area, which can be split into three regions called the primary zone, intermediate zone, and dilution zone.



**Figure 8.** Typical design for a conventional gas-turbine combustor (Adapted from Mattingly, 1996).

The diffuser's function is to slow down the air rushing into the combustor in order to prevent blowout, provide steady flow to the liner, and to reduce hot pressure losses across the system (Lefebvre, 1983:108). This type of loss occurs when heat is added to a moving flow, and is governed by the following equation:

$$\Delta P_{hot} = \frac{1}{2} \rho U^2 \left( \frac{T_4}{T_3} - 1 \right) \quad (9)$$

where  $U$  is the combustor inlet velocity,  $T_3$  is the compressor exit temperature, and  $T_4$  is the temperature at the turbine inlet. The non-linear relationship between  $U$  and  $\Delta P_{hot}$  shows hot pressure loss increases as the square of inlet velocity (Quaale, 2003:5).

Pressure loss reduces combustion efficiency and will be discussed later (Anisko, 2006:6).

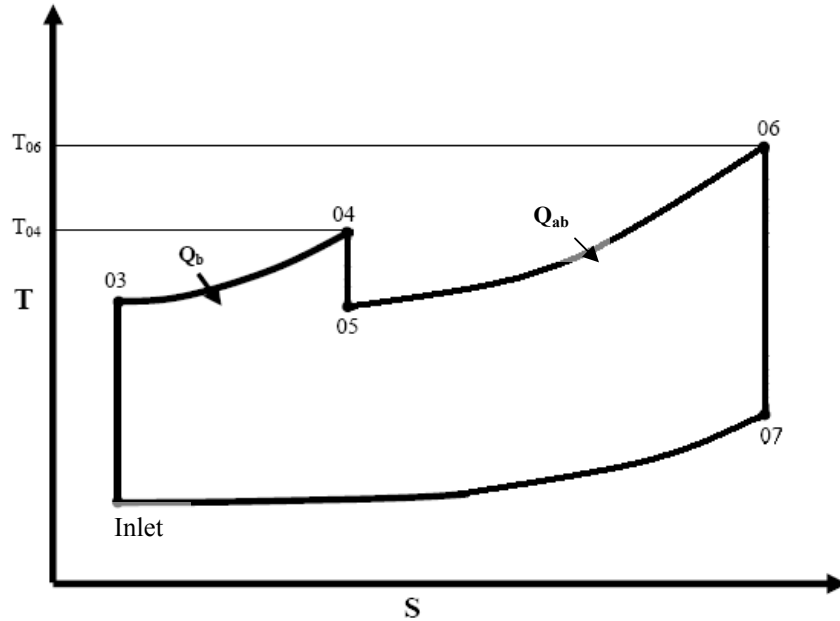
The primary zone is the initial area of combustion. It is an area of turbulence and recirculation into which high equivalence ratio flows are injected (Anisko, 2006:6). This provides a stable flame anchoring continuous and nearly-complete combustion (Moenter, 2006:8). Following the primary zone, air from the liner is injected into the intermediate

zone. The products of the fuel-rich primary zone contain higher-than-desirable levels of UHC and CO, and there are some pockets of fuel and air which have not yet reacted. With the injection of new air, these products can continue to react and harmful emissions are reduced (Anisko, 2006:6-7). The addition of liner air also serves to cool the exhaust somewhat, which recovers some of the dissociation losses occurring at elevated temperatures. At high altitude or low pressure conditions, the intermediate zone serves to extend the primary zone and increase the residence time for the reacting gases (Moenter, 2006:8).

Finally, the mixture flows into the dilution zone, where it is further cooled by the remaining air in the liner. Most remaining free radicals react in this region, and the non-reacting outgoing flow will have reached a mean temperature inducing less wear on the turbine downstream (Anisko, 2006:7).

### *Thermodynamic Cycle*

Combustors work by creating heat and entropy ( $s$ ) in the flow through chemical reactions, adding energy used by the turbines. This energy drives the compressor as well as any powered systems aboard the aircraft. Figure 9 shows a T-s diagram from the inlet to the exit of a conventionally designed gas-turbine engine. The line from the inlet to point 03 corresponds to the compression section, where temperature increases but entropy remains constant.



**Figure 9.** Engine cycle for a typical gas-turbine combustor (Adapted from Liu et al., 2000:9).

In the diagram,  $Q_b$  represents the heat added by a traditional in-line combustor. Both the temperature and entropy increase during this process. Between points 04 and 05, the turbines draw power from the flow and the temperature decreases. Point 06 represents the condition of the mixture when an afterburner is used to reheat it and provide more thrust. A major limiting factor for the performance of combustors occurs at point 04, where the temperature after combustion cannot exceed the maximum threshold for the turbine blades.

### 2.3 UCC Development

The UCC capitalizes on several theories in order to achieve the benefits it can provide. Combining them into a single design has led to a significantly smaller, high-performing combustor. The development process for the UCC has included both experimental and computational fluid dynamics analysis.

### *Centrifugally-Enhanced Combustion*

As mentioned above, Lewis' study published in 1973 showed significant increases in flame speed with high G-loading. By spinning pre-mixed fuel and air flows through a pipe combustor, forces up to 3500 G's were achieved. Using propane-air and hydrogen-air mixtures, flame speed increased with G-load and progressed through three modes of propagation. Moving through laminar and turbulent flame mechanisms, Lewis found above 500 G's flame speed followed a new relationship, defined in Equation 10 where  $S_B$  is the buoyant flame speed and  $G$  is the G-load on the flow (Moenter, 2006:11).

$$S_B = 1.25\sqrt{G} \quad (10)$$

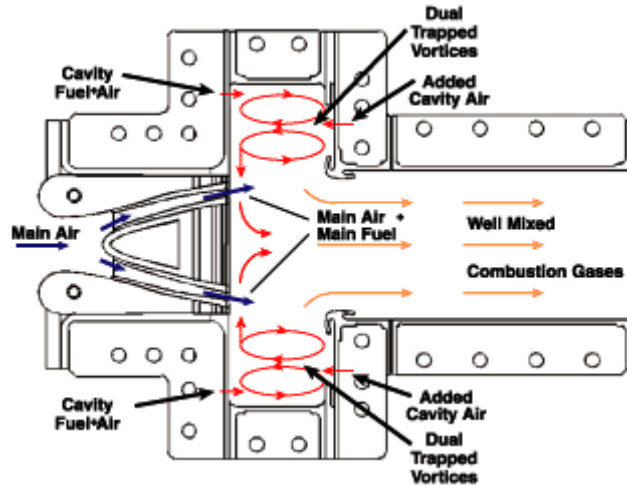
Lewis termed this new mode "buoyant bubble" flame transport because the G-load induces stratification in the mixture. The density difference between hot and cold air leads to hot air velocities surpassing normal turbulent flame speeds, thus transporting the flame at a rate above the capability of the turbulent flame mode (Moenter, 2006:11). Yonezawa examined this behavior further by using angled air injectors to induce a ring of swirling vortices (Anderson, 2007:11). This induced a G-load on the mixture, and the study found increased combustion efficiencies were achieved while also decreasing the necessary residence time (Anisko, 2006:48).

### *Trapped Vortex Combustion*

The idea of using standing vortices for the purposes of flame-stabilization has received much attention. For the environment inside a combustor, the most practical method of achieving this state is to allow vortices to shed from a main flow region into an offset cavity. Research done by Little and Whipkey showed, with the correct cavity size, a stable, non-reacting vortex could be locked in place (Little et al., 1979). Hsu further



investigated the Little and Whipkey findings by working with combustive flows. The study found reacting vortices could be locked into a cavity as well, and would serve as an efficient means of flame stabilization (Hsu et al., 1998). These and other studies showed the most favorable conditions for trapping a vortex in a cavity were when cavity flow rates were roughly 10-20% of the flow rate in the main channel (Moenter, 2006:11). A CFD study performed by Straub indicated certain vortex phenomena produced regions of higher temperatures when reacting, which affects the generation of  $\text{NO}_x$  (Straub et al., 2000). Overall, results of the research indicated TVC exhibits improved lean blowout (LBO) and high-altitude relight characteristics (Anisko, 2006:8). They also showed combustors utilizing TVC had wider operating ranges and decreased  $\text{NO}_x$  emissions (Greenwood, 2005:11). The UCC was designed with these results in mind, and utilizes TVC at the site of every fuel injector. As shown in Figure 2, the cavity-in-a-cavity concept is employed at these locations in order to provide flame stabilization. This allows for higher velocities inside the cavity, and thus higher G-loads, while still maintaining a region of stable and efficient combustion (Roquemore et al., 2001). Figure 10 shows the design for one of the TVC experimental research rigs.



**Figure 10.** A design for a TVC experimental research rig (Roquemore et al., 2001).

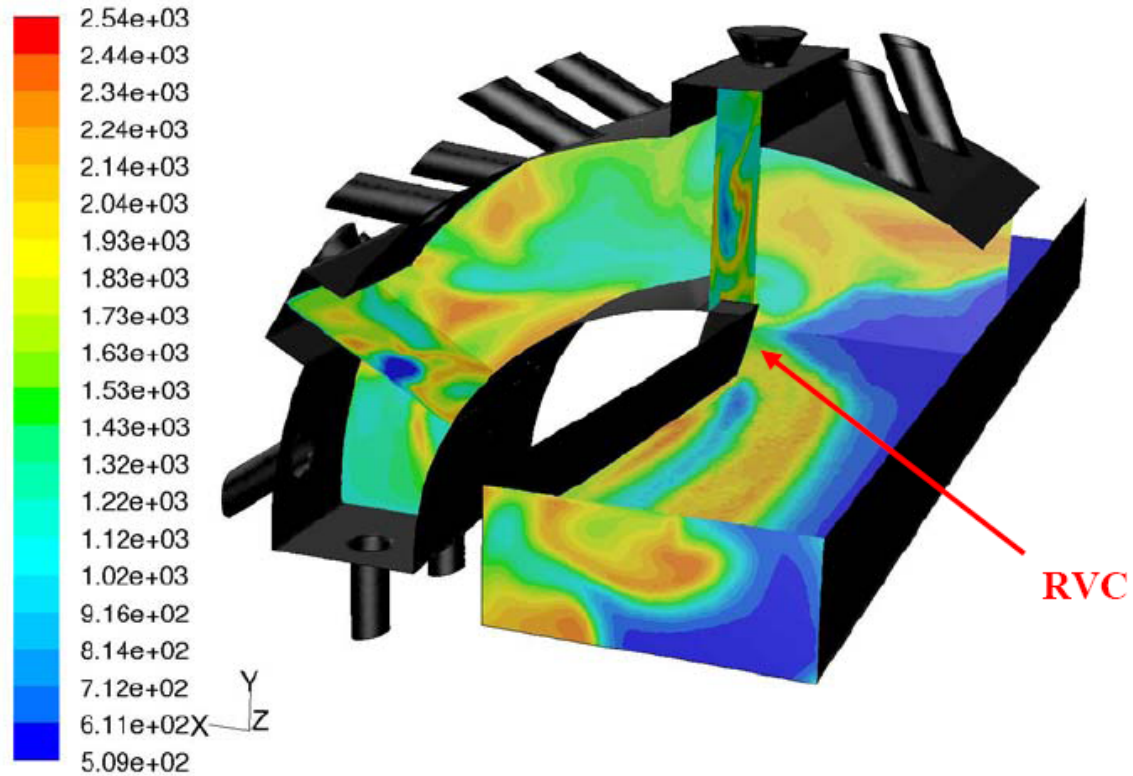
### *Design of the UCC*

As described above, the UCC is designed to use both centrifugally-enhanced and trapped vortex combustion extensively. With its circumferential design around the main axis of the engine and its angled air nozzles, high tangential velocities, and thus G-loads, are achieved. The CIAC concept utilizes TVC to maintain steady combustion even with the ignition system off and very high velocities in the main cavity area. Also, the vortices in the cavity are comparable to a traditional combustor's primary combustion zone. The six radial-vane cavities serve as the intermediate zone and provide a low-pressure turbulent wake to draw the hot products of the cavity down into the main flow (Hankins, 2008:13).

### *Computational Fluid Dynamics Research*

As CFD has developed in complexity and accuracy, it has played an increasingly important role in engineering research. The research surrounding the UCC is no

different, having used CFD extensively in the process leading up to the construction of actual experimental rigs to support combustor flows. Studies focused on predicting the flow mixing and combustion characteristics, as well as understanding the effects of combustor geometry on performance (Hankins, 2008:20-22). Anisko and Greenwood developed codes used to investigate and optimize the internal geometry of the UCC models, and compared their data to experimental data gathered by AFRL using a full-sized UCC (Anderson, 2006:6). Moenter's work built on that of Anisko and Greenwood, and focused more on the cavity-vane interactions inside UCC sectional models. Specifically, he developed CFD models for the infinite-radius (flat-cavity) and curved-cavity sectional rigs, and tested several operational conditions for each (Hankins, 2008:20-22). A plot of temperature contours for the curved section can be seen in Figure 11.



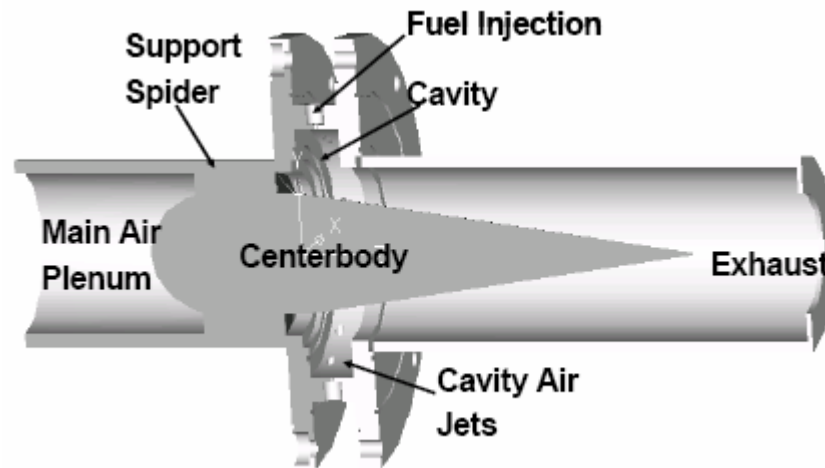
**Figure 11.** Curved UCC sectional rig developed by Moenter for CFD analysis. The plot shows temperature contours (K), with airflow to the right in the cavity and out of the page in the main vane (Moenter, 2006:112).

JP-8 was used as the fuel for all tests. (Moenter, 2006:57) Of note for this thesis, Moenter observed theoretical combustion efficiencies from 94.49-99.45%, pressure drops from only 1.15-7.86%, and average combustor exit temperatures from 1027-1073K. Maximum exit temperatures ranged from 2330-2347K (Moenter, 2006). These were promising figures for the combustor, and experimental work needed to be done to validate the CFD findings.

### *Experimental Research*

The UCC concept was developed at the AFRL Propulsion Directorate, and experimental work on the idea began in 2001. Initial tests conducted by Anthenien used

an atmospheric pressure rig with JP-8 and ethanol-based fuels, while varying the equivalence ratio (Anderson, 2007:11-12). The original UCC rig used is shown in Figure 12.



**Figure 12.** Schematic of the original UCC experimental rig. The support spider did not include an RVC design. Flow path is from left to right (Zelina et al., 2004).

This first study reported encouraging results. At loadings of approximately 1000 G's, observed flame lengths were reduced by 50% from traditional combustors, combustion efficiency was over 99%, and the system showed a wide operating range. LBO occurred at  $\phi = 0.5$ , and operation continued over  $\phi = 2$  (Anthenien et al., 2001). Work done by Zelina in 2003 investigated the effects of fuel injector type and injection angle. Results from this study indicated a strong dependence in efficiency on these properties, but observed pressure losses no greater than 2% and validated the expectation that increased G-loads in the cavity increased combustion efficiency (Zelina et al., 2003).

Laser Doppler Velocimetry (LDV) tests in 2003 measured tangential velocities in the cavity from 20-45 m/s, and induced G-loads from 1000-4000 G's. A CFD study by

Quaale coordinated with this research served to validate the CFD model. This study also found cavity velocity was insensitive to main vane velocity. Of note, higher CO emissions indices were recorded at higher G-loadings (Quaale, 2003:88). More recent studies have utilized a pressurized rig to more accurately simulate operational conditions (Zelina et al., 2005), and introduced the RVC concept into the rig (Zelina et al., 2004). All preceding data was gathered directly from the AFRL Propulsion Directorate by Greenwood.

The first sectional UCC experimentation was conducted by Hankins in 2007. Hankins tested a 2-D flat-cavity section of the combustor at several of Moenter's CFD test conditions. Important results from this study include observed combustion efficiencies above 99% at most conditions, although no G-load could be achieved without cavity curvature. Hankins also observed very different emissions results than predicted by Moenter when operating at the recommended conditions. Practical sources of error in the experiment included fuel pooling and a low volume of emissions data taken. Table 1 shows the results of Hankins' experimentation compared to Moenter's CFD predictions.

**Table 1.** Hankins' experimental efficiency and emissions data compared with that predicted by Moenter's CFD analysis at select conditions (Hankins, 2008:120).

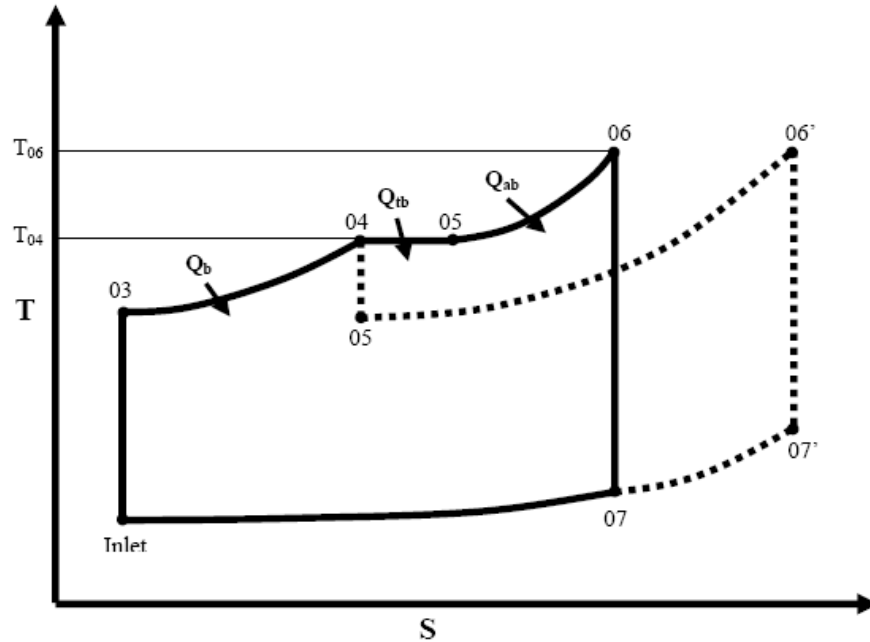
Condition	CO (ppm)	NO <sub>x</sub> (ppm)	UHC (ppm)	% O <sub>2</sub>	% CO <sub>2</sub>	$\eta_b$ (%)
EXP ATM1	1577.90	7.00	1740.00	18.84	2.08	99.88
CFD ATM1	2586.95	102.81	1.35	16.23	2.85	99.12
EXP ATM2	208.00	1.30	790.00	20.87	0.51	99.92
CFD ATM2	1665.53	42.43	0.72	16.01	3.05	99.45

#### 2.4 Use of the UCC as an Inter-Stage Turbine Burner

Research proposed and conducted at the University of California at Irvine has indicated operating a gas-turbine engine with a constant temperature cycle can provide

large increases in ST with little or no penalty in TSFC (Sirignano et al., 1997 and Sirignano et al., 1999). However, a true continuous-turbine burner (CTB) would require combustion in the turbine rotor (Liu et al., 2000), which currently available turbine materials are not capable of withstanding without immense costs (Anisko, 2006:9). An alternative method, proposed by Liu and Sirignano, is to burn fuel at the vanes leading to the turbine rotor, a concept they called inter-stage turbine burning (Liu et al., 2000). An ITB cycle would closely approximate the CT cycle, but does not exceed the limits of the turbine materials (Anderson, 2007:9). Their research showed adding a single stage ITB in a turbofan engine increased the specific thrust by over 50% with no TSFC increase (Liu et al., 2000).

The concept improves cycle efficiency by adding energy to the flow in a high-pressure region, which then proceeds to do work on the turbine rotor as the exhaust expands (Anisko, 2006:9). The ITB mitigates the thrust lost due to this work (Zelina et al., 2003). Figure 13 illustrates a gas-turbine engine cycle with (solid line) and without an ITB (dashed line), as well as some of the associated benefits.



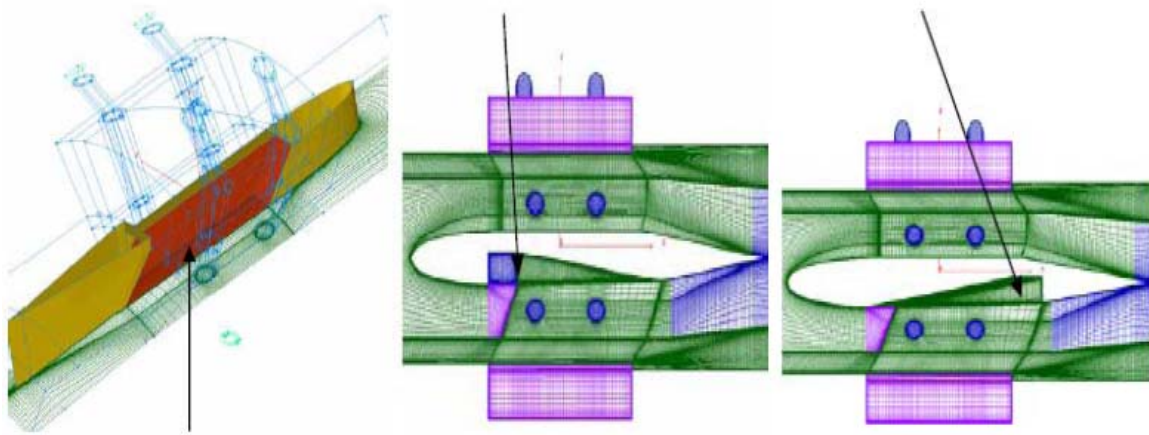
**Figure 13.** Thermodynamic cycle for an engine using an inter-stage turbine burner (solid line) overlaid on an example of a traditional gas-turbine cycle (dashed line) (Adapted from Liu et al., 2000:9).

Points 04 to 05 show the condition of the flow through the turbine, and confirm the temperature will not exceed that achieved in the main burner, thus increasing the life of the turbine section (Anderson, 2007:9). Figure 13 also indicates the length of the afterburner section needed to achieve the same end temperature is less due to the higher temperature at the turbine exit (Sirignano et al., 1999). Other benefits of the ITB concept include slower degradation in TSFC and ST with increasing Mach number, and engine operability at higher Mach numbers, increasing an aircraft's operational envelope (Sirignano et al., 1999). Conventional combustors would negate the benefits of adding an ITB because of their size, but the UCC provides a new alternative.

Critical to the operation of an ITB is the presence of radial-vane cavities. The exhaust gases created by combustion between turbines around the turning vanes must be



allowed to reach the main flow in order for the CT cycle to occur. An RVC accomplishes the extraction of the cavity flow into the main flow's exhaust (Thornburg et al., 2007). As previously described, the RVC creates a low-pressure wake drawing exhaust gases down into the main flow. CFD research investigated the best shape for the RVC, and Figure 14 shows several of the candidates tested.



**Figure 14.** CFD designs of various radial-vane cavity shapes (Mawid et al., 2006).

This research showed that an angled or forward-facing cavity provided the best entrainment and temperature characteristics (Thornburg et al., 2007). The UCC is designed with an angled RVC.

## 2.5 *Combustor Performance Parameters*

In order to quantitatively compare one combustor design to another, numerical performance parameters are needed. Of the eleven parameters suggested by Lefebvre, two are applicable to the current research.

### *Combustion Efficiency*

Combustion efficiency, usually given in terms of a percentage, is an important indicator of combustor performance (Moenter, 2006:33-34). It is a measure of how closely the device is operating to perfect, or ideal, combustion based on the energy released related to the energy available in the reactants (Hankins, 2008:24). For the current study, this quantity will be calculated with reference to temperatures and mass flow rates according to Equation 11 (Hankins, 2008:25).

$$\eta_b = \frac{1}{\dot{m}_f H_C} \left[ (\dot{m}_{air} + \dot{m}_f) C_p T_4 - \dot{m}_{air} C_p T_3 \right] \quad (11)$$

Here,  $\dot{m}_{air}$  and  $\dot{m}_f$  are the mass flow rates of air and fuel in kg/min,  $H_C$  is the fuel's lower heating value (LHV) in kJ/kg, and  $C_p T$  is the stagnation enthalpy in J/mol with  $T_3$  and  $T_4$  referring to the temperatures at the combustor's inlet and exit (Hankins, 2008:25).

### *Pressure Loss*

Pressure loss is also an important measure of not only combustor efficiency, but of the performance of the whole engine (Moenter, 2006:32). In a combustor, this drop comes from two components: hot and cold losses. Hot pressure losses occur due to the combustion process and flow acceleration as density decreases, as described by Equation 6 (Anisko, 2006:31). Cold losses come from friction and turbulence along the combustor walls (Hill et al., 1992). Equation 12 shows a method of calculating pressure loss accounting for the combined factors:

$$\frac{dP}{P} = 100 * \frac{P_3 - P_4}{P_3} \quad (12)$$

Where  $P_3$  is the absolute inlet static pressure and  $P_4$  is the absolute exit static pressure (Moenter, 2006:32).

### *Thrust Specific Fuel Consumption and Specific Thrust*

Specific thrust and thrust specific fuel consumption are frequently used as metrics to describe improvements in whole-engine performance when discussing the addition of the ultra-compact combustor. For the purposes of completeness, the relationships defining these terms are shown below in Equations 13 and 14 (Hunecke, 1997).

$$ST = \frac{T}{\dot{m}_{air}} \quad (13)$$

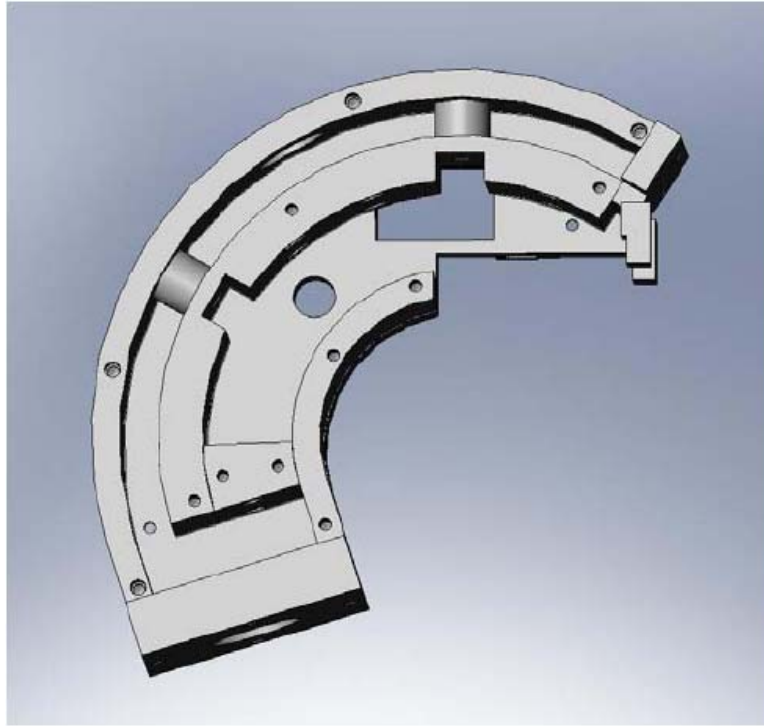
$$TSFC = \frac{\dot{m}_f}{T} \quad (14)$$

Here,  $T$  represents thrust in units of Newtons,  $\dot{m}_{air}$  is in units of kg/s, and  $\dot{m}_f$  is in units of kg/hr.

## **2.6 2-D Sectional Design**

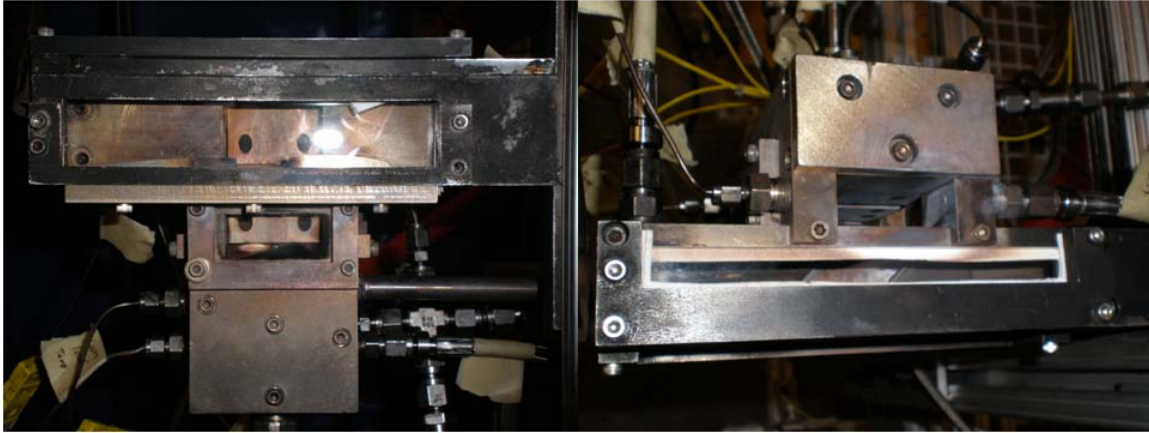
Previous research on the full UCC test rig has indicated a better understanding of the combustor's outflow temperature distribution is needed. The contributing factor of interest is the interaction between the main flow and the cavity flow, specifically at the radial-vane cavity locations. In order to truly understand the flow dynamics inside the combustor, non-intrusive diagnostic methods are needed. However, the geometry of the full 360-degree model precludes any method of laser diagnostics in this region. Thus, sectional operational models of the UCC are needed in order to investigate a more favorable geometry. An additional benefit of this sectional analysis is that by creating both a flat, "infinite-radius" cavity section and a curved section, an empirical study into

the effects of G-loading can be performed (Anderson, 2007:14). Figure 15 shows a cut-away view of the curved section.



**Figure 15.** Cut-away view of the curved cavity for AFIT's UCC sectional model (Hankins, 2008:7).

Important considerations in the design of these sectional rigs include the recreation of the main and cavity flows and mass entrainment, RVC, CIAC, and accurate fuel- and air-injection methods. Also, the addition of optically-clear quartz windows in several locations along the walls of the cavity and main vane is necessary in order to facilitate the use of lasers and optical observation methods. Figure 16 shows the flat-cavity model with quartz windows installed.



**Figure 16.** The AFIT 2-D sectional UCC model with quartz viewing windows installed at several locations.

Another design element available for these models is to embed half of the radial-vane into the non-viewing wall of the main vane. This enables the observation of just the interaction of the cavity and main flows with the RVC, rather than including the dynamics due to the open exhaust region, and simplifies the sectional designs (Moenter, 2006:43).

The sectional models are constructed of stainless steel to facilitate high operational temperatures (Anderson, 2007:73). Both are designed as 1/6 scale models of the full rig in order to match the COAL lab's air delivery capabilities (Dittman, 2006). The lab's compressors can provide up to 7 kg/min of air to the main vane and up to 2 kg/min to the cavity, both of which can be heated to 530K for improved lighting. Fuel delivery is accomplished by precision syringe pumps at a rate of up to 5.67 milliliters of JP-8 per second (0.0042 kg/s). Gaseous fuel delivery of ethylene ( $C_2H_4$ ) for the igniter and hydrogen ( $H_2$ ) for the actual combustor is provided by pressurized tanks through high precision mass flow controllers (Hankins, 2008:6).

Both the curved and flat sectional rigs have been constructed in the AFIT model shop, but the flat-cavity system was constructed first and is the section studied in this thesis.

## **2.7 Laser Diagnostics**

Laser diagnostic techniques receive much attention in the combustion field because of their non-intrusive nature. When high temperatures threaten to melt or disable traditional thermocouple or probe devices, or the dynamics of interest may be disturbed by the methods used for analysis, optical analysis can be used. There are many varieties of optical and laser diagnostic techniques, but this research focused on PLIF.

### *Planar Laser-Induced Fluorescence*

PLIF is a 2-D diagnostic technique introducing a plane of light created by a laser passing through cylindrical optics into a region of interest (ROI). This technique makes use of the molecular absorption and emission of energy in the form of light at high energy levels. In a general sense, a molecule absorbs a photon which excites the electrons of that molecule to a higher energy state. Following this excitation, the molecule naturally tends to relax back to a balanced electron configuration, releasing energy, again in the form of photons, in the process. This photon release is called fluorescence (Hankins, 2008:29). More specifically, fluorescence occurs when the energy emission occurs between energy states of the same spin, as opposed to phosphorescence, which occurs between energy states of opposite spin (Anderson, 2007:33). Fluorescent absorption refers to wavelengths of light which, when introduced upon a molecule, result in fluorescence at a different wavelength.

Research has shown there are many molecular candidates for the PLIF technique involved in combustion exhibiting usable absorption and emission characteristics. Table 2 shows the fluorescent absorption range for species of interest.

**Table 2 .** Wavelength spectra open to fluorescent absorption for species of interest in combustion diagnostics (Eckbreth et al., 1979:260-265).

<b>Molecule</b>	<b>Electronic Transition (nm)</b>
C2	230-330 400-600
CH Radical	360-450 430-500
CO	150-240 200-250
N2	100-500 Vac u.v.
NO	195-340 200-500
O2	170-220 500-900
OH Radical	240-400
CH4	145.5-500
C2H2	210-237
CO2	140-170
H2O	145-186

Scrutiny of the above table shows a characteristic ultra-violet (UV) range for each species' absorption spectrum. This range is easily accessible for common lab equipment (Anderson, 2007:37), and thus PLIF is a widely used technique (Kohse-Hoinghaus, 1994:203-279). The reality of quantum mechanics is that only certain discrete wavelengths within the above ranges function for the purposes of PLIF, and theory-based

computer programs such as LIFBASE must be used in order to find the correct lines (Anderson, 2007:36). This program will be discussed in more detail later.

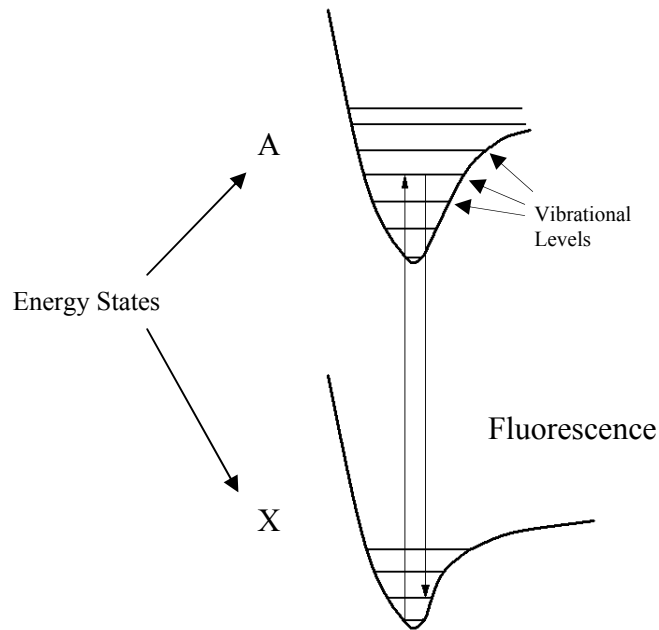
The abundance of the hydroxyl (OH) molecule in high temperature combustion processes and its associated long fluorescence time - between  $10^{-10}$  and  $10^{-5}$  seconds - make it a prime candidate for PLIF studies in combustive environments (Eckbreth, 1988:14). The absorption and emission lines of OH are generally termed the OH (A-X) electronic transition system, and will be discussed in the following section (Hankins, 2008:31).

OH PLIF has a range of uses, including acting as a flame marker for flame location studies, temperature measurement, and determining OH species concentration (Hankins, 2008:31). The fluorescent intensity of a species' photon emissions is approximately linearly related to its concentration in the ROI, and thus is the quantity measured in PLIF studies (Anderson, 2007:34). The intensity of the light emitted can be measured using specially designed and tuned cameras.

### *PLIF Thermometry*

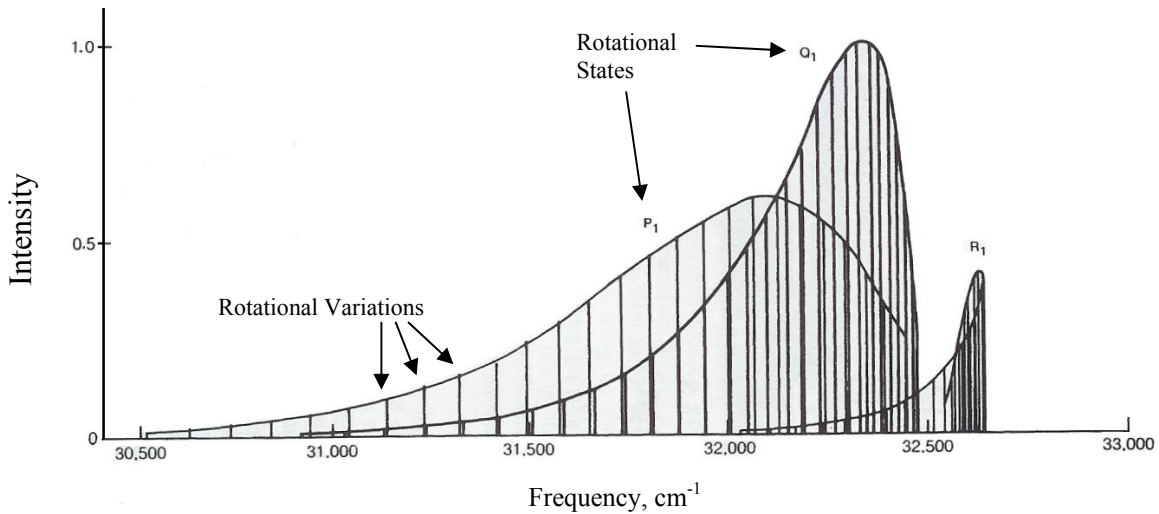
Planar laser thermometry studies play an important role in the evaluation of combustion dynamics, offering insight into regions where unburned pockets of gas may exist and indicating the temperature distribution across a region of interest (Seitzman et al., 1994). OH PLIF provides these benefits by making use of the OH (A-X) electronic transition system (Hankins, 2008:31). This term designates the energy states being manipulated by the incident laser sheet, as shown in Figure 17.





**Figure 17.** The X and A energy states with sub vibrational levels shown. Rotational levels are not shown. Vertical arrows designate increasing and decreasing energy (Adapted from Eckbreth et al., 1998).

The figure shows the X energy state as the ground state for electrons in the OH molecule, and the upward arrow designates their excitation to the higher A energy state. The horizontal lines represent the vibrational levels within each energy state. These levels are written after the (A-X) designation in common notation, as OH (A-X) (1-0) or (1,0), with different numbers representing different levels. Not shown in Figure 17 are the rotational states within each vibrational level (Eckbreth et al., 1998). These states further quantize the description of an electron's condition, and are the level at which PLIF excites subject molecules. As shown in Figure 18, there are many rotational states within each vibrational level, with multiple variations on the rotation.



**Figure 18.** An example of the rotational structure of a vibrational level (Adapted from Eckbreth et al., 1998).

Rotational states are designated by letter and number combination followed by the specific variation in parenthesis, as  $Q_1(5)$  (Eckbreth et al., 1998). These states are excited by specific wavelengths of incident light, and are generally referred to as “lines.”

Two methods of PLIF thermometry are used in order to perform the laser system calibration. The first examines the ratio of fluorescent intensities produced by two different wavelengths of light. These two wavelengths are known as line pairs, and are selected for their sensitivity to temperature and wavelength proximities. By choosing one line which is insensitive to temperature and another which has an intensity varying greatly with temperature, the fluorescent intensity ratio of these two lines can be correlated with theoretical data generated by LIFBASE in order to determine temperature (Hankins, 2008:31). The use of LIFBASE is discussed in Section 3.4. Previous work referenced on intensity-ratio OH PLIF thermometry has examined several line pairs, all in the OH (A-X) (1-0) vibrational level. An example study conducted by Seitzman, Hanson, and others used three line pairs to observe a hydrogen-air flame with a

temperature range of 1000-3000 degrees Kelvin (Seitzman, 1994). The line pairs used were as follows:  $Q_2(11) - R_2(5)$ ,  $Q_2(11) - P_1(7)$ , and  $Q_2(11) - R_2(8)$ . The wavelengths for these lines were:  $Q_2(11) - 285.16$  nm,  $P_1(7) - 285.09$  nm, and  $R_2(8) - 281.72$  nm. Using the  $Q_2(11) - P_1(7)$  pair, temperatures were measured with as low as 7% error (Hankins, 2008:32), a level of accuracy valuable for engine research. The Hankins research examined seven line pairs, the results of which will be referenced in Section 4.1 (Hankins, 2008:83).

The second method of PLIF thermometry is called an excitation scan. After selecting a line of interest from LIFBASE, the incident laser is tuned in small increments through a range of wavelengths just below and above the peak (Hankins, 2008:31). The recorded fluorescent intensities, when plotted versus wavelength, show the “shape” of the line. This line shape also depends on temperature, and thus can be correlated again with LIFBASE data in order to determine flame temperature (Hankins, 2008:31). This method in particular requires several correction factors for accurate readings, however.

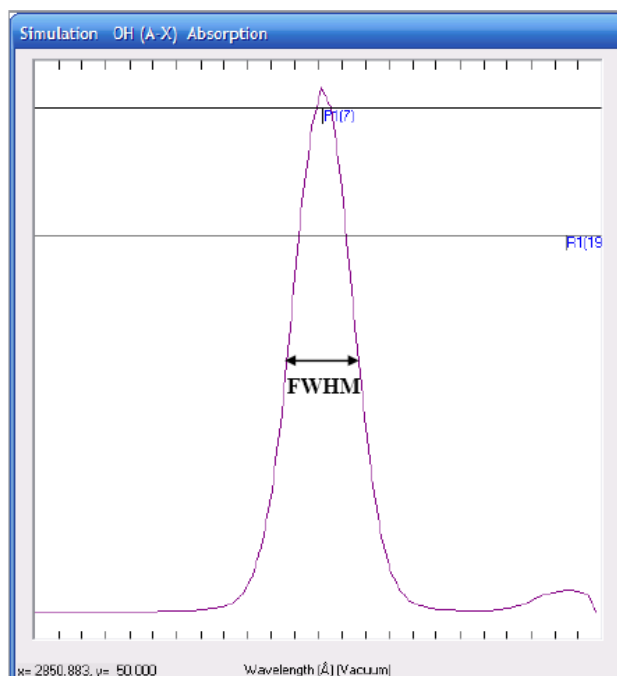
The first of these corrections accounts for laser, or line broadening. Although the lab laser may be tuned to a specific wavelength, it is actually emitting a very small range of wavelengths termed the “line-width” (Eckbreth et al., 1998). This property limits the resolution, and thus accuracy, with which the OH line’s shape can be determined.

The second correction factor accounts for Doppler broadening, which is a function of temperature. This type of broadening is a result of the small-scale motion of the radiating molecules. Based on the Doppler principles, particles moving toward the collection device will appear to emit at a higher frequency, while those moving away will

produce an apparent lower frequency (Eckbreth et al., 1998). Thus, a range of frequencies wider than those actually emitted is recorded.

The third source of error is called collisional, or pressure broadening. This is a factor of molecules colliding with each other as they interact with radiation, interrupting the absorption or emission process (Eckbreth et al., 1998). Line-width can be experimentally measured, and Doppler broadening can be calculated by LIFBASE based on the anticipated temperature predicted by an equilibrium kinetics code such as STANJAN, so collisional broadening can be empirically determined. This allows all three correction factors to be applied to recorded data.

Since line shape is the quality of interest for the excitation scan, a method of quantitatively analyzing these shapes must be used. The technique used in the current study evaluates the full-width, half-maximum (FWHM) values of recorded line shapes. Figure 19 shows an illustration of this method using LIFBASE.



**Figure 19.** Illustration of the full-width, half-maximum method for excitation scan analysis. Image generated by LIFBASE (Hankins, 2008:66).

This method is accomplished by determining the width of the line in wavelength at half of its peak intensity. The FWHM value provides a repeatable technique to characterize the line width. This value is a function of temperature, and when correlated with LIFBASE data provides a useful technique for measuring this variable (Hankins, 2008:31).

### *Quenching and Power Corrections*

Two correction factors are needed in order to normalize all fluorescent intensity data and reveal an accurate trend of the flame's state. The first accounts for a condition known as quenching. Quenching is the general term describing three possible occurrences that prevent the emission of fluorescent spectra by molecules excited to a higher energy state. These occurrences include “dissociation, energy transfer to another

molecule or internal energy state, [and] general chemical reaction[s]” (Hankins, 2008:30). Very accurate analytical correction factors exist based on species densities and known quenching processes. A method published by Tamura et al. will be used for the current study, and is addressed in Section 3.4 in detail (Tamura et al., 1998:502-514).

### *Laser Structure*

In order to provide the power and wavelengths necessary at the location of the flame studied, the COAL lab’s current laser system uses a pump laser, a tunable dye system, and frequency-doubling crystals. The pump laser is a dual-pulsed neodymium-doped yttrium aluminum garnet (Nd:YAG) laser providing an initial infrared beam to the rest of the laser system. More technically, the unit is a flash lamp-pumped, Q-switched Nd:YAG laser. Using two flash lamps - hence the dual-pulsed designation - the system excites triply ionized neodymium, which emits photons at 1064 nm. Q-switching blocks and restores beam feedback in order to provide increased peak output power from the unit (Spectra, 2001). More details on the lasing process can be found in Hankins’ thesis (Hankins, 2008:25-28).

The infrared beam from the YAG is then passed through a series of frequency-doubling units and a tunable dye system. By altering the concentration of a methanol Rhodamine 590 dye pumped into cells placed in the beam path, the dye system allows the output frequency of the entire system to be adjusted at very small intervals. This provides the precision necessary when conducting combustion laser diagnostics. Frequency-doublers placed in the beam path emit light at both the same and double the incident frequency, cutting one beam’s wavelength in half. The COAL lab’s frequency-doublers are potassium dideuterium phosphate (KDP) crystals (Hankins, 2008:28).

### III. Methodology

#### 3.1 Objective Achievement

1. *Lab Enhancements.* Hankins suggested several modifications to the COAL lab based on the testing performed immediately prior to this research. Other major redesign tasks are important to the optimization of the lab's performance. Before any research can progress, these tasks must be completed and functionality of all systems verified.
2. *Calibration and Validation of PLIF System.* Following the enhancement of the COAL lab, the PLIF laser system needs to be calibrated and tuned. Extensive knowledge of the laser system not available during the Hankins research will allow the system to be even more precisely aligned and adjusted. A laminar hydrogen-air flame produced by a Hencken burner will again be used in conjunction with theoretical data in order to validate the system.
3. *Igniter Characterization.* The Hankins research revealed difficulties in the use of the ignition system. Specifically, a consistent and steady regime was not found for the igniter's operation. This system is critical to the consistent and reliable operation of the UCC model, and needs to be fully understood for future UCC research.
4. *PLIF in Cavity-Vane Interaction Region of UCC Section.* A PLIF study investigating flow and combustion dynamics in the cavity-vane area will be conducted. The effects of equivalence ratio and cavity-to-main flow rate ratio will be investigated. Multiple planes will be observed in the UCC in order to provide a complete picture of the dynamics in the region.

5. *Dual-Vortex Behavior Observations.* A visual study using a high-speed camera will be conducted in order to observe and characterize the dual-vortex behavior discovered during the Hankins research. This behavior was predicted to signify an increase in the performance of the combustor and an operating regime for its occurrence must be defined.
6. *Performance Calculations.* Temperature and pressure data from the UCC section will be gathered using Lab-View in order to determine pressure drop across the cavity and an approximation of combustion efficiency.

### **3.2 Major Laboratory Alterations**

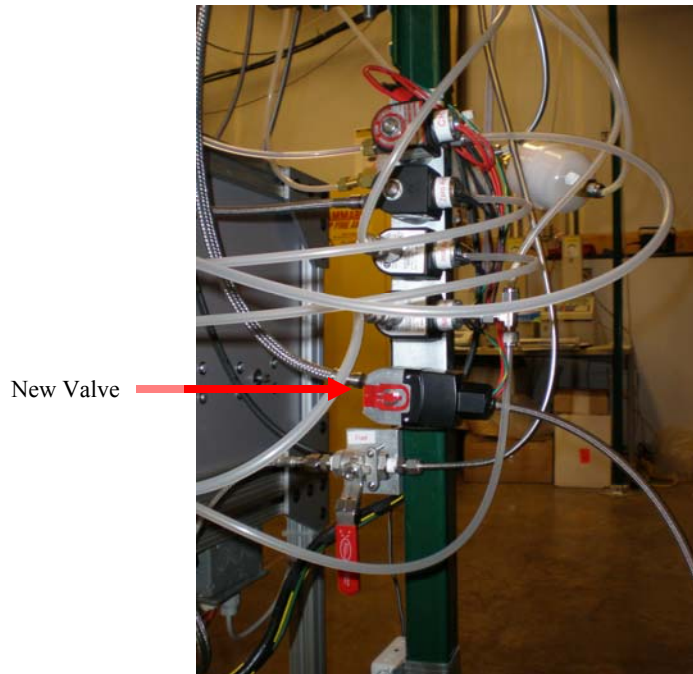
As Hankins noted, two items were absolutely necessary for the progression of combustive testing in the COAL lab. For safety reasons, the ventilation system's capability needed to be increased and an electric fuel shut-off valve, which could be operated from the Lab-View control station, needed to be installed just upstream of the combustor. To accomplish improved ventilation, a second fan was added in line with the one already in place. The fans (Figure 20) are 41 cm Dayton tube-axial models and pull about 108,000 SLPM. The modification nearly doubled the capability of the exhaust system.





**Figure 20.** One of the 16” Dayton exhaust fans.

The fuel shutoff valve was added at the same location as several other electric solenoid gas valves next to the test stand. Figure 21 shows its location.



**Figure 21.** Asco electronically-operated solenoid valve used for remote fuel shut-off.

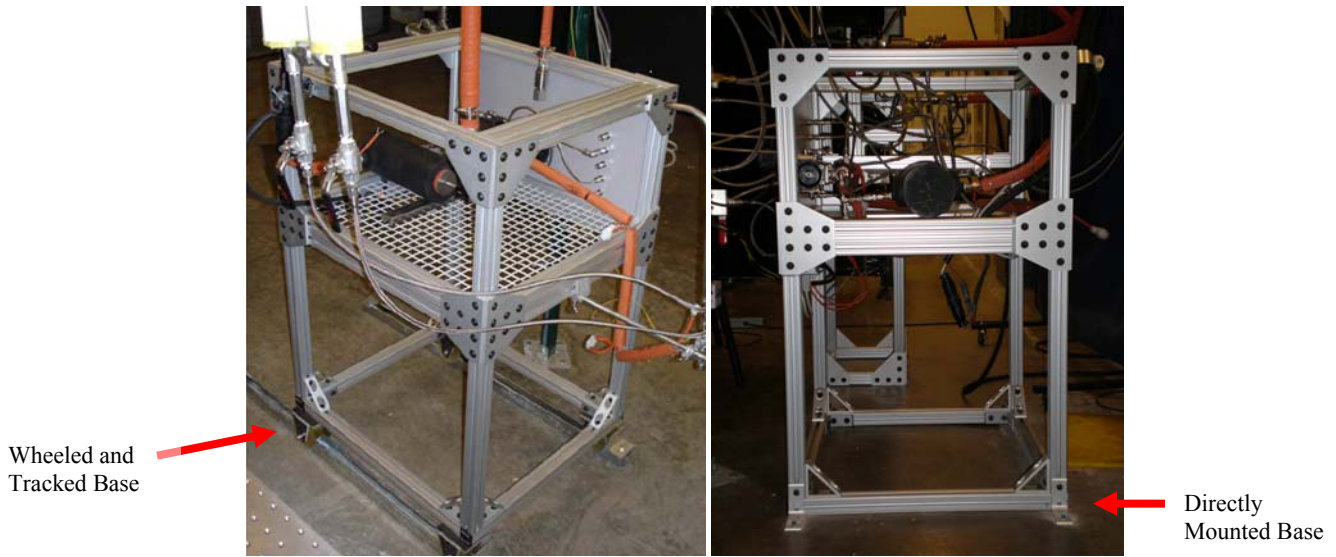
A controlling toggle switch was also added in the Lab-View control virtual instrument (VI), which will be discussed later. The addition of this valve and its associated toggle switch ensure the ability of any user to safely shut down the entire system from a distance in case of fire. The valve is an Asco electronically-operated, normally closed 2-way solenoid valve.

Aside from these safety-mandated alterations, experience during Hankins' research showed several other modifications could enhance the capability of the lab. The first of these is the addition of an electric actuator for the exhaust system. This actuator allows users to transition ventilation between the UCC test stand and the neighboring High Velocity, Open-Flame facility safely. The switch and actuator are shown in Figure 22.



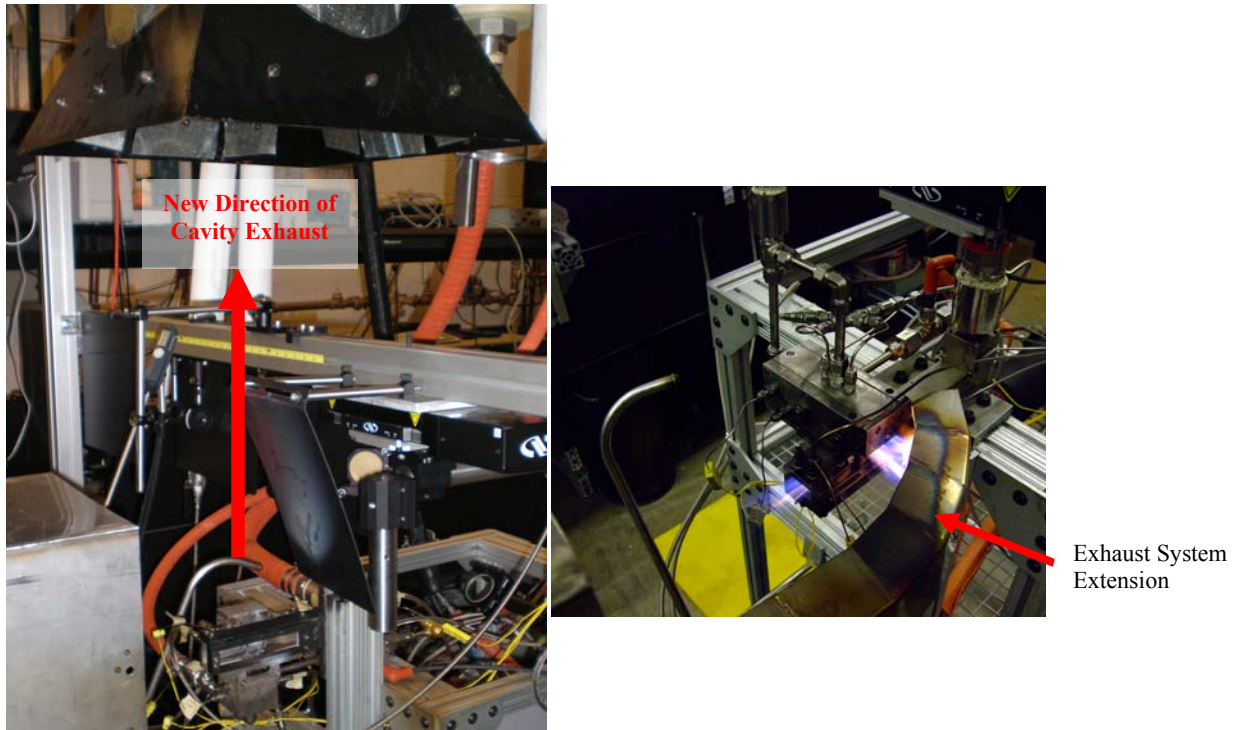
**Figure 22.** Electric damper switch and actuator.

The next task was to mount the test stand directly to the floor. It was originally thought that designing the test stand on a wheeled track would give the COAL lab a modular capability and allow the quick exchange of test apparatuses. With the high flow rates and violent nature of the anticipated testing, however, vibrations allowed by an unfixed base became a greater concern. Thus, the wheels and tracks were removed, and the stand was bolted directly into the lab deck. This shortened the stand, and the entire set-up needed adjustment to match the new height. Figure 23 compares the two designs.



**Figure 23.** Original design (left) of the COAL lab’s test stand next to the new configuration (right) with wheels eliminated (Anderson, 2007:70).

Another safety- and practicality-related modification required the cavity to vent directly up into the exhaust hood, as opposed to its original design involving an extension on the exhaust system. Figure 24 shows the difference between the two set-ups.

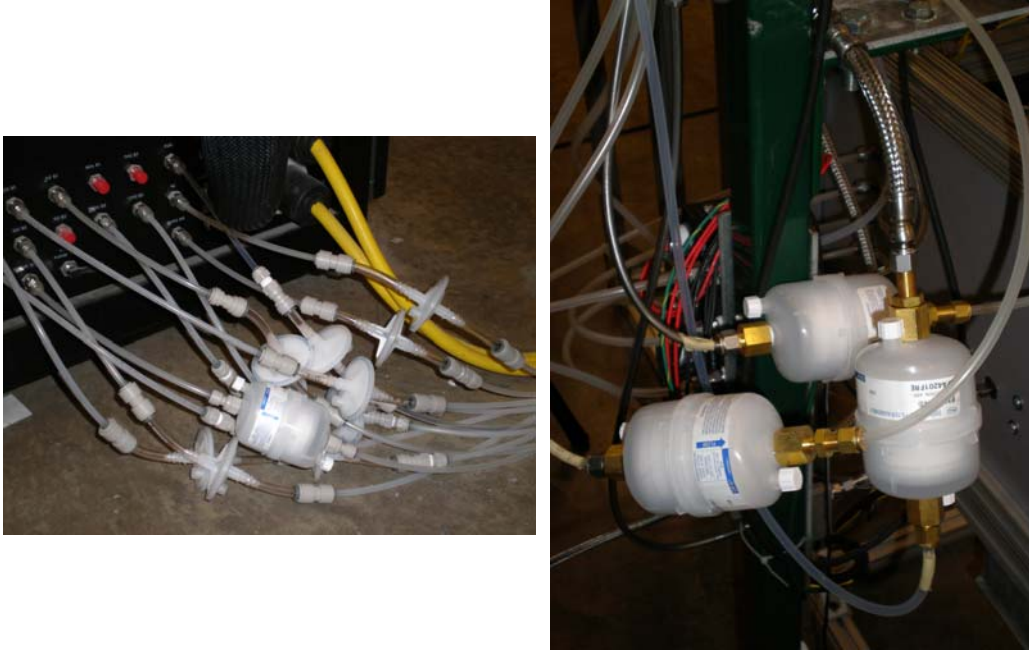


**Figure 24.** New configuration of the UCC section (left), with cavity exhaust oriented straight up into ventilation system, compared to the old configuration (right) which used an extension to redirect the exhaust from the cavity (Hankins, 2008).

This re-alignment of the combustor entailed an extension of the air delivery system and its insulation, exchanging rigid stainless steel lines for flexible metal and Teflon lines, and a new mounting configuration.

An additional alteration needed was discovered in the process as well. During previous research, a mass flow controller malfunctioned due to particles from an unfiltered gas line lodging in the controller’s internal components, requiring an expensive factory repair. This incident led to the requirement to have all gas lines filtered at the appropriate level immediately prior to the introduction of that gas into any sensitive system. The incorporation of these filters into the COAL lab is shown in Figure 25. In conjunction with the installation of the filters, the tank farm in which the gases are kept

had to be reconfigured for improved accessibility and safety. Appendix A shows the new configuration.



**Figure 25.** The incorporation of filtration units at two different locations in AFIT’s COAL lab.

Additional adjustments and repairs were performed during experimentation as needed, but no other major alterations were required.

### **3.3 Operation of Combustive Systems**

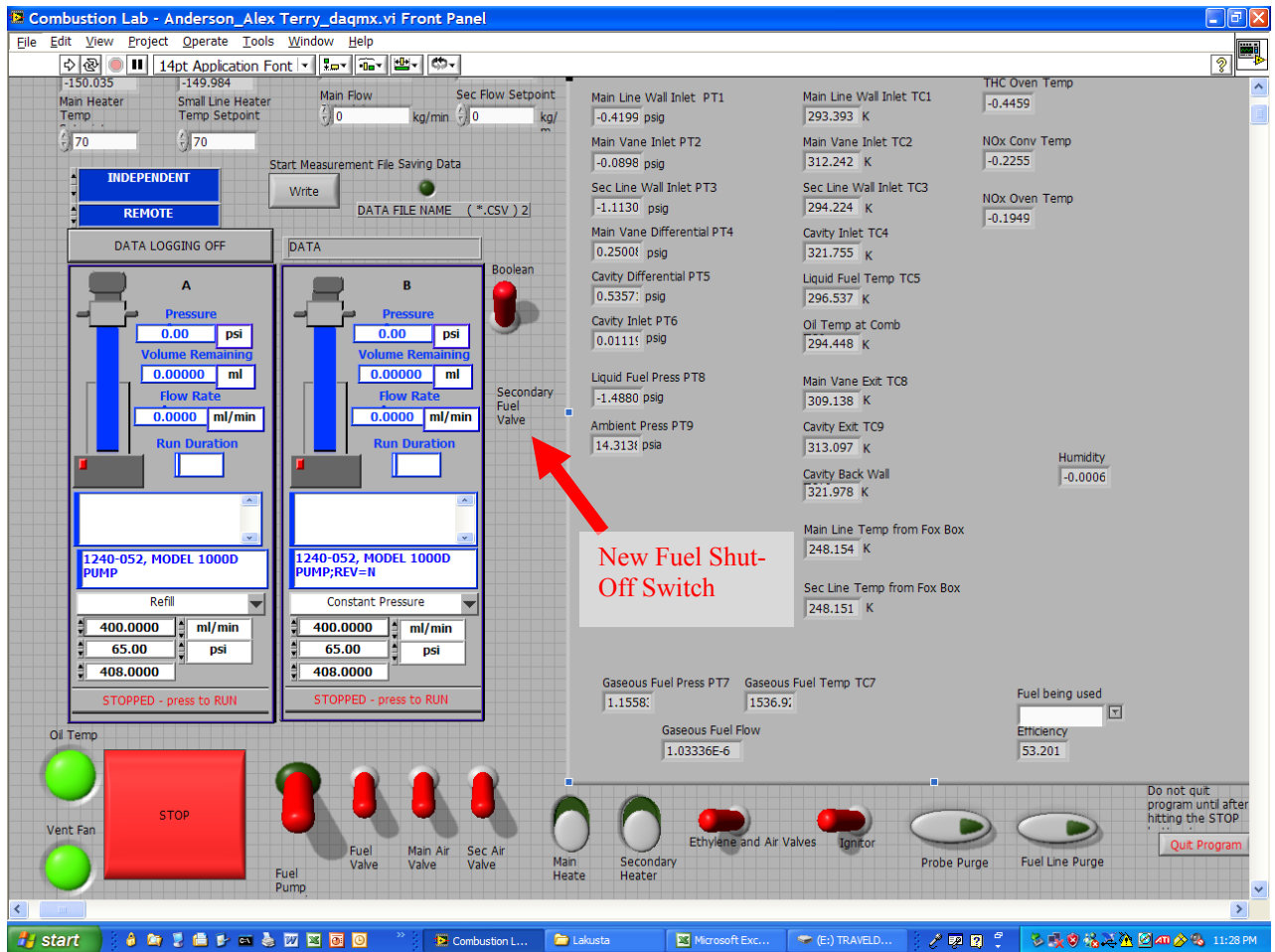
The research covered in this thesis involves the use and observation of three different combustive systems, each with its own experimental set-up and gas requirements. However, the COAL lab’s state-of-the-art design allows all three systems to be set up and controlled from the same central control station, using the same delivery equipment. This station is shown in Figure 26. Updated operating procedures for the lab are included in Appendix B.



**Figure 26.** Central control station for AFIT's COAL lab.

### *Lab-View*

National Instruments' Lab-View program provides the basis for the COAL lab's control and data acquisition capabilities. The VI interface designed by Anderson and shown in Figure 27 controls all air and fuel delivery to the test stand, most associated adjustments to the state of these flows, and is the hub for much of the data acquired directly from the UCC system.



**Figure 27.** Lab-View VI control interface. Arrow points to new fuel toggle switch.

The theory governing the function of the pressure transducers and thermocouples used for data acquisition is discussed in Anderson's thesis (Anderson, 2007:23). The output function for all data gathered in Lab-View is also updated to provide a more organized and readable format, solving the need for the output key in Appendix E of Hankins' thesis.

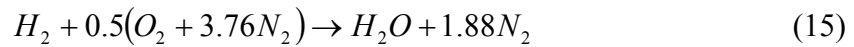
### *Theoretical Calculations*

Successful combustion operations and the evaluation of data require the application of the correct theory to the results. Two theoretical situations, complete and



equilibrium combustion, must be calculated and used in order to perform the research described. The theory for these conditions is addressed in Section 2.1, and their practical application is discussed here.

The calculation of equivalence ratio provides the data users need in order to determine the equipment settings necessary to accomplish a range of flame states. This parameter was calculated for two fuels: H<sub>2</sub> for the Hencken burner and UCC section, and ethylene for the igniter.  $\phi$  was varied in the tests on all three systems. For hydrogen, the balanced chemical reaction is written as:



Using Equation 4, the volumetric air-to-fuel ratio at  $\phi = 1$  is:

$$\left(\frac{A}{F}\right)_{ST} = 4.76(0.5) = 2.38 \quad (16)$$

For air held constant at 40 SLPM, Equation 5 shows fuel flow rate varies with equivalence ratio according to the following relationship:

$$F = \frac{40\phi}{2.38} \quad (17)$$

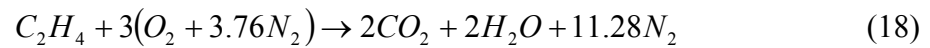
Hydrogen flow rates calculated using this method and used in Hencken burner operations are tabulated in Table 3.

**Table 3.** Equivalence ratio and fuel flow rate data for a hydrogen-air flame with the air flow rate held constant at 40 SLPM.

$\Phi$	Fuel (SLPM)
0.4	6.72
0.5	8.40
0.6	10.08
0.7	11.76
0.8	13.45
0.9	15.13
0.92	15.46
0.94	15.80
0.95	15.97
0.96	16.13
0.98	16.47
1	16.81
1.02	17.14
1.04	17.48
1.05	17.65
1.06	17.82
1.08	18.15
1.1	18.49
1.2	20.17
1.3	21.85
1.4	23.53

The same process was used to calculate data for the ethylene-air ignition torch.

Equation 18 shows the balanced chemical reaction:



Using Equation 4 results in:

$$\left(\frac{A}{F}\right)_{ST} = 4.76(3) = 14.28 \quad (19)$$

Holding air flow rate constant at 10 SLPM, rearranging Equation 5 results in:

$$F = \frac{10\phi}{14.28} \quad (20)$$

Ethylene flow rates used for igniter tests were calculated in this manner and are shown in Table 4.

**Table 4.** Equivalence ratio and fuel flow rate data for an ethylene-air flame with the air flow rate held constant at 10 SLPM.

$\Phi$	Fuel (SLPM)
0.3	0.21
0.4	0.28
0.5	0.35
0.6	0.42
0.7	0.49
0.8	0.56
0.9	0.63
1	0.70
1.1	0.77
1.2	0.84
1.3	0.91
1.4	0.98
1.5	1.05
1.6	1.12
1.7	1.19
1.8	1.26
1.9	1.33
2	1.40
2.1	1.47
2.2	1.54
2.3	1.61
2.4	1.68
2.5	1.75

Theoretical equilibrium calculations were accomplished using STANJAN (Reynolds, 1995). For a hydrogen-air flame, OH species concentrations and adiabatic flame temperatures were calculated for a range of equivalence ratios at standard temperature and pressure.  $\phi$  variations were calculated by holding the number of mols of hydrogen constant while varying the mols of air. The results were used to correlate experimental data gathered using the OH PLIF technique in the Hencken flame in order

to calibrate the laser system. An example of a STANJAN calculation is included in Appendix C.

### *Mass Flow Controller Calibration and Operation*

Control of the flow rates for every gas or liquid entering the combustive systems in the COAL lab is of vital importance in order to gather accurate and precise data. The theory governing several of these control methods is discussed in Anderson's thesis (Anderson, 2007:22). Aside from the shop air flow control system, all gases fed into the combustors are controlled and metered by MKS ALTA digital mass flow controllers, shown in Figure 28.



**Figure 28.** Several of the MKS ALTA digital mass flow controllers used in the COAL lab. The black arrow points to the zero reset button (Hankins, 2008:48).

Each controller is designed to allow a certain maximum flow rate through, and several different capacities were used for each of the three systems tested. Maximum flow rates of the controllers used include 5, 10, 30, and two 50 SLPM controllers

operating with H<sub>2</sub>, C<sub>2</sub>H<sub>4</sub>, zero air, nitrogen (N<sub>2</sub>), and argon (Ar) for a short period. Because of sensor drift and the frequent interchange of gases through the same flow controllers, the controllers needed to be recalibrated on a regular basis. The procedure for this calibration follows below.

The COAL lab ALTA units are operated by an MKS Type 247 4-Channel Readout display, shown in Figure 29. This unit allows users to adjust the controllers' flow settings in either percentages of total flow capacity or SLPM, with the percentage method being easier to use with the calibration curves (Hankins, 2008:49).



**Figure 29.** MKS Type 247 4-Channel Readout used to operate the MKS ALTA digital mass flow controllers (Hankins, 2008:49).

It is first necessary to turn this system on and allow the controllers thirty minutes to warm-up. Once ready, the units must be zeroed out. This is accomplished by ensuring a zero-flow condition through the controller by covering both inlet and exit. Once this state is achieved, the zero reset button on top of the unit itself may be depressed, re-seating the controller in its no-flow position (Hankins, 2008:48). With the actual controller zeroed, the display should now read zero flow. If this is not the case, the appropriate channel's tuning knob on the back of the Type 247 unit must be adjusted until a zero reading is displayed. An important fact noted in both the Hankins study and

the current research is that with positive pressure applied to the inlet of these controllers, it is possible for them to allow a small flow through, sometimes reaching as high as 0.9% (Hankins, 2008:49).

At this point, it is necessary to calibrate the settings and associated flow rates through the controller. A separate flow calibration unit, the BIOS Definer 220-H, was used to accurately and precisely measure flow rates. This unit, shown in Figure 30, is attached in-line downstream of the flow controller. When placed in “Continuous” mode, the Definer will take measurements as long as gas is flowing.

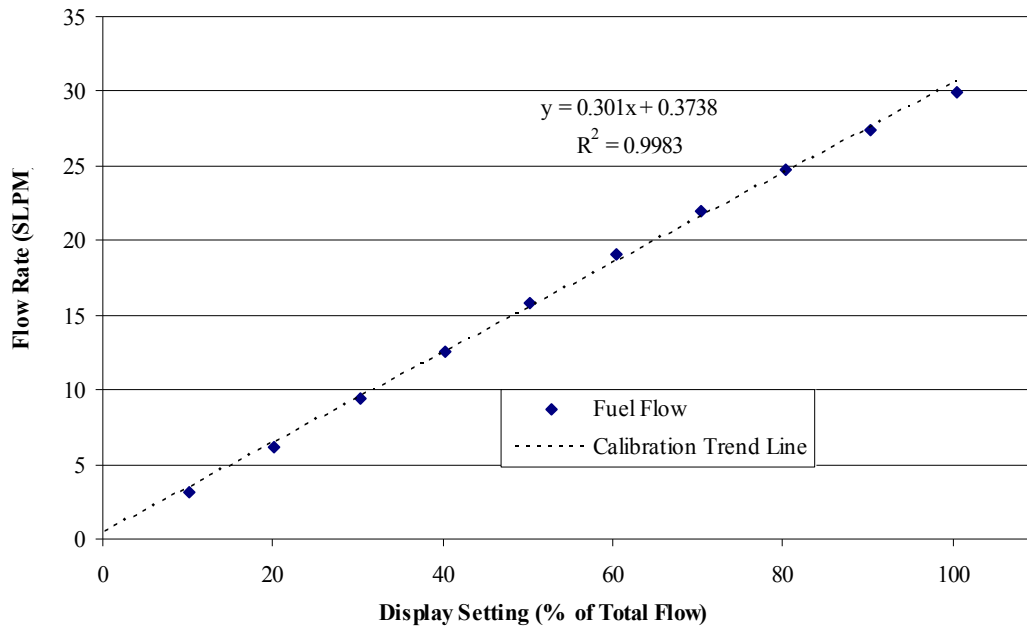


**Figure 30.** BIOS International Corporation Definer 220-H flow meter used for calibration of the MKS ALTA digital mass flow controllers (Hankins, 2008:50).

The ALTA controllers are calibrated at the factory for use with a certain type of gas. When a controller and its appropriate gas are paired, a table of gas correction factors shipped with the unit is used to predict the flow rates at different settings. When recalibrating, these numbers are used to tune the display’s readout. A range of flow settings should be tested in order to assure the linearity of the valve response. Testing a flow setting is accomplished by holding the appropriate channel’s “Set Point” switch in the up position while setting the desired flow rate with the screw to the right of the

switch. Once the setting is established, the Set Point switch should be placed in the “Read” position, and that channel’s operating switch turned to the “On” position. The Definer will take ten measurements and report an average matching the anticipated flow rate calculated for the setting. If this is not the case, the tuning knob should be adjusted until the setting matches the measured flow rate. This process must be repeated at multiple settings in order to assure complete calibration. Once the settings and average flow rates correlate, the controller is ready for use.

When a controller is used to meter a gas for which it was not pre-calibrated, a different procedure is followed. In this situation, it is necessary to characterize the new gas-controller pair. This is accomplished by measuring a full range of flow settings on the controller and tabulating the average flow rate at each setting. The settings and measured flow rates can be correlated to create a plot like the one shown in Figure 31. With the data plotted, a fitted trend line provides an equation describing the linear relationship. This equation is a formula for calculating the setting necessary on the Type 247 Readout to achieve a desired flow rate.



**Figure 31.** Calibration plot of hydrogen settings and corresponding flow rates on a 30 SLPM MKS ALTA digital mass flow controller.

This method was used to control nitrogen, zero air, and argon on 50 SLPM controllers, hydrogen on a 30 SLPM controller, and ethylene on a 10 SLPM controller.

### *Hencken Burner Operation*

The Hencken burner is a simple system, which generates a laminar, pre-mixed flame used in this research to calibrate the laser system. Because the flame is laminar, temperature measurements with only a single laser are possible using both the intensity ratio and excitation-scan method. The distributed flame is well characterized, and for each equivalence ratio allows data gathered through PLIF to be correlated to operating conditions. The procedure for operating the Hencken burner is described below.

First, as described in the mass flow controller calibration section, it is necessary to turn on the MKS Type 247 4-Channel Readout unit in order to allow the flow controllers



their thirty-minute warm-up. At this time, the laser should also be turned on in order to allow it at least fifteen minutes of warm-up time. Detailed operational and measurement procedures for the laser system will be discussed in Section 3.4. During this warm-up period, the tanks in the tank farm outside of lab room 258 should be opened. For this research, the Hencken burner is needed to produce a hydrogen-air flame, so both the hydrogen and zero air tanks must be opened. The zero air used is a 77.6% N<sub>2</sub>, 20.5% O<sub>2</sub> mix with 2.9% trace gases, and contains 3.77 mols of nitrogen for every mol of oxygen. The burner also provides for a co-flow of nitrogen to be used in order to maintain a laminar flame far from the burner surface, so the nitrogen tank should be opened as well. When nitrogen is not available, other inert gases such as argon can be used for the same purpose. Koether's thesis describes the use of the co-flow in greater detail (Koether, 2007).

Once the tanks are open, the valves on the wall of the COAL lab must be opened as well. This charges the gas lines all the way to the flow controllers. Hankins notes this positive pressure on the flow controllers' inlets is of critical importance in order to prevent malfunction and damage (Hankins, 2008:59). With the warm-up time complete, the mass flow controllers can be set to the required flow percentages for the desired equivalence ratio and flow rate according to the procedures described in Koether's thesis (Koether, 2007). Lighting can then proceed according to the procedure outlined in Appendix B.

The Hencken burner used in the current research, shown in Figure 32 below, has inner burning surface dimensions of 24.5 x 24.5 mm, and outer dimensions of 38 x 38 mm.



**Figure 32.** The Hencken burner used for calibration of AFIT's COAL lab laser systems.

Research conducted by Hancock was referenced in order to pick Hencken burner operational parameters and find a good location for the laser sheet. The Hancock burner had inner dimensions of 36.5 x 36.5 mm, so the flow rates used in this research are scaled appropriately (Hancock et al., 1997:323-331). For laser calibration, the laser sheet is passed through the flame at a height of 15-25 mm above the burner's surface. This minimizes the effects of heat transfer to the surface while the high burner flow rate still provides plentiful OH for PLIF, in accordance with Hankins' suggestion (Hankins, 2008:123). Figure 33 shows this set-up in use.



**Figure 33.** Hencken burner and laser optics used for laser calibration in AFIT's COAL lab. The red arrows denote the path of the laser sheet.

The air flow rate is held constant at 40 SLPM and fuel (hydrogen) is varied to change equivalence ratio. Since the laser sheet is still near the burner's surface and the co-flow is a non-reacting gas, the co-flow rate is only important insofar as it is sufficient to maintain a laminar flame at the laser sheet's location.

Shut down procedures can be found in Appendix B. Another very important note is that the valves controlled by Lab-View should never be closed while the mass flow controllers are still on. This will cause the controllers to spike open and possibly jam in that position. Hankins' thesis details the procedure for safely bleeding the gas lines if it is necessary (Hankins, 2008:59).

### *Igniter Operation*

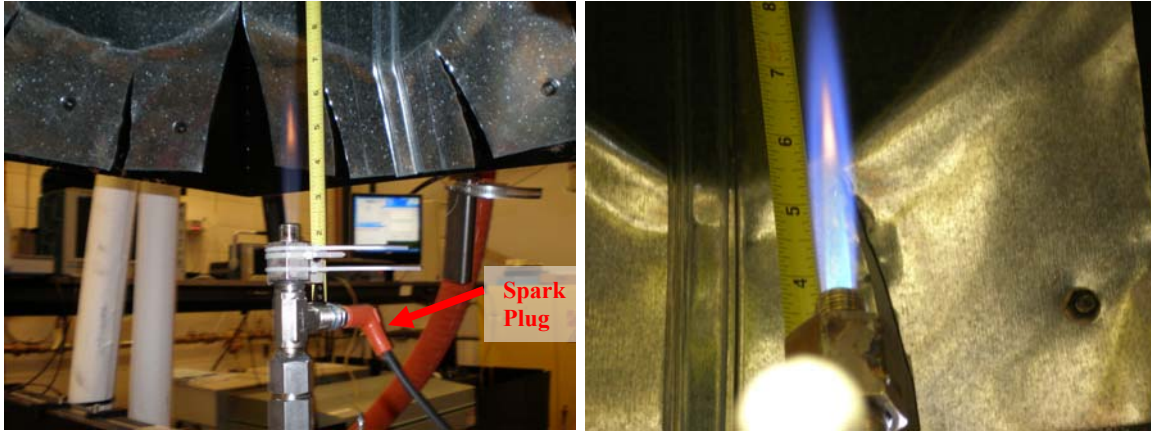
As discussed above, the dependable operation of the igniter is critical to repeatable and safe use of the UCC. It is necessary to discover a steady operating

condition producing a flame long enough to progress down the igniter tube shown in Figure 3 and still burn hot enough to ignite atomized or gaseous fuel.

Start-up procedures for the igniter are similar to those for the Hencken burner. The mass flow controllers must be warmed-up, and the appropriate tanks in the tank farm and associated valves on the lab wall should be opened. The UCC ignition system is an ethylene-air pre-mixed torch, and thus both the ethylene and zero air lines should be opened. Flow set points should be established according to Koether's procedure in order to achieve the desired equivalence ratio and flow rates (Koether, 2007).

With the set points established, the "Ethylene and Air" valve in the control VI can be opened, and the mass flow controllers turned on. Again, it is important not to have the flow controllers on with a downstream valve closed. Once the fuel (ethylene) and air are flowing, the "Igniter" toggle switch in the control VI should be turned on. Once a flame is established, the "Igniter" switch can be turned back off.

The characterization of the igniter requires two configurations. The first is an open-air flame directed straight into the exhaust system. This arrangement provides data on the flammability regime for the system, as well as allowing easy measurements of flame length. Because it is an open-air flame, a diffusion flame is expected to form an outer cone around a pre-mixed inner cone. The inner cone is the item of concern, as it will be the only reaction occurring in the igniter tube. Using the set-up shown in Figure 34, inner and outer cone lengths can be measured and recorded. A range of flow rates and equivalence ratios are needed to find the regime of best performance.



**Figure 34.** Two views of the open-air configuration used for igniter characterization.

The second configuration used in the characterization of the igniter employs it in the UCC section as it is designed for operational use. This configuration requires visual observation in the cavity to determine whether or not the flame will propagate and behave as expected. Observation will possibly necessitate the use of a mirror.

Shut down of the igniter again closely follows the Hencken burner procedure outlined in Appendix B, taking care not to close the “Ethylene and Air” valves before the flow controllers are switched off.

#### *UCC Section Operation*

Operation of the UCC section can require the full use of the COAL lab’s facilities. Depending on the configuration used, the equipment needed varies. As described previously, this study uses hydrogen as the primary fuel of interest. This was to validate the quartz window and PLIF techniques while still gathering data on the interior flow dynamics without dealing with soot on the windows. Appendix B has a detailed procedure for UCC operation using JP-8, but the current hydrogen study requires the modified method described below.

First, the mass flow controllers and laser must be warmed-up, and the proper gas tanks and valves opened, as described in the Hencken burner and igniter operations sections. For this experiment, hydrogen, ethylene, zero air, and nitrogen are all needed. Hydrogen is metered by a 50 SLPM flow controller, ethylene a 5 SLPM, and zero air a 30 SLPM controller. The nitrogen is used as a purge gas in this set-up, and does not need to be flow-controlled.

While the flow controllers and laser warm up, the air lines must also be given time to reach the desired temperature. Steps 1-8 in the “UCC Start-Up Procedure” section of Appendix B outline this process. Consistent with the Hankins study, the main line was heated to 480K and the secondary line to 420K (Hankins, 2008:70). Hearing and eye protection are essential during this type of testing. Velocities in the combustor are high enough to generate high noise levels and projecting any loose particles outward at high rates. The COAL lab’s capabilities have been enhanced in this respect by the addition of wireless radio headsets, allowing operators to communicate with each other while still providing sufficient hearing protection. Once the equipment warm-up is complete, Koether’s procedure for setting the necessary flow rates for the desired test condition on the MKS Type 247 should be followed.

In order to light the combustor, the igniter should be set to the conditions described in Section 4.2. The “Ethylene and Air” valves should be opened in Lab-View and then the mass flow controllers operating on the ethylene and air lines can be turned on, taking caution with the order of valve and controller operation as described previously. With ethylene and air flowing, the “Igniter” switch in Lab-View should be toggled on. Further igniter operation is described in Section 4.2.

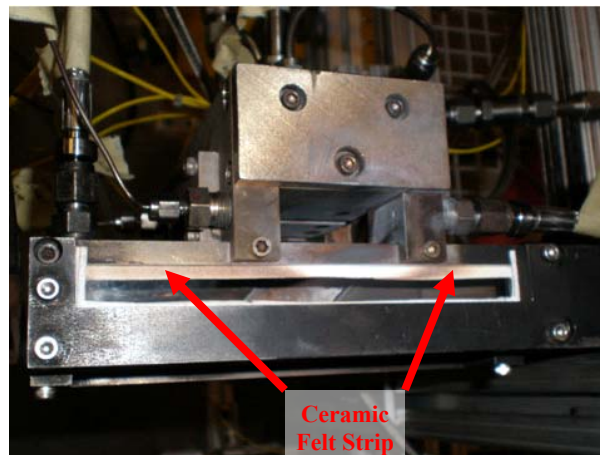
With the igniter operating and the combustor warmed-up according to Section 4.2, the UCC can now be lit. This is accomplished by opening the “Secondary Fuel Valve,” then turning the hydrogen channel of the Type 247 unit on and allowing the gas to flow. Once the UCC ignites, the igniter can be shut down by first turning the ethylene and air flows off, followed by toggling the “Igniter” switch off and closing the “Ethylene and Air” valves.

In order to facilitate the use of hydrogen and the first use of laser diagnostics in a UCC section, the combustor is modified from its state in the Hankins research. The fuel injectors described by Hankins are used to atomize liquid fuel (Hankins, 2008:12), but cause unnecessary pressure build-up and prevent the flow of gaseous fuel. The replacement of these injectors solves this problem. Two new nozzles, shown in Figure 35, consist of the barrel of a screw separated from its head and cut to the necessary length. This threaded rod is completely bored-through, allowing the free and unrestricted flow of gaseous fuel.



**Figure 35.** New fuel injectors developed for the use of gaseous fuels in AFIT's UCC sections.

Another modification to the combustor is the installation of the optically clear quartz windows. These windows, while capable of withstanding high temperatures, expand with heat and are very sensitive to compression. They tend to crack easily at any points of direct contact with steel. It is essential to maintain a good seal around the entire combustor except at the exits, and thus a new sealing method was devised. Thin strips of ceramic fiber are lightly glued to any steel surface which comes in contact with the quartz, and also at any joint known to leak. Figure 36 is a good example of the employment of the new sealant. This fiber has been found to withstand high temperatures and direct exposure to UCC flames without destruction and provides a good seal.



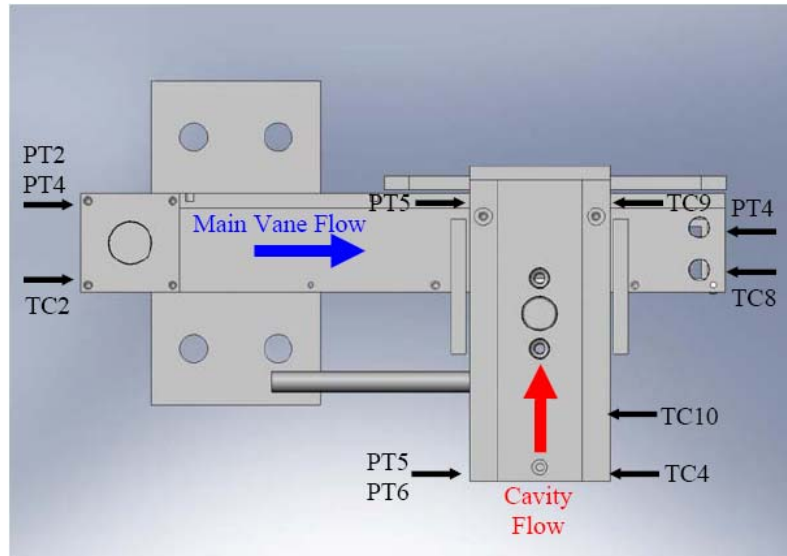
**Figure 36.** A view of AFIT's flat-cavity UCC section showing the use of ceramic fiber as a sealant.

The laser sheet is aligned through a window directly along the main vane with the direction of flow.

As addressed previously, the Lab-View VI handles all direct data acquisition from the UCC section. The program compiles pressure, temperature, and flow rate state data into a format easily manipulated in Excel. State measurement locations on the combustor



are shown in Figure 37. For all UCC tests, cavity air is held constant at 0.1 kg/min, with fuel rate changed to vary the cavity equivalence ratio and main flow rate changed to vary the overall equivalence ratio and cavity-to-main air flow ratio.



**Figure 37.** A view of AFIT's flat-cavity UCC section showing the location of state measurements on the combustor (Hankins, 2008:94).

The shutdown procedure for the UCC consists of turning off the hydrogen flow followed by closing the “Secondary Fuel Valve” in Lab-View. Steps 3-16 in Appendix B then apply for complete lab shutdown. With the hydrogen PLIF experiment completed, the igniter characterization experiment can be validated by conducting an ignition study in the UCC section using JP-8 as the fuel. Appendix B describes the operation of this configuration.

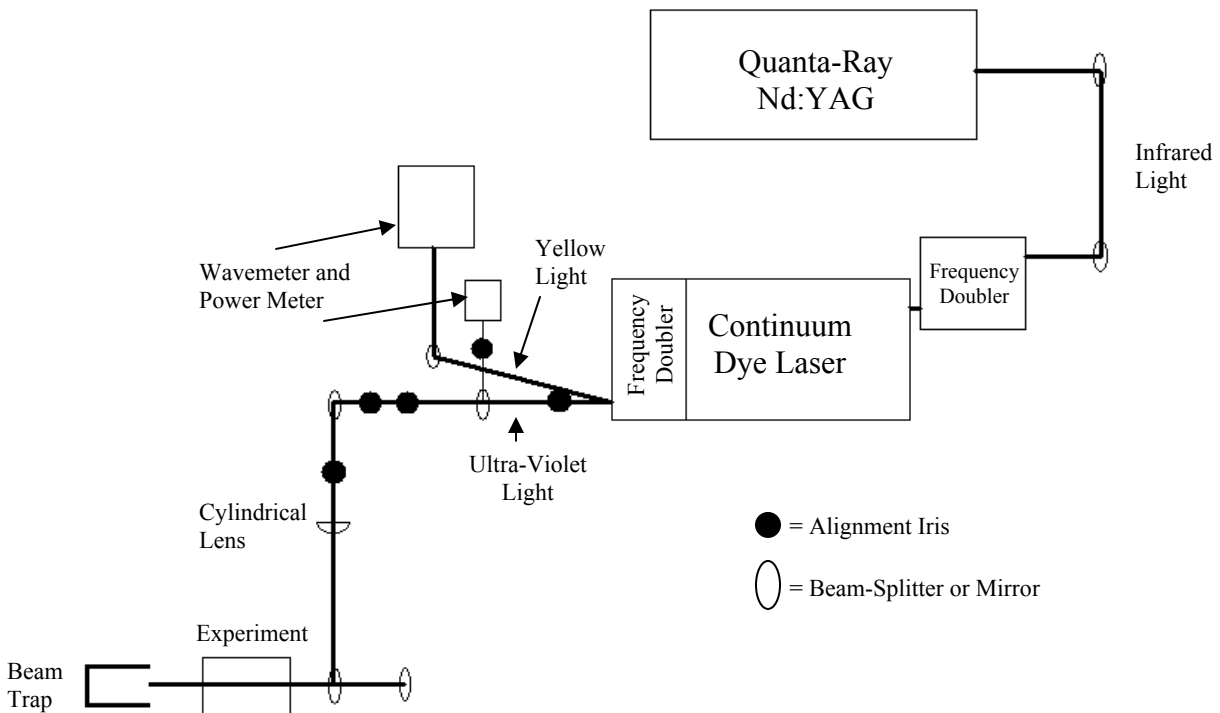
### 3.4 Laser Operations

The COAL lab’s laser system is state-of-the-art. The current set-up provides the capability to perform one-color PLIF and Coherent anti-Stokes Raman-Scattering (CARS) spectroscopy, and forthcoming additions will provide two-color PLIF, particle

imaging velocimetry (PIV), and laser-induced incandescence (LII), among others. Only the PLIF capability is used in this study.

### *Set-Up and Operation*

The PLIF laser system is arranged on one of two optics tables in the COAL lab. The laser is created by a Quanta-Ray PIV-Series dual pulsed Nd:YAG unit made by Spectra-Physics, and tuned in a Continuum ND6000 narrow-band combination dye laser and frequency doubler. The system was assembled by Innovative Scientific Solutions, Inc. (ISSI). The YAG produces a pulsed 1064 nm beam at 200-400 mJ, and pulse separation times range from 100 ns to 100 ms (Hankins, 2008:4, 26). The beam passes through several sets of optics, allowing power output and wavelength to be measured without interrupting the beam path, as shown in Figure 38.



**Figure 38.** Diagram of the COAL lab's PLIF laser system and beam path.

In the diagram, the power and wavelength measurement techniques are shown. As explained in Section 2.7, frequency doubling produces both the incident frequency and a second, exactly doubled frequency. This is useful because it allows measurement of the undesired beam's wavelength, which can simply be divided by two in order to determine the wavelength of the beam of interest. The wavemeter is an Angstrom High Finesse WS-7 unit. In order to measure power, a 5% beam-splitter is arranged in the path of the ultra-violet beam, deflecting some of the light into a power meter.

Also depicted in the figure are several alignment irises. These are placed directly in the beam path and are opened or closed by hand. As the wavelength of the beam is altered for each experiment, its diffraction angle through the final frequency doubler

changes, requiring a re-alignment of the beam. At each wavelength change, the irises are partially closed, and the doubling crystal is tuned until the beam passes directly through all of them. A -300 mm cylindrical lens coupled with a 1 m focusing lens is used to shape the circular beam output by the dye laser into the flat sheet of light needed at the experiment.

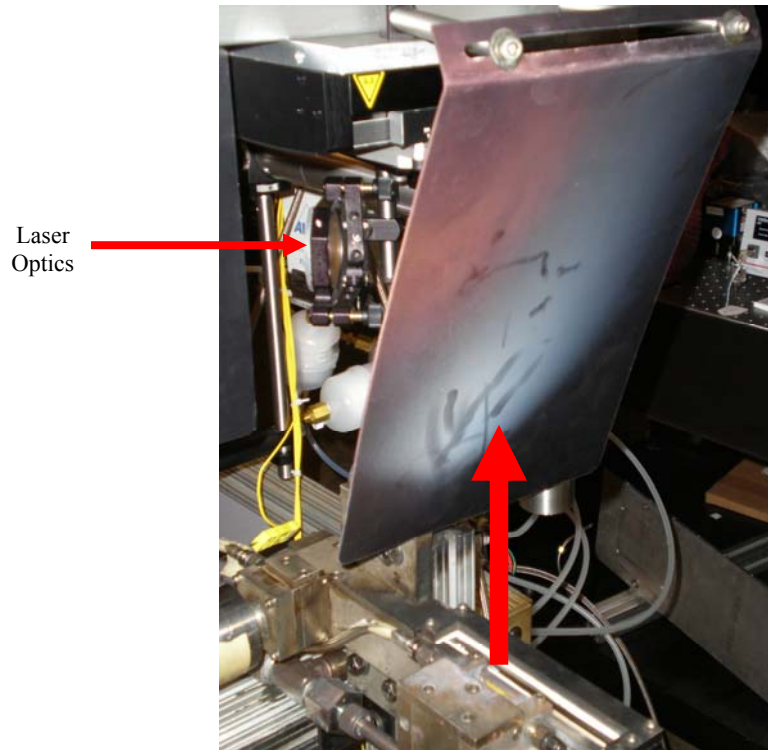
Operation of the laser is accomplished at a second computer station, shown in Figure 39. Operating instructions and maintenance procedures are loaded onto the computer in a text file. These instructions can be referenced in Koether's thesis (Koether, 2007).



**Figure 39.** The laser operating station in AFIT's COAL lab (Hankins, 2008:43).

In order to protect the sensitive optics used to guide the beam through the experiment, a heat shield is attached between the experimental area and the mirror just above it. This arrangement is shown in Figure 40. The heat shield diverts any hot

exhaust slightly away from the mirrors, but not enough to keep it out of the exhaust hood's capture area.



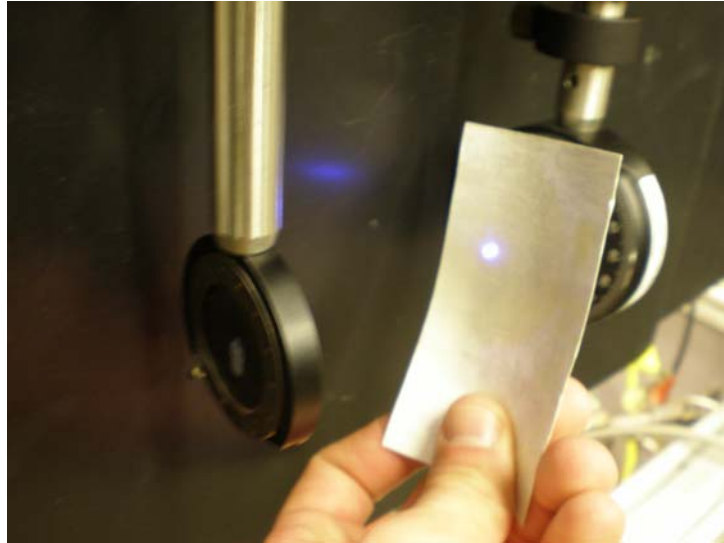
**Figure 40.** This image shows the placement of the heat shield between any hot exhaust and the laser optics. The red arrow represents the UCC's exhaust flow.

### *Calibration*

As a whole, the PLIF system used in this research comprises three main parts: the laser, the image acquisition equipment, and the combustion apparatus. Because of the laminar flame it produces and the ability of the user to determine exactly the conditions for the flame, a Hencken burner is used to calibrate the system. The procedures for this calibration are described below.

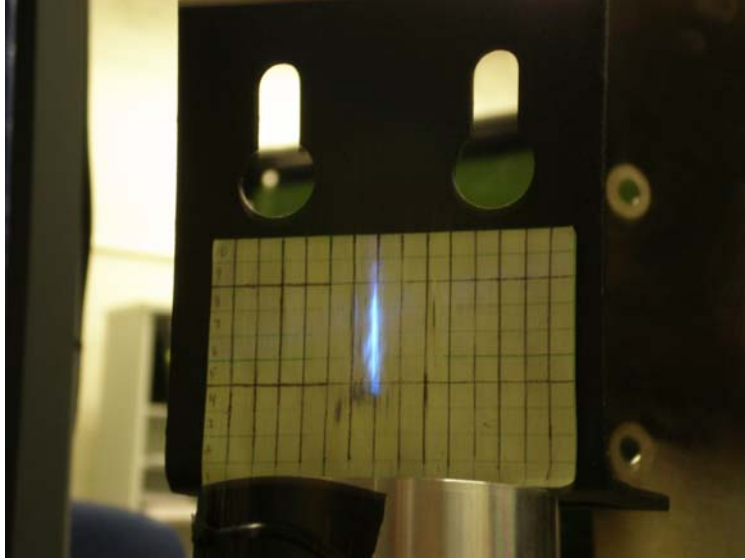
Once all of the equipment is in place and connected, the first task is to tune the laser. Several factors affect the output of the laser, including dye concentration and doubling crystal alignment. Using the power and wavemeters, these factors can be

tweaked until maximum performance is achieved. With the laser tuned, the beam must then be aligned through all of the optics and over the surface of the Hencken burner. This is accomplished using alignment irises, as described above. Figure 41 shows what a correctly aligned beam looks like.



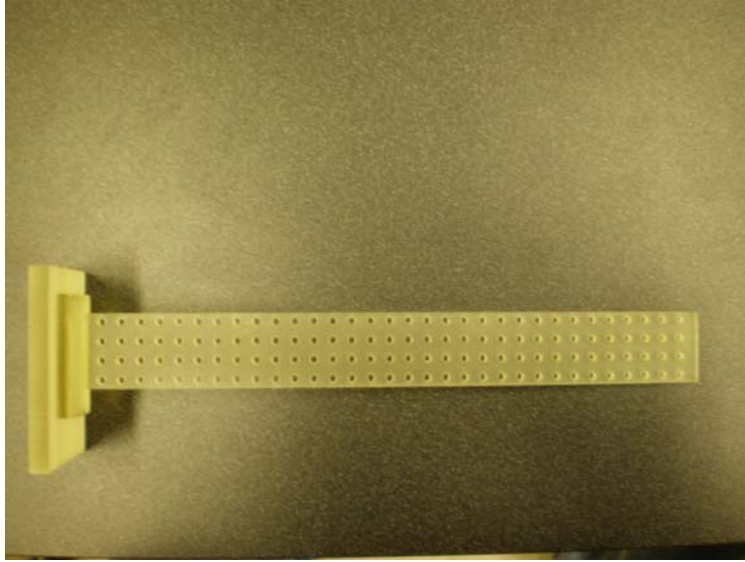
**Figure 41.** This image shows the beam-alignment process using adjustable irises.

With the beam aligned through the irises, the final turning optics must be adjusted in order to ensure the laser sheet is exactly vertical, crosses directly over the center of the burning surface, and has no skew angle in any plane. Two alignment aids will be used for this purpose: one for the Hencken burner and one for the UCC section. Figure 42 shows the graph paper and metal plate aid for the Hencken burner.



**Figure 42.** The graph paper and metal plate alignment aid used for Hencken burner tests.

The graph paper ensures that the beam is vertical, and any skew angle can be checked by moving the plate forward and back across the surface of the burner. The paper also allows the height of the laser sheet to be measured. For the UCC section, a special plastic calibration sleeve was designed and cut. This sleeve, shown in Figure 43 fits snugly into the exhaust end of the main vane and has a 5 x 5 mm grid of holes cut into it. The sleeve provided the ability to align the laser sheet within the combustor, and aided in camera-focusing, as well.



**Figure 43.** The plastic sleeve designed for beam alignment in the UCC section.

During the alignment process, it is also possible to adjust the focal point of the beam. The laser should be focused directly over the Hencken burner's surface. This can be verified using a white business card. The output power of the laser system is high enough that an audible snapping noise is heard with the card in the beam path. This noise is loudest at the focal point. The cylindrical lens and associated focusing lens can be moved until this is the case.

Once the beam is aligned and focused, the ICCD camera must be focused, as well. This is accomplished using the same beam alignment aids. By removing all filters in front of the camera, more light enters the camera and an image of the combustion system and alignment aid is visible. The camera should be focused exactly on the alignment aid since that is where the laser sheet will pass through the flame.

The image collection system must now be timed very accurately in order to ensure images are taken when the OH is fluorescing. By installing an oscilloscope to the laser and camera triggers, users can roughly adjust the camera trigger to fire shortly after



the beam is released. Precise timing requires actual image collection. The gate delay and gate width settings must be tuned carefully in order to ensure all of the LIF signal is captured while eliminating any other signal sources. The initial settings are adjusted first by capturing LIF on a business card, but should be done using actual OH in a flame as the final check.

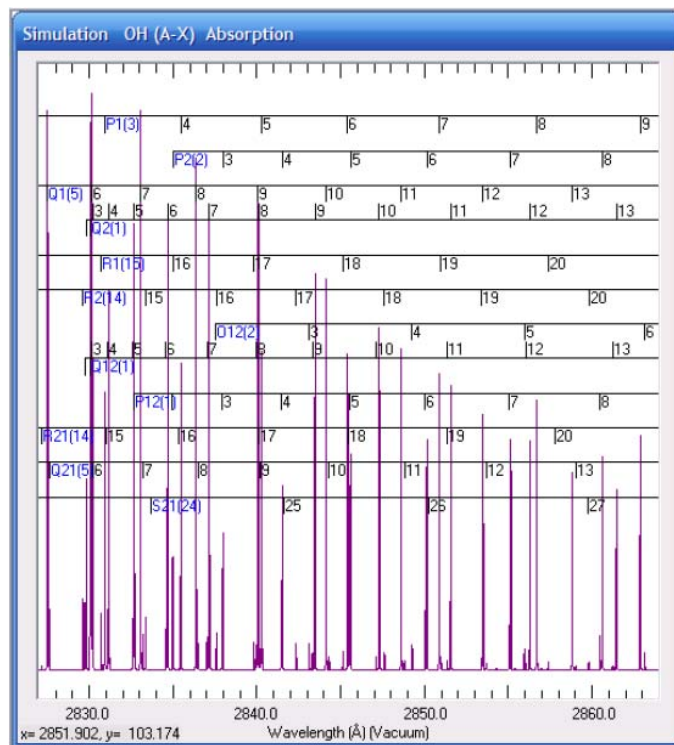
With the camera timed correctly, two final checks must be performed. The first is to verify the camera is not being saturated by LIF signal. This check is accomplished by lowering the laser power and operating the camera in its “focus” setting. The focus setting streams continuous images, as if it were a video feed. The signal intensity should be measured and recorded, and the laser power slowly increased after each data point, all the way to maximum power. When reduced, the data should show a linear increase in signal intensity with increased power. If not, the camera was most likely saturated. Next, the region of interest should be checked for scattering. Scattering is due to laser light reflecting off particles or from fluorescing particles in the air. A scatter check simply requires any flame to be off and the laser to be on. If any signal is present, the filter configuration or gate width setting should be examined.

Finally, data must be collected on the Hencken burner at all conditions of interest for the UCC study. Using the Hencken results, data from the later experiment can be correlated to the numbers gathered at precisely known conditions, providing an accurate measurement system for data reduction.

### *LIFBASE*

LIFBASE is a free system used for the simulation of electronic transition behavior for diatomic molecules (Hankins, 2008:57-58). It has the capability to simulate both

absorption and emission (Hankins, 2008:57-58), including the calculation of the collisional and Doppler broadening correction factors. For this study, LIFBASE was used to calculate and compare theoretical data and as a line-finding tool. Figure 44 shows a screenshot of the program as it was used for the OH (A-X) (1-0) electronic transition system. Horizontal lines represent the various rotational states of the (1-0) vibrational level, with each rotational variation designated by a small numbered vertical line. Wavelengths are given in Angstroms ( $\text{\AA}$ ).



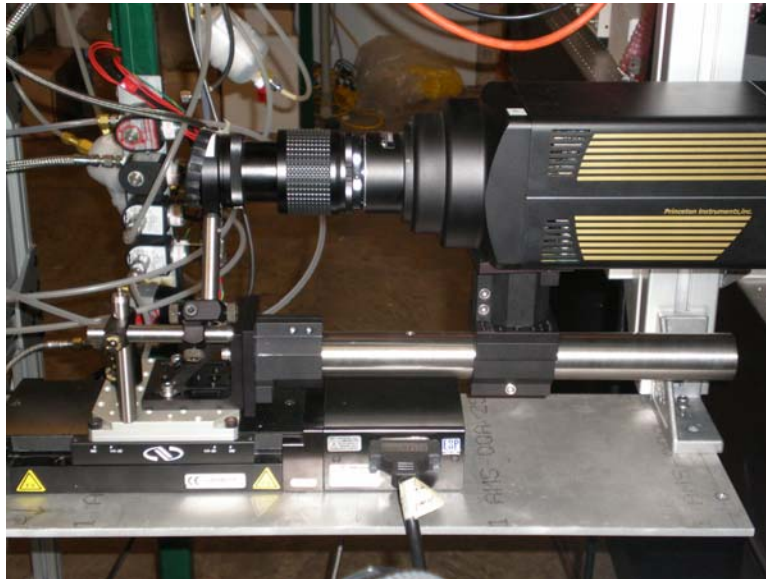
**Figure 44.** A screenshot of the LIFBASE program used for calculations in the OH (A-X) (1-0) vibrational level. Wavelengths are given in Angstroms (Hankins, 2008:57).

The purple lines represent wavelengths at which OH absorbs incident light. Their height indicates the relative OH absorption at that wavelength, and thus their relative signal strength. They are normalized by signal strength, with the tallest line normalized to 100 (Hankins, 2008:57-58). LIFBASE calculates these spectral simulations at a range

of temperatures, showing the varying OH populations and thus varying signal strengths at each temperature (Hankins, 2008:57-58). This theoretical data is important for correlation with experimental data in order to determine measurement accuracy.

### *PLIF Image Collection*

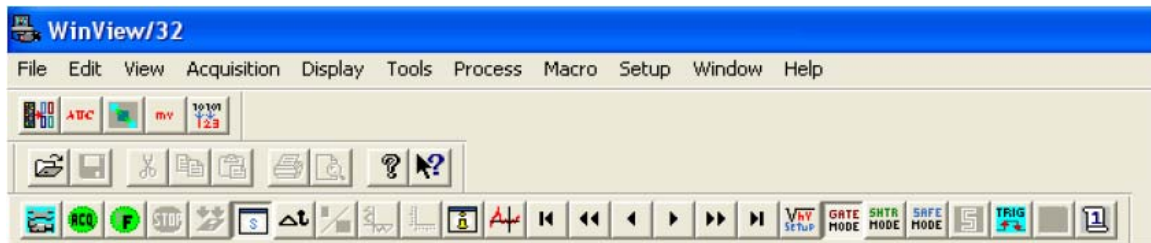
Collection of PLIF images is accomplished using an intensifying charge-coupled device (ICCD) camera made by Princeton Instruments (PI-Max, 512 x 512 pixels) and shown in Figure 45 (Hankins, 2008:5). The camera is fitted with a Nikon UV lens. Several configurations of Schott CG-WG-295 colored glass filters ensure only light due to OH fluorescence is captured.



**Figure 45.** The Princeton Instruments ICCD camera used for image collection in AFIT's COAL lab.

The camera is controlled at a third computer station using Win-View 32 software, shown in Figure 46. Instructions for the camera's operation can be found in Koether's thesis

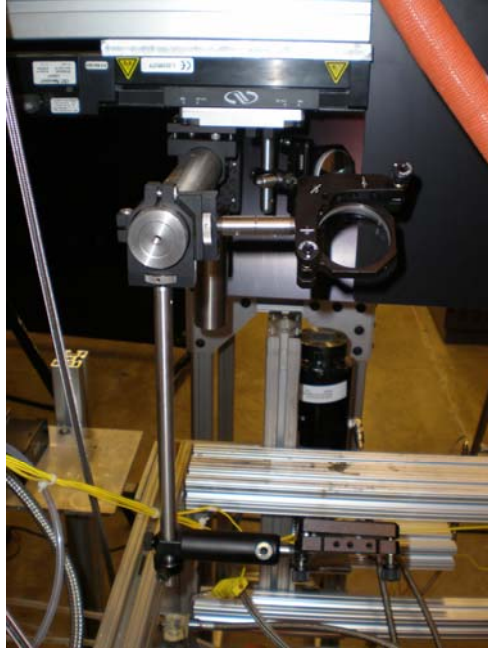
(Koether, 2007), and the use of Win-View is covered in Appendix C of Hankins' thesis (Hankins, 2008:136-138).



**Figure 46.** Screenshot of the Win-View 32 software used for image analysis (Hankins, 2008:45).

The Win-View software and camera are capable of allowing multiple accumulations per image, and multiple images can be used and averaged in order to get the best signal quality. The software is also capable of performing image signal processing, and is used for signal intensity measurements. During calibration, gate timing must be set in the software with an aperture setting, or “f stop,” for the camera selected (Hankins, 2008:61).

The camera and laser optics are mounted on computer-controlled translation tracks, shown in Figure 47. These are used to ensure that the laser sheet can be moved through the flame without affecting the beam alignment or focus of the camera.



**Figure 47.** Laser optics mounted on one of two Universal motion control tracks in AFIT's COAL lab.

The tracks are controlled and powered by a Newport Universal Motion Controller/Driver, model ESP300. This unit has the capability to control up to three axes of motion, two of which are used in the current experiment. Commands can be given to the controller directly or through ESP Utility Version 4.2 software on the camera control station's computer (Hankins, 2008:46-47). This software allows single millimeter translations of attached tracks. Instructions for the use of the motion control system can be found in Appendix D of Hankins' thesis (Hankins, 2008:139).

### *Quenching Correction*

As discussed in Section 2.7, a correction for quenching is needed when processing PLIF images. The correction used was published by Tamura et al., and is described below.

First, species concentration, temperature, and pressure data must be calculated for an equilibrium condition using equilibrium combustion software, as described in Appendix C. Several tabulated constants are needed, as well. These are listed in Tables 5 and 6, which show accepted constants and empirically determined values published by Tamura, respectively (Hankins, 2008:63).

**Table 5.** Constant values needed for quenching correction factor calculations (Hankins, 2008:63).

Constant	Value
OH Spontaneous Emmissions Constant (A)	$1.45 \times 10^6 \text{ s}^{-1}$
Boltzman's Constant (k)	$1.38065 \times 10^{-23} \frac{\text{m}^2 \text{kg}}{\text{s}^2 \text{K}}$

**Table 6.** Empirical values for quenching correction factor calculations (Tamura et al., 1998:502-514).

Colliding Species	$\sigma_{Q(INF)}$ (Angstroms) <sup>2</sup>	$\epsilon/\kappa$ (K)	Quenching Rate Coefficient
CH <sub>4</sub>	11.0	320	$(5.07 \times 10^{-19})(\sigma_Q)(T^{0.5})$
H	14.5	84	$(15.0 \times 10^{-19})(\sigma_Q)(T^{0.5})$
O	0.0	0	$(0 \times 10^{-19})(\sigma_Q)(T^{0.5})$
N	0.0	0	$(0 \times 10^{-19})(\sigma_Q)(T^{0.5})$
H <sub>2</sub>	4.5	224	$(10.88 \times 10^{-19})(\sigma_Q)(T^{0.5})$
OH	20.0	384	$(4.99 \times 10^{-19})(\sigma_Q)(T^{0.5})$
CO	12.0	397	$(4.97 \times 10^{-19})(\sigma_Q)(T^{0.5})$
NO	0.0	0	$(0 \times 10^{-19})(\sigma_Q)(T^{0.5})$
O <sub>2</sub>	8.0	243	$(4.37 \times 10^{-19})(\sigma_Q)(T^{0.5})$
H <sub>2</sub> O	20.0	434	$(4.92 \times 10^{-19})(\sigma_Q)(T^{0.5})$
CO <sub>2</sub>	11.0	488	$(4.16 \times 10^{-19})(\sigma_Q)(T^{0.5})$
N <sub>2</sub>	0.4	624	$(4.47 \times 10^{-19})(\sigma_Q)(T^{0.5})$

Correction for quenching is accomplished by calculating LIF Efficiency through the following multi-step process. Equation 21 below is used to determine the temperature dependence of each molecule's cross-section:

$$\sigma_Q = \sigma_{Q_{INF}} e^{\left(\frac{\varepsilon}{kT}\right)} \quad (21)$$

The number density for each species must also be known, and is found using Equation 22:

$$\text{Species Number Density} = \left(\text{mole fraction of the species}\right) \left(\frac{P}{kT}\right) \quad (22)$$

Using this quantity and Table 6, the quenching rate for each species is calculated according to Equation 23:

$$Q_{\text{species}} = (\text{Species Number Density})(\text{Quenching Rate Coefficient}) \quad (23)$$

Total quenching rate is the sum of each of the species' rates:

$$Q_{\text{Total}} = \sum Q_{\text{species}} \quad (24)$$

Finally, LIF Efficiency is calculated using Equation 25 following manner:

$$\text{LIF Efficiency} = \frac{A}{A + Q_{\text{Total}}} \quad (25)$$

By dividing the measured intensity by the LIF Efficiency calculated, the corrected intensity can be found.

### 3.5 High-Speed Camera Operations

High-speed footage and images are used in this research to investigate the regime in which the dual-vortex condition exists. The camera used is an Integrated Design Tools (IDT), Inc. X-Stream XS-4, shown in Figure 48 with an 85 mm Nikon Micro Nikkor

lens. It is controlled by ITD Motion Studio software operating on a portable computer station.



**Figure 48.** Integrated Design Tools, Inc. X-Stream XS-4 high-speed camera used for image collection in AFIT's COAL lab.

In order to acquire images or video, users must open the program from the computer's desktop, and then open a camera session. The camera is attached to the station by a USB cable, and appears as "MotionPro X on USB 2.0" in the menu of available cameras once it is turned on. With the camera open, users need only press play or record to gather footage. The frame rate was set to 200 Hz and single exposure per image for this research.



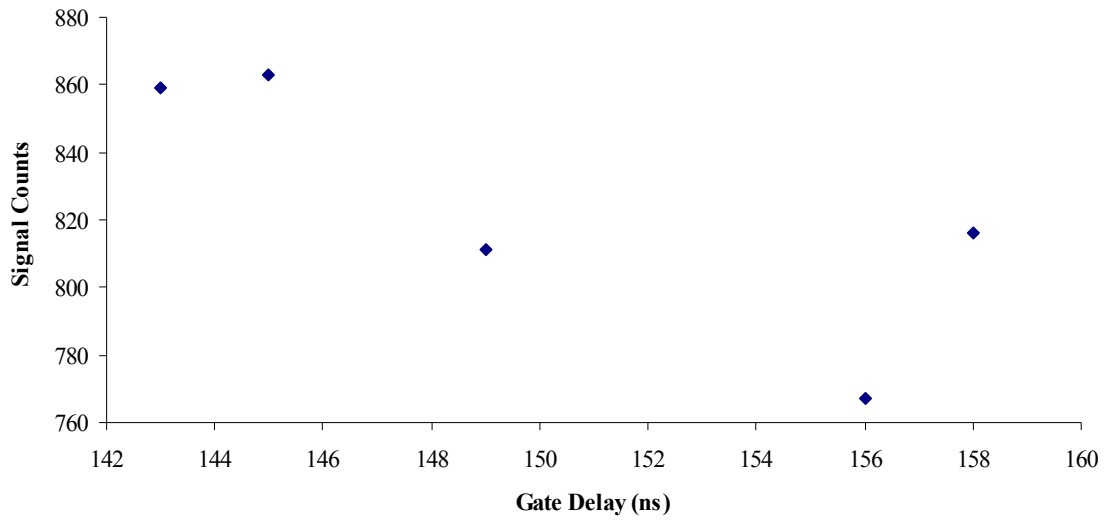
## IV. Results and Discussion

### 4.1 *Hencken Burner OH PLIF Results*

As previously described, the COAL lab's Hencken burner was used to calibrate the PLIF system and create an empirical thermometer that could be used to determine flame temperature inside the UCC section. Both the intensity ratio and excitation scan methods were used and are presented below.

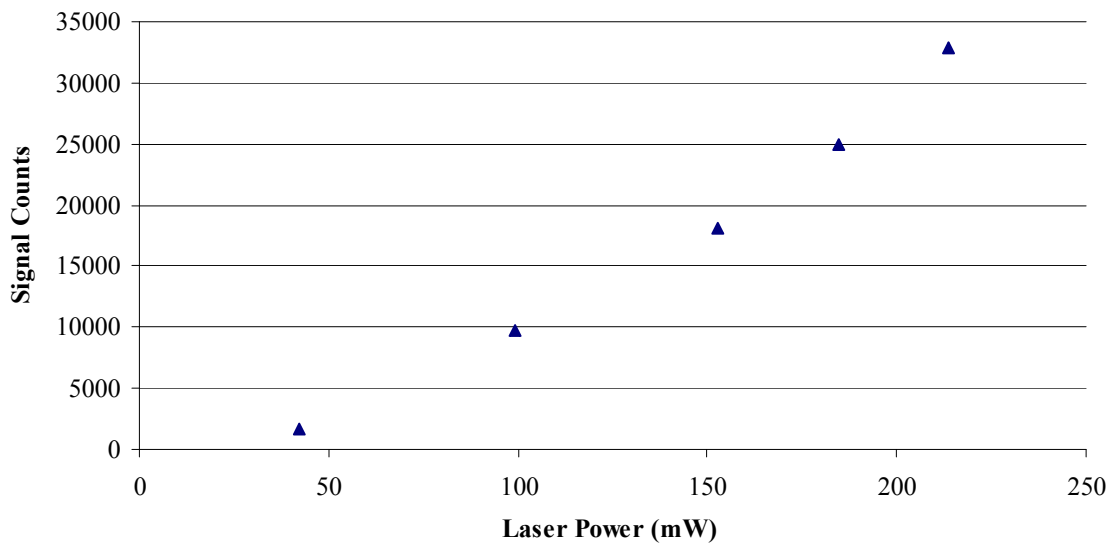
#### *General Calibration Work*

The first step for either process was to ensure the system was aligned, timed, and tuned correctly. From Hankins' research, the 3.8 aperture setting or "f stop" on the camera was selected, as it provided sufficient contrast between the LIF signal and background while still letting in as much light as possible (Hankins, 2008:62). Also for this study, a Schott CG-WG-295 filter was used in front of the camera. During the camera-timing process, a gate width of 40 ns on a 145 ns delay proved to produce the best images, as shown in Figure 49.



**Figure 49.** Results of the timing process for the COAL lab's Princeton Instruments ICCD camera. A hydrogen-air flame created by a Hencken burner at  $\phi = 1$  was used to produce OH.

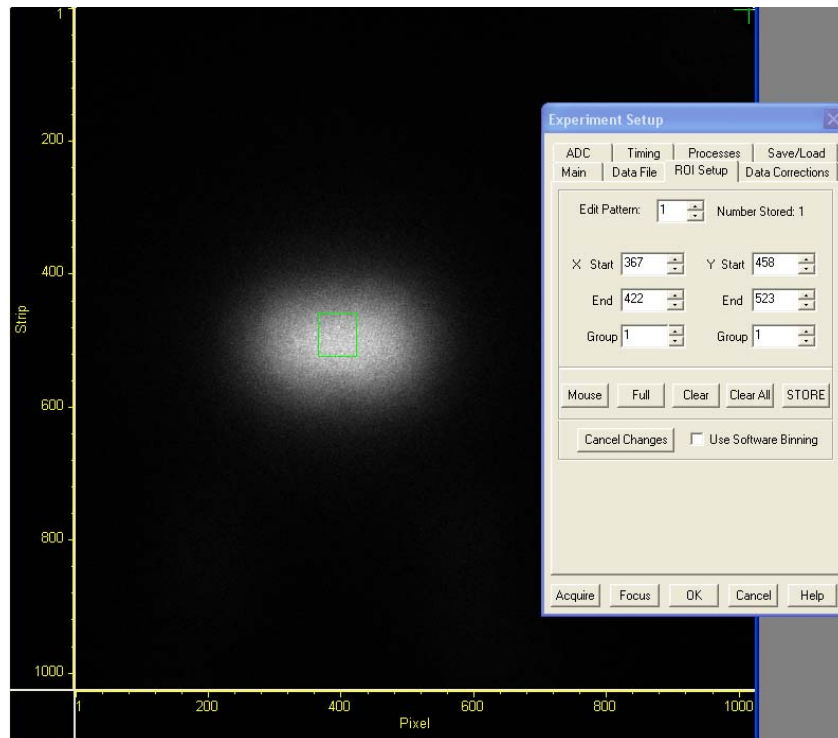
With these settings chosen, the next step was to perform a saturation check. Figure 50 shows the results.



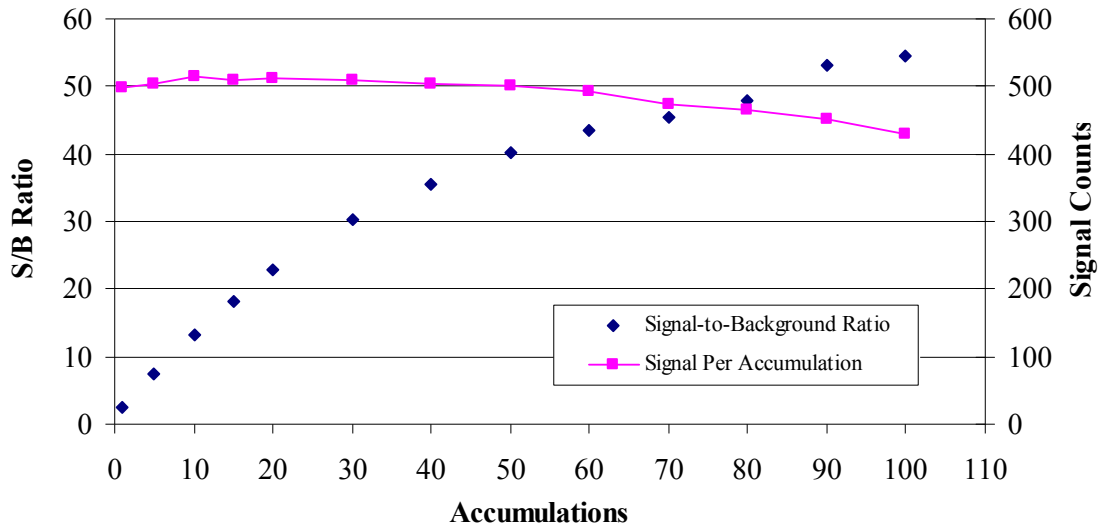
**Figure 50.** Results of the saturation check on the hydrogen-air Hencken burner flame in AFIT's COAL lab.

The plot shows between 150 and 215 mW, where all measurements were taken, the LIF signal did increase at a constant rate with respect to power, and the camera was not saturated. Regular scatter checks during testing also showed no interfering signal.

After examining the image picked up by the camera at several laser lines it was determined that allowing multiple exposures to accumulate for each image might provide a stronger signal and better contrast. For this to be an accurate method, however, the linearity of the measured signal with number of accumulations needed to be verified. This was accomplished by subtracting background intensity from signal intensity in a designated ROI, shown in Figure 51, and dividing that quantity by the number of accumulations. The results are reported in Figure 52.



**Figure 51.** Screenshot of Win-View 32 showing the ROI used for the PLIF system calibration on the Hencken burner.



**Figure 52.** Results of the signal per accumulation check.

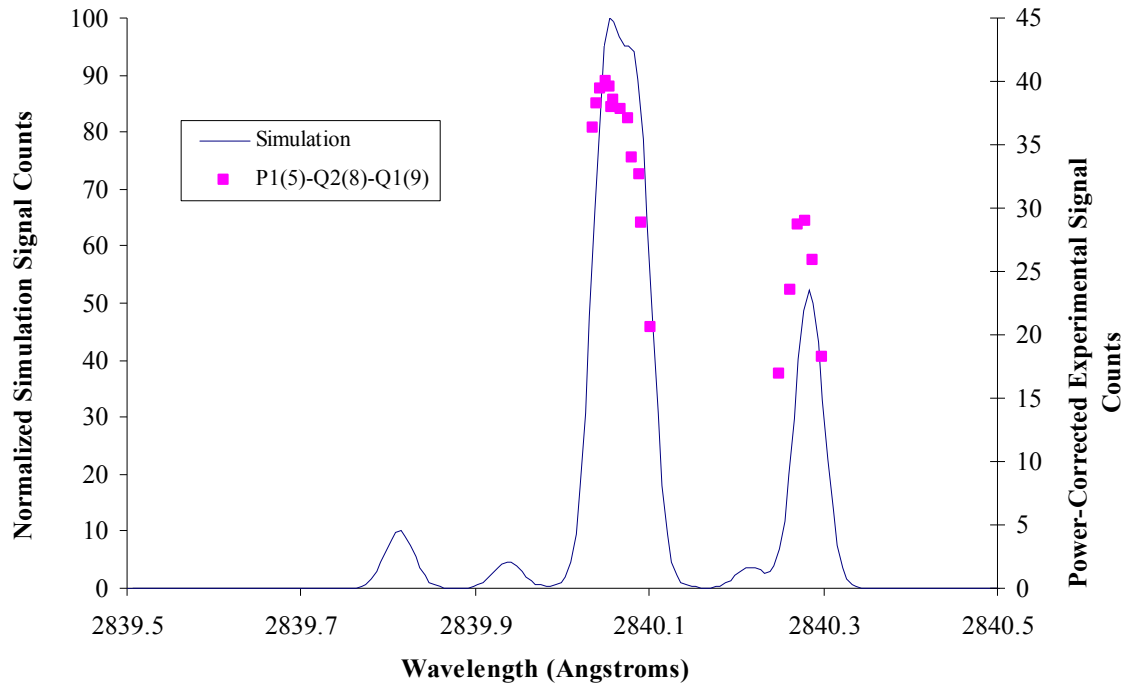
The investigation shows below 50 accumulations for each image, the signal per accumulation shows a roughly linear trend. This means that the results of studies using up to 50 accumulations per image are valid.

With the camera tuned and ready, it was necessary to conduct a scan for the line peaks which looked usable for PLIF in LIFBASE. Lines of interest and their wavelengths are shown in Table 7. LIFBASE includes both the Doppler and collisional broadening corrections, so these effects have been accounted for in all theoretical data. Research conducted by Rea et al. was used to determine the collisional broadening coefficients needed (Rea et al., 1986:125).

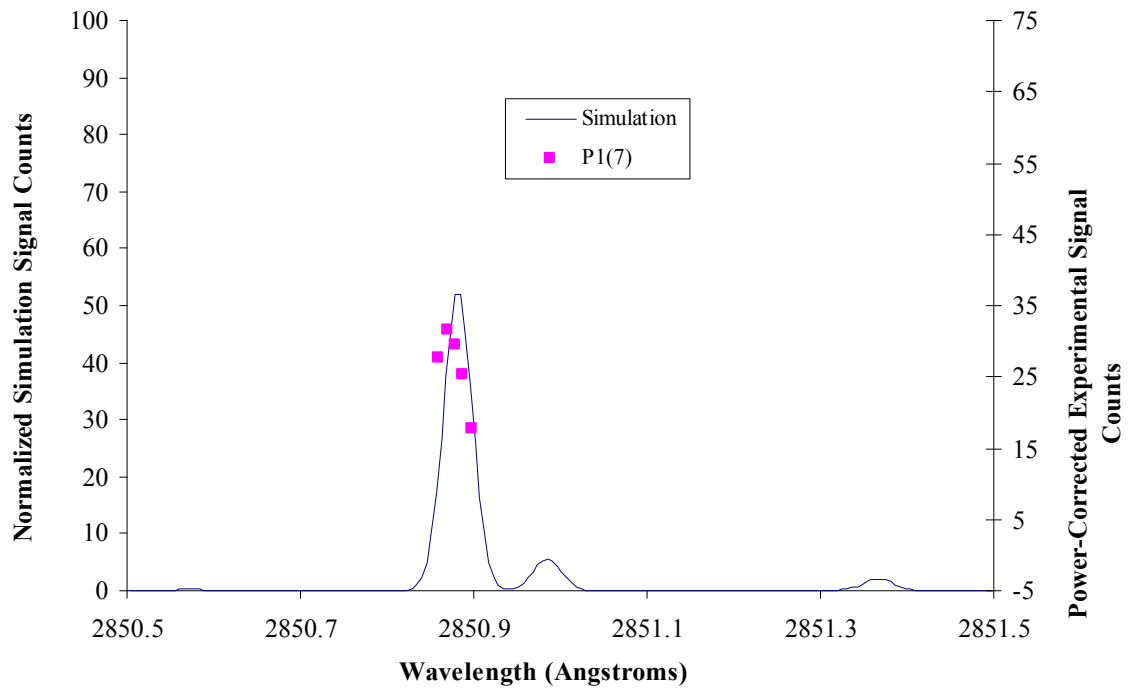
**Table 7.** Rotational variations and wavelengths of the OH (A-X) (1-0) vibrational level investigated for use in PLIF thermometry.

Rotational Variation	LIFBASE Wavelength (nm)	Experimental Wavelength (nm)
P <sub>1</sub> (7)	285.089	285.087
Q <sub>2</sub> (11)	285.157	285.156
R <sub>2</sub> (8)	281.725	281.724
R <sub>2</sub> (5)	281.738	281.737
Q <sub>1</sub> (14)	286.456	286.455
Q <sub>1</sub> (5)	282.750	282.750
R <sub>2</sub> (13)	282.639	282.637
P <sub>1</sub> (2)	282.663	282.663
Q <sub>1</sub> (9)	284.005	284.005
Q <sub>2</sub> (8)	284.008	284.007
P <sub>1</sub> (5)	284.029	284.028

Figures 53 and 54 are examples of the results of the peak search. The search tests were all conducted at  $\phi = 1$ , so the only correction needed for the measured fluorescent intensity was to account for laser power. These power-corrected values are shown in Figures 53 and 54. The study indicated that eight of the actual lines peaked just slightly under the LIFBASE wavelength, which may be due to measurement error or Doppler shift resulting from the flow velocity. The flame was on the edge of the exhaust system's capture area, and may have not been perfectly parallel to the plane of the camera lens. The Doppler correction in LIFBASE accounts for broadening, but since flow velocity cannot be input, the theory cannot account for those effects.



**Figure 53.** Experimental results for the initial peak search at the P<sub>1</sub>(5), Q<sub>2</sub>(8), and Q<sub>1</sub>(9) rotational variation lines.

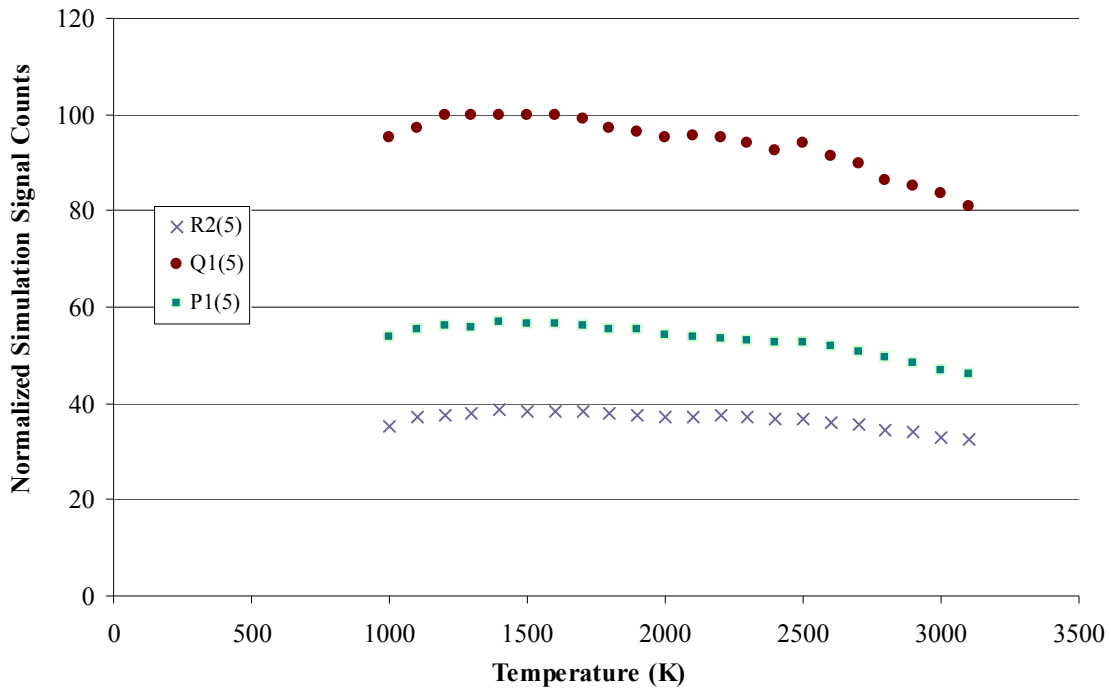


**Figure 54.** Experimental results for the initial peak search at the P<sub>1</sub>(7) rotational variation line.

These experimental peak locations were used for all further PLIF measurements.

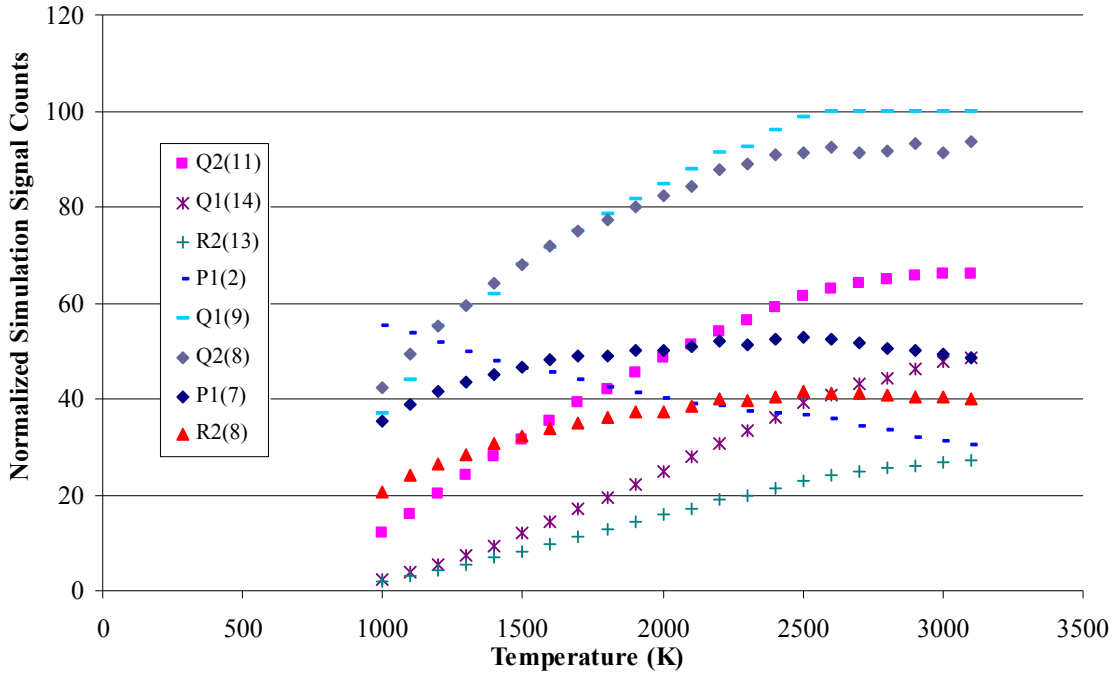
### *Intensity Ratio Method*

Once the peak locations were verified, testing for the intensity ratio method began. The first task was to find and evaluate possible temperature-insensitive lines. LIFBASE was used to locate candidates which were subsequently experimentally evaluated. Before testing, however, theoretical values from LIFBASE for all eleven lines were tabulated and reduced in order to create a theory-based thermometer to compare with experimental data. Of the eleven lines used in the peak search, three were designated as temperature-insensitive, and Figure 55 shows their predicted signal strength with temperature.



**Figure 55.** LIFBASE theoretical predictions for three candidates for the temperature-insensitive line used in PLIF thermometry.

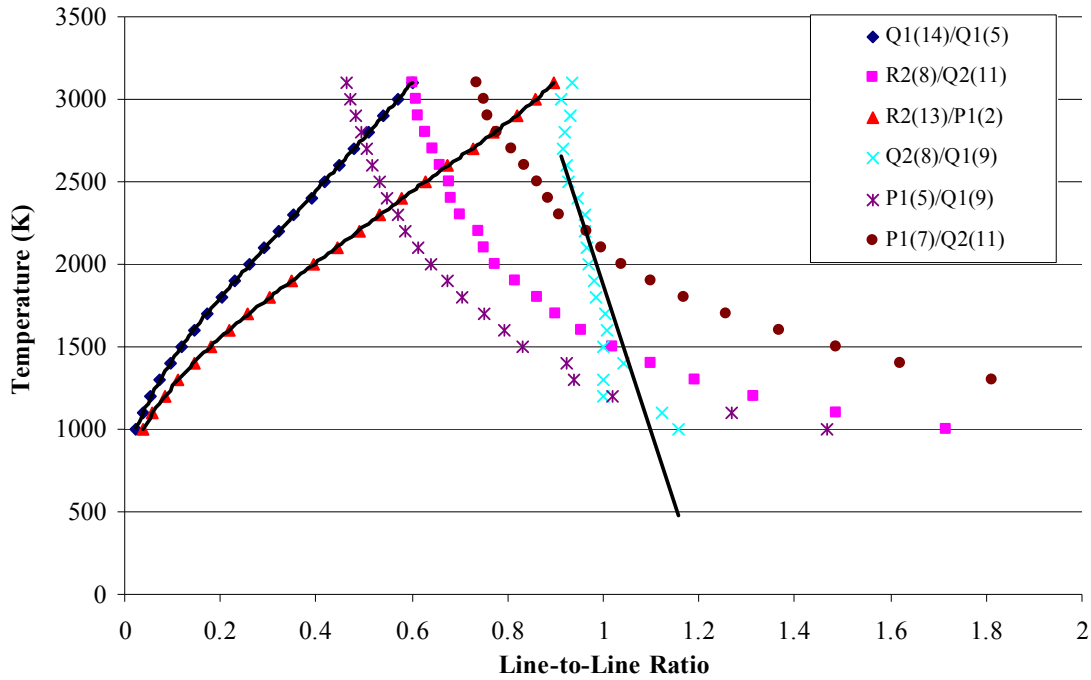
Figure 56 shows the same data for the other eight temperature-sensitive lines.



**Figure 56.** LIFBASE theoretical predictions for the eight temperature-sensitive lines used in PLIF thermometry.

From the Hankins research referenced for this study, several possible line pairs for calculating intensity ratios were selected. Using the theoretical predictions above, trends for temperature as a function of intensity ratio were developed for each pair and are shown in Figure 57. Trend lines have been added for several data series in order to highlight the quality of interest, slope, in this plot.





**Figure 57.** Theoretical temperature trends with intensity ratio based on LIFBASE calculations. The black lines are trend lines.

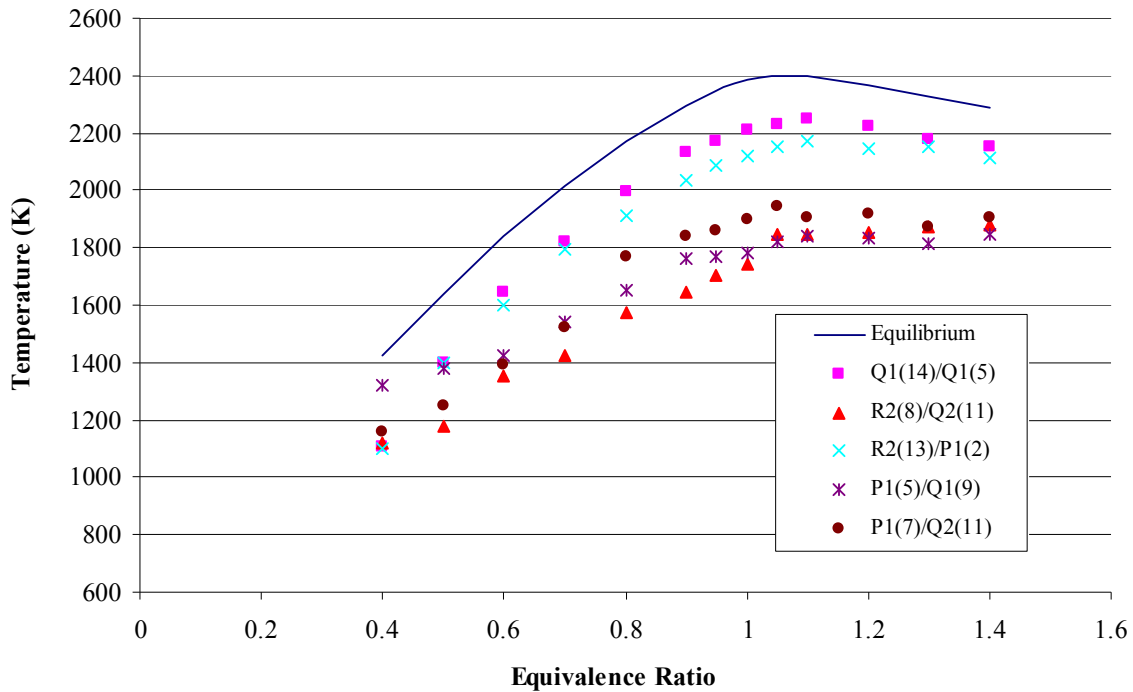
The plot reveals several important things. The first is that one of the pairs,  $Q_2(8)/Q_1(9)$ , has too steep of a slope to be of any use. Even very small fluctuations in line ratio indicate large jumps in temperature for this pair. The second is that in the operating temperature range for the flames in this study, roughly 2000-3000 K, two line-pairs show a positive linear trend. This makes them useful and consistent when determining temperature. The trend lines for these two pairs were calculated as fifth order polynomials, the equations for which effectively serve as thermometers for future PLIF data. Equation 26 gives the trend for  $Q_1(14)/Q_1(5)$ , and Equation 27 is for  $R_2(13)/P_1(2)$ .

$$T = (62819)R^5 - (116871)R^4 + (84375)R^3 - (29553)R^2 + (8258.5)R + 821.03 \quad (26)$$

$$T = (11984)R^5 - (30704)R^4 + (30482)R^3 - (14794)R^2 + (5701.5)R + 809.56 \quad (27)$$

$T$  is temperature in degrees Kelvin and  $R$  is the intensity ratio in these equations.

Experimental measurements of flame temperature could now be performed. With the five useful line pairs shown above, fluorescent intensity measurements were taken at a range of equivalence ratios for each set. Intensity data was gathered in a common ROI for every image and processed to return intensity ratios. Using the thermometry equations described above, experimental temperature readings were calculated for each pair at each equivalence ratio, and are reported in Figure 58.



**Figure 58.** Temperature readings generated using the intensity ratio method of PLIF thermometry. Theoretical data was calculated by STANJAN.

Again, accounting for power was the only correction needed because for ratio comparisons, any other correction factors cancel out. With this correction, the plot shows experimental values closely following the theoretical trend generated by the equilibrium kinetics software STANJAN. Unlike the Hankins study, the experimental measurements peaked with the theoretical data. Hankins predicted that the peak discrepancy noted in

that study was due to the lower flow rates and resulting heat losses, which appears to be the case. The two pairs previously noted for their linearity in the right temperature range return temperature readings much closer to what theory predicts. Similar to Hankins' findings, the  $Q_1(14)/Q_1(5)$  pair produced the most accurate readings. Table 8 quantifies this accuracy as percent error compared with both Hancock's and Hankins' research.

**Table 8.** Experimental temperature accuracies for the  $Q_1(14)/Q_1(5)$  line pair compared to theoretical data and previous research.

$\Phi$	Theoretical Equilibrium	Hancock	Hancock% Difference	Hankins	Hankins% Difference	Current Experimental	Experimental % Difference
0.4	1425					1105.49	22.4
0.5	1642	1655	0.8	1464	10.8	1400.46	14.7
0.6	1837	1840	0.2	1665	9.4	1642.24	10.6
0.7	2014	2040	1.3	1854	7.9	1817.99	9.7
0.8	2169	2145	1.1	2005	7.6	1997.64	7.9
0.9	2298	2260	1.7	2141	6.8	2129.84	7.3
0.95	2347	2300	2.0	2191	6.6	2169.48	7.6
1	2382	2350	1.3	2170	8.9	2210.13	7.2
1.05	2398	2392	0.3			2229.59	7.0
1.1	2395	2375	0.8	2138	10.7	2248.19	6.1
1.2	2367	2350	0.7	2095	11.5	2225.46	6.0
1.3	2328	2310	0.8	2043	12.2	2176.65	6.5
1.4	2288	2275	0.6			2152.52	5.9

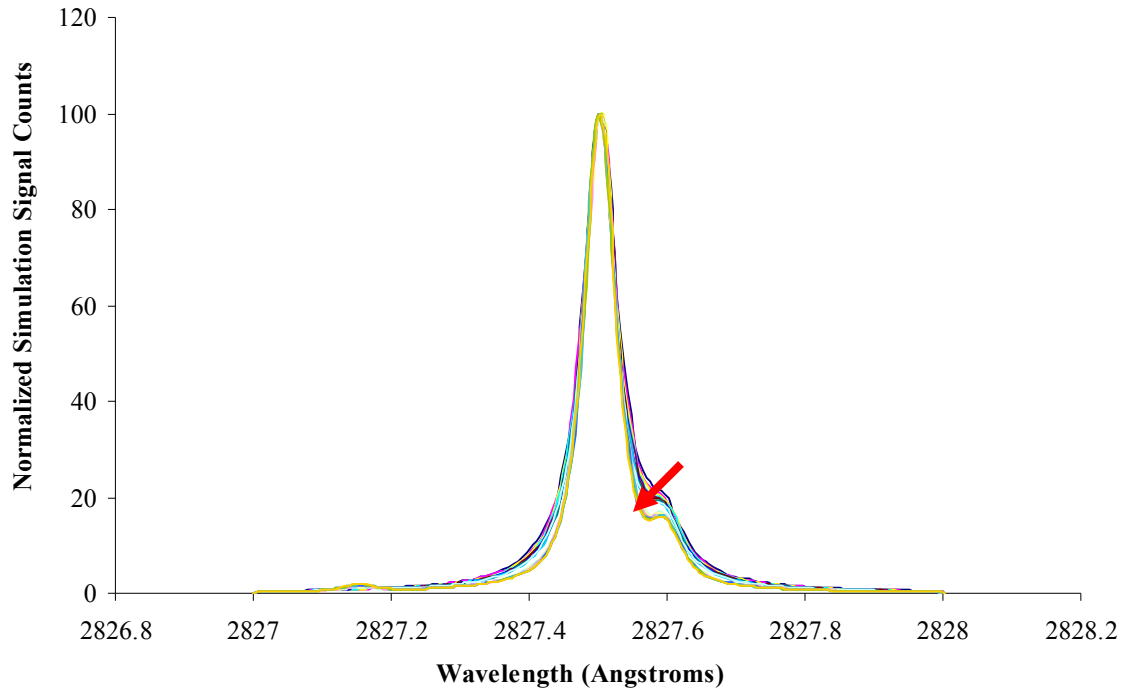
A comparison of experimental data to Hankins' data shows at equivalence ratios below 1, data gathered at the higher location and flow rate is actually less accurate. Above that point, the data shows improved accuracy. This may be due to the higher laser location, but is also possibly due to disproportionality in the co-flow. Because the nitrogen mass flow controller could not provide enough flow maintain the same relationship with the fuel and air flow as in Hancock's and Hankins' studies, it is possible that some mixing occurred at the laser location. Two possible mixing scenarios may have affected the flame. The first, as suggested by Hankins, is entrainment of the cooler co-flow gas. This

would mix with and cool the combusting gases. The second is the mixing of stagnant air from the atmosphere, which would alter the equivalence ratio slightly as it reacted with fuel in the moving flow. In order to evaluate these possibilities, larger mass flow controllers are needed for testing in the lab.

### *Excitation Scan Method*

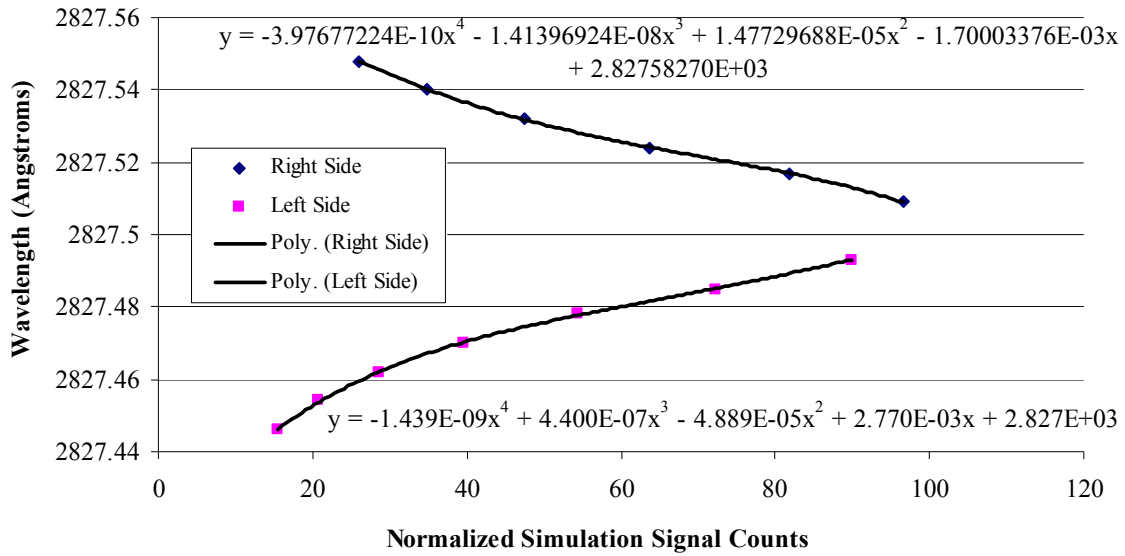
For the excitation scan study, the  $Q_1(5)$  and  $Q_1(14)$  rotational lines were chosen as the energizing wavelengths. The  $Q_1(5)$  line was chosen because of its high signal strength and temperature-insensitivity, as shown in Figure 55. It was expected that using this line would ensure a strong LIF signal at a wide range of equivalence ratios. The  $Q_1(14)$  line was used for comparison. From the Rea study, the collisional broadening coefficients used were as follows:  $Q_1(5) = 0.83$ ,  $Q_1(14) = 0.89$ . (Rea et al., 1986:125) No constant was presented, but 1.0 was found to produce good results.

Similar to the intensity ratio method, the excitation scans began with theoretical work in LIFBASE. Figure 59 shows a plot of the  $Q_1(5)$  line at a range of temperatures.



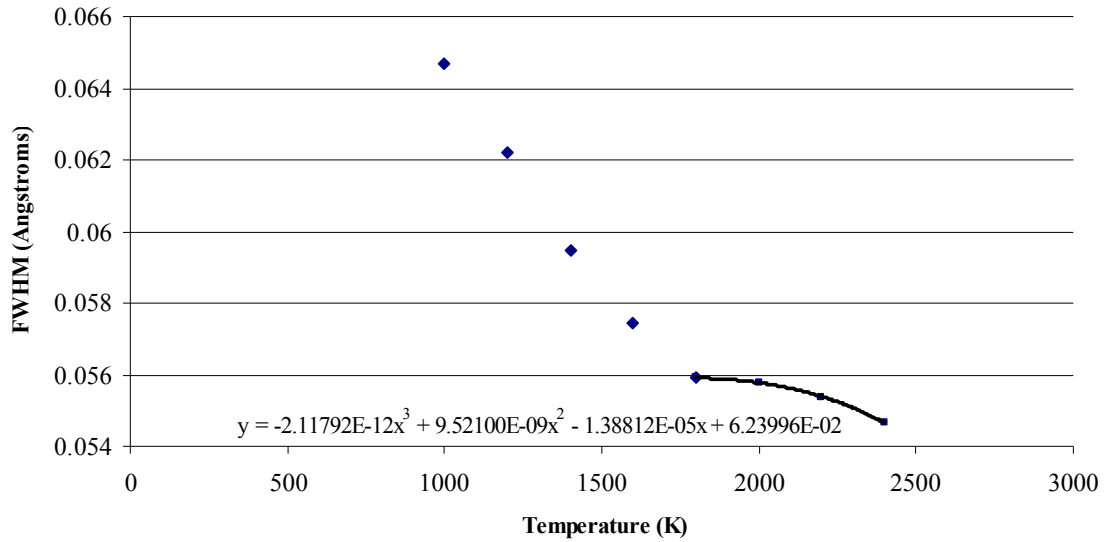
**Figure 59.** LIFBASE simulations of the  $Q_1(5)$  rotational line at a range of temperatures. The red arrow indicates the direction of increasing temperature, and the secondary peak is well below the half-maximum point.

The data gathered from LIFBASE was tabulated by temperature in order to allow FWHM values to be calculated at each point. This was accomplished by plotting both the left side and the right side of the line and calculating a trend line for each. With the trend equation, a wavelength could be calculated at exactly half of the normalized signal strength. This method ensured the most accurate FWHM predictions possible, and is shown in Figure 60 below.



**Figure 60.** An example of the theoretical FWHM calculation method. This LIFBASE data was calculated for the  $Q_1(5)$  line at 2400 K.

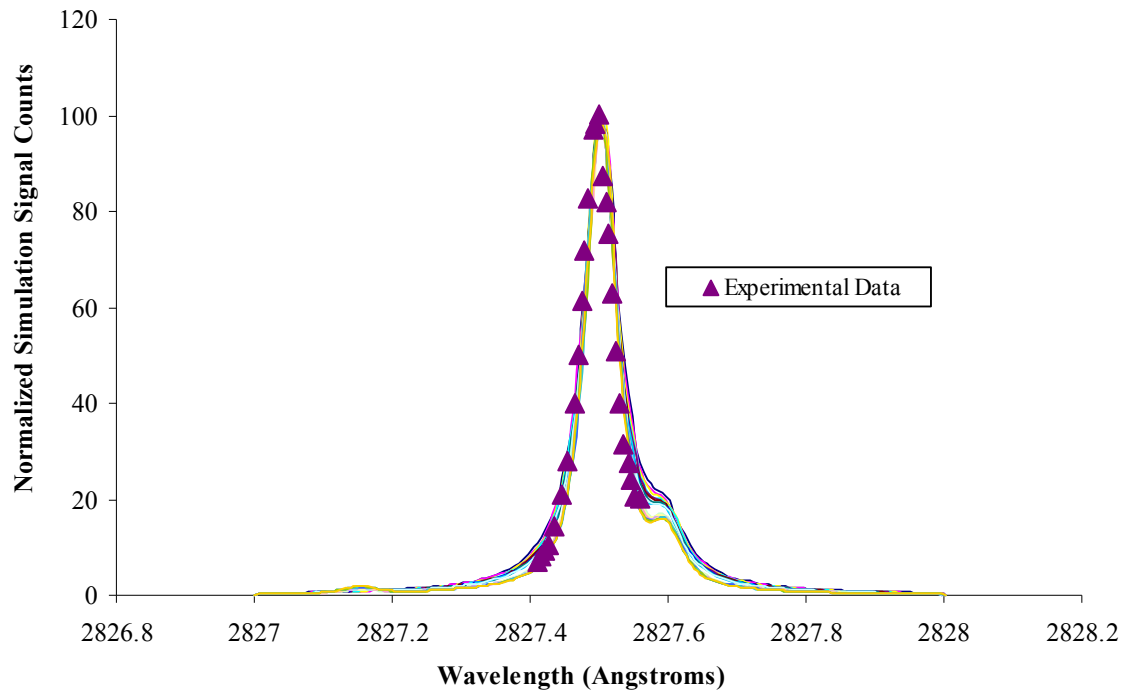
Theoretical FWHM values were calculated using this method for every 2000 degrees Kelvin in the range of possible experimental flame temperatures. By plotting these values and calculating a trend equation in the expected temperature region, an empirical thermometer was again created. The order of the trend equation for each condition was determined by its accuracy relative to the theoretical data, and was not fixed between conditions. The results of this process are shown in Figure 61.



**Figure 61.** Theoretical FWHM trend with temperature for the  $Q_1(5)$  line based on LIFBASE calculations. The black line is the trend line used for thermometry.

The trend line was only calculated in a region of practical flame temperatures in order to ensure its accuracy, and serves as the thermometry equation for the  $Q_1(5)$  line.

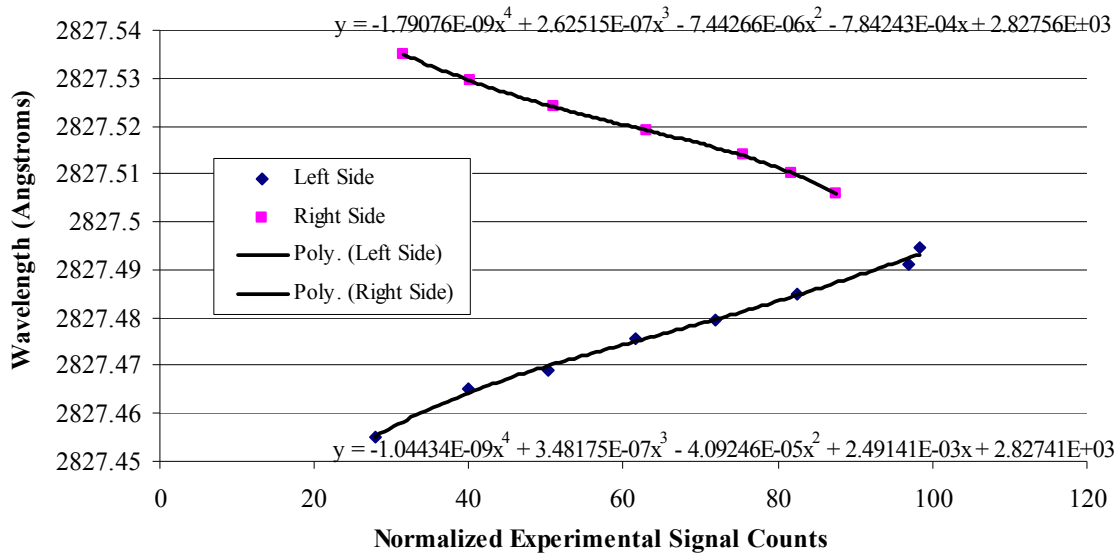
Because of the improved line resolution coming out of the laser system relative to the Hankins study, temperature measurements were possible in this research. Power-corrected intensity data for the  $Q_1(5)$  line gathered at  $\phi = 1$  is presented in Figure 62. The figure shows the experimental data matches closely with the theoretical data.



**Figure 62.** Experimental intensity data gathered for the  $Q_1(5)$  line at an equivalence ratio of one plotted over theoretical data generated by LIFBASE.

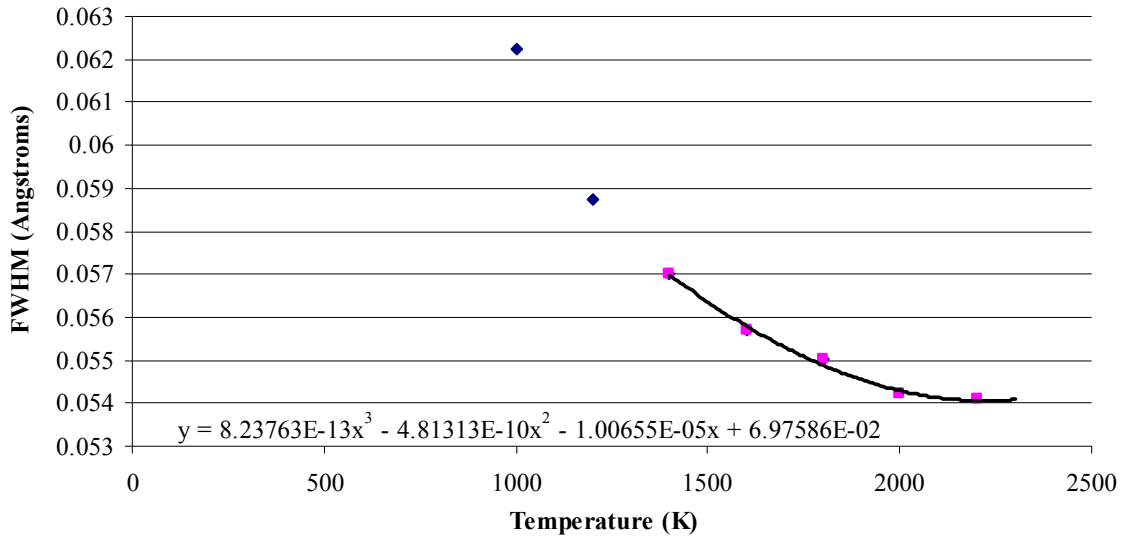
Once the data was collected, it was processed in the same manner as the theoretical numbers in order to generate a FWHM value. Figure 63 shows the plot used for curve-fitting.





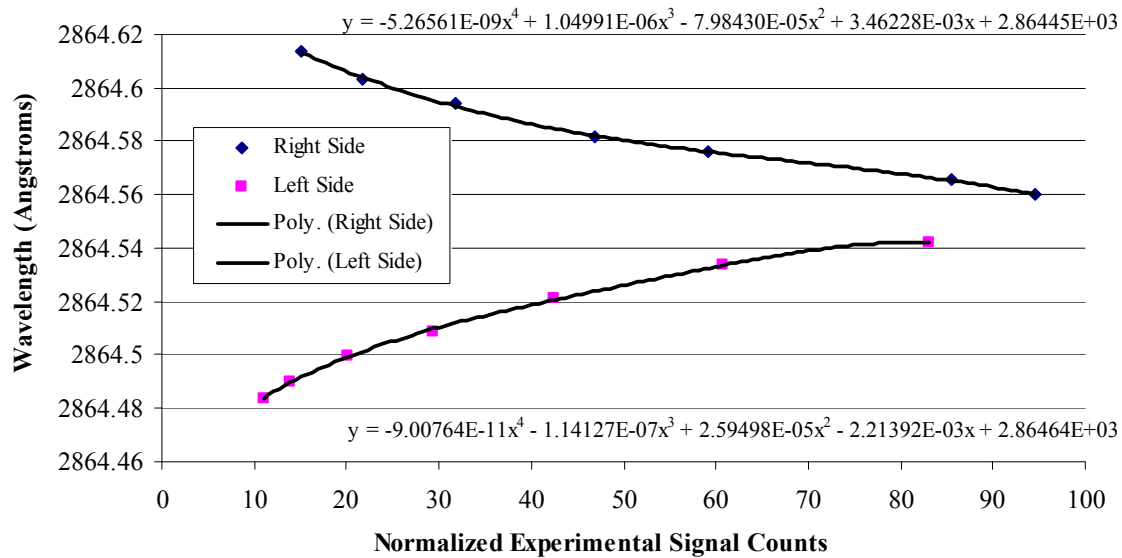
**Figure 63.** The curve-fitting plot used for FWHM calculation for the  $Q_1(5)$  line at  $\phi = 1$ .

Using the trend lines calculated above, the excitation scan for the  $Q_1(5)$  line returned an experimental flame temperature of 2404 K compared to a theoretical temperature of 2383 K, with a percent error of only 0.90%. The  $Q_1(14)$  line was tested in the same manner. The theoretical thermometry equation was calculated using Figure 64, shown below.



**Figure 64.** Theoretical FWHM trend with temperature for the  $Q_1(14)$  line based on LIFBASE calculations. The black line is the trend line used for thermometry.

Data for the  $Q_1(14)$  line was collected at  $\phi = 1$  as well, and the experimental curve-fitting plot for FWHM values is shown in Figure 65.

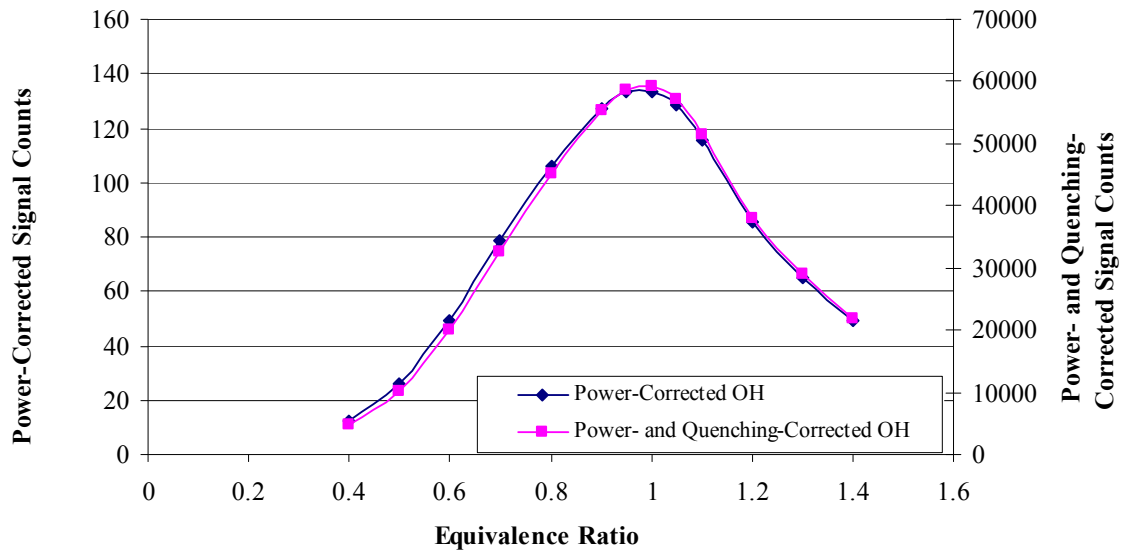


**Figure 65.** The curve-fitting plot used for FWHM calculation for the  $Q_1(14)$  line at  $\phi = 1$ .

As expected, the  $Q_1(14)$  line proved to be less accurate than the  $Q_1(5)$ , returning an experimental flame temperature of 1986 degrees Kelvin and a percent error of 17%. However, neither line is completely trustworthy because of the lack of a definitive constant for use in the collisional broadening correction. This fact highlights the benefit of using the intensity ratio method over the excitation scan method. When dividing intensity ratios, the only correction needed is for power because any correction factors applied to both measurements will cancel out.

### *OH Concentration*

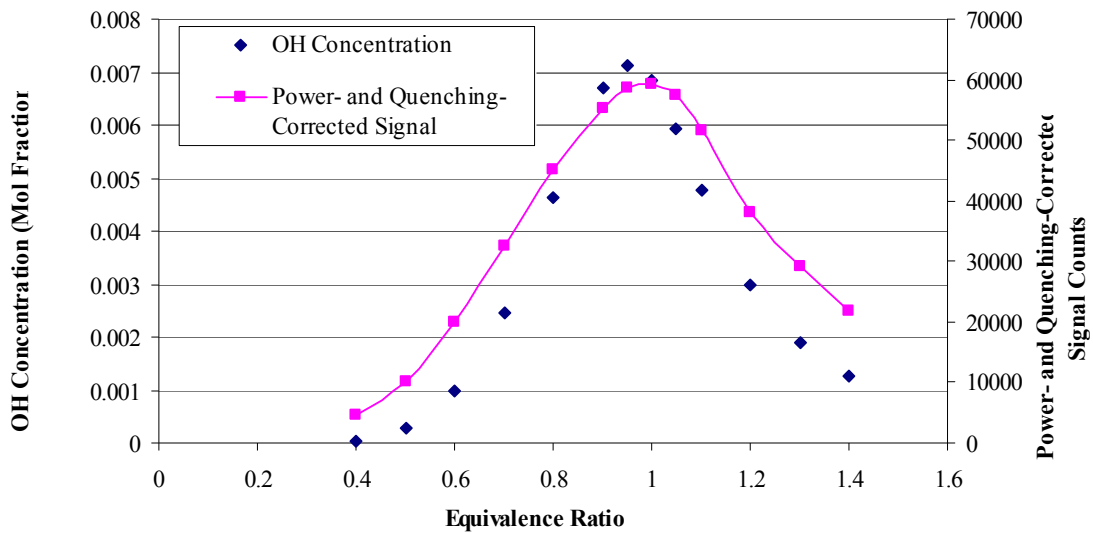
Correlation of the intensity data with OH concentration is also an important aspect of the calibration process. Concentration measurements, however, depend solely on signal counts and not on a measurement's relationship to other data. In order to ensure the accuracy of the correlation, the quenching correction discussed in Section 3.4 was applied in addition to the power and broadening corrections. Figure 66 shows the difference in the relative shapes of the power-corrected and the power- and quenching-corrected intensity curves.



**Figure 66.** Signal counts for power-corrected intensity relative to power- and quenching-corrected intensity.

While only producing a small difference in the curve shape, every effort should be made to improve experimental accuracy.

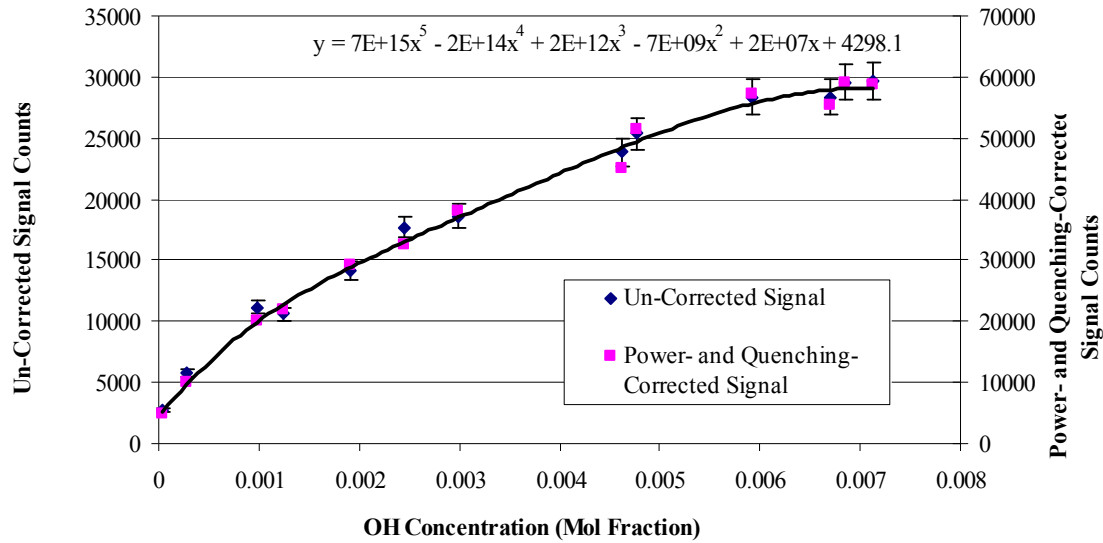
For concentration measurement, the power- and quenching-corrected signal was correlated with theoretical concentration data generated by STANJAN. The relationship between these two quantities is shown with equivalence ratio in Figure 67.



**Figure 67.** OH concentration and power- and quenching-corrected signal versus equivalence ratio.

In order to derive concentration from corrected signal intensity, a method similar to that used in the intensity ratio and excitation scan thermometry techniques was used.

Corrected signal counts were plotted against theoretical OH concentration data and a trend line was calculated. The trend line serves as an equation which can provide OH concentration given a signal intensity or an expected signal intensity given a concentration. Figure 68 shows the plot used to generate the trend equation, and also shows the completely raw signal counts with error bars. The error bars represent the standard deviation of the uncorrected signal. The percent deviation ranges from 4.5% to only 6.0%, which shows the accuracy of the intensity measurements made.



**Figure 68.** Raw and fully corrected signal counts versus OH concentration. Error bars represent the standard deviation of the raw signal in the ROI.

Concentration, like temperature, is an instantaneous measurement. In the COAL lab's current set-up, OH concentration measurements in the UCC section were not possible, but the calibration equations can all be used for future studies once instantaneous laser measurements are possible.

#### 4.2 Igniter Characterization

The two phases of the igniter characterization study were necessary in order to determine first where the igniter was operational, and second to verify that operation in use with the UCC. The open-air test, described in Section 3.3, provided a means to determine the system's flammability range and predict its behavior when connected to the igniter tube.

Initial testing revealed an inability to sustain a flame in the igniter. The only flames observed were highly unsteady, resembling more of a rapid sequence of detonations rather than constant burning, and existed only with the spark plug operating.

With closer examination, it was determined that the spark plug's electrode was recessed too far into its cavity, and no spark was actually in the path of the main flow. This problem was initially resolved by using a spark plug with the negative terminal cut off. In this configuration, the igniter tube's wall opposite the spark plug served as the negative terminal, and sparks arced all the way across the path of the flow. This resulted in successful ignitions. The charge passed through the metal of the igniter tube was not enough to be dangerous, but safety concerns dictated another solution be found.

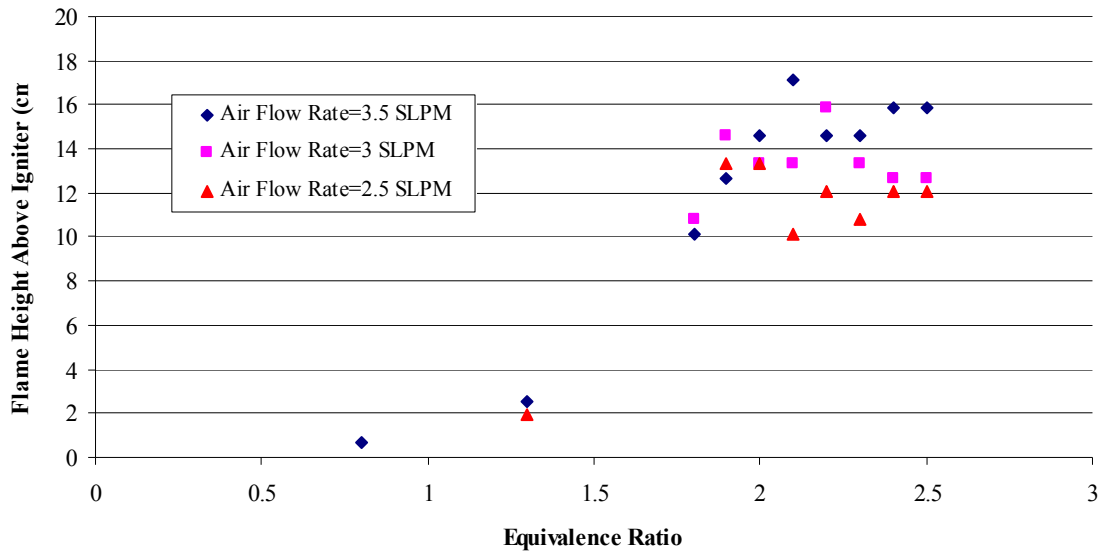
The second, and final solution, uses a spark plug with an extended electrode. This extends both terminals into the path of the flow, but prevents any charge from being carried by the igniter itself. While successful ignition was accomplished in this manner as well, blowout became a problem before the flame height increased enough to propagate down the igniter tube.

In order to determine the relationship between the flame speed of the ethylene, air mixture in the igniter and the velocity of the mixture, Equation 7 was used. Accounting for 274 kPa (25 psig) in the lines leading to the igniter and a temperature drop due to the flow of gas, the flame speed in the igniter was found to be roughly 42 cm/s at  $\phi = 1$ . With 6 mm diameter lines, this equates to a maximum total incoming flow rate (ethylene plus air) of about 7.9 SLPM before blowout. This calculation verified blowout was the problem when attempting to increase the flame height.

Further testing showed the solution to the blowout problem was to incorporate a flame holding mechanism. The device needed to be simple and thin in order to fit inside the igniter tube without increasing the tube's distance. Of several possibilities, inserting a simple washer into the joint between the spark plug section and the tube extension

proved to be the best method. The washer constricts the diameter of the tube to about 5 mm just past the spark plug. With the flame holder in place, steady flames were consistently lit and maintained with the spark plug turned off.

The necessary characterization study could now progress with open-air flame height measurements. First, equivalence ratio was varied in order to determine the system's flammability range and any height variation trends. Figure 69 shows the results of this test with varying equivalence ratio for several air flow rates.



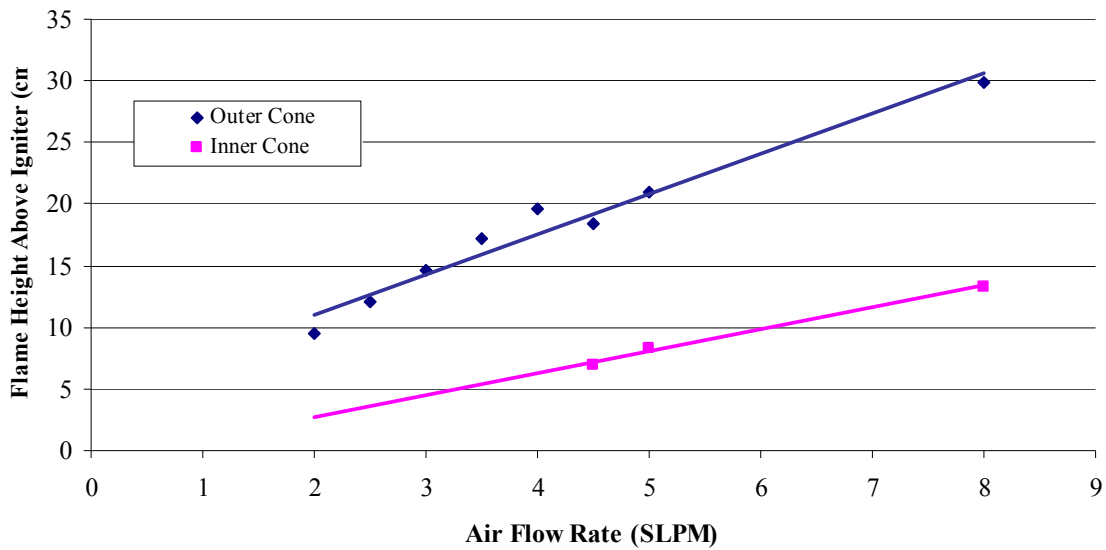
**Figure 69.** Flame height observations with changing equivalence ratio for open-air igniter operation at multiple air flow rates.

With the exception of the three data points left of  $\phi = 1.5$ , flame height was measured only in a steady flame condition. Data left of that operating position was taken at the first sight of any unsteady flame. With this in mind, the plot shows a torch could not be maintained below  $\phi = 1.8$  for any flow rate. Visual observation of the steady operating conditions showed flames initially burning clean and blue, but quickly progressing to a yellow, sooty flame beginning at  $\phi = 2.2$ . Optimum equivalence ratio



for igniter operation was determined to be  $\phi = 2.1$  because of this condition's distance from the edge of flammability and clean burning characteristics.

Overall, the plot shows flammability was not affected by air flow rate, but does indicate a general increase in height with flow rate. Based on this information, a second open-air test was conducted which maintained an equivalence ratio of 2.1 while varying the air flow rate. The results of this test are shown in Figure 70.



**Figure 70.** Flame height observations with changing air flow rate for open-air igniter operation at  $\phi = 2.1$ .

The data from this test clearly validates the previously observed trend that flame height increases with air flow rate. Most importantly, however, increasing the flow rate made observation of the expected inner cone of the flame possible. The height of the inner cone was difficult to measure because of its lack of visible color, but several data points were able to provide a trend which fit well with the measurements for the outer cone. Using this trend, an air flow of 10 SLPM was predicted to be necessary in order to allow the flame to propagate down the full length of the 10 cm igniter tube used in the

UCC and still be sufficient to ignite fuel. However, at this flow rate, even the flame holder was not sufficient to maintain totally steady combustion, and continuous operation of the spark plug was needed.

Generally, the open-air tests showed flame height was primarily a function of air flow rate, while flammability was most dependent on equivalence ratio. With a setting for each state selected, the igniter was attached to the UCC section in order to determine its performance in the operational system. The initial test plan called for the use of a mirror placed in the combustor in order to facilitate a view directly down the igniter tube; but selection was severely limited by size, and the heat of the igniter quickly melted any makeshift system. Observation of the cavity soon showed that no mirror was necessary, however, as the end of a blue flame could easily be seen flickering into and out of the UCC. As time passed, the flicker produced by the igniter moved further into the cavity, and within five minutes filled the bottom with a steadily burning flame. The flame's dependence on time is suspected to be due to a "warm-up" of the igniter system, where the tube itself becomes hot and in turn further heats the gas moving through it. This would have the effect of lowering the activation energy necessary to ignite the ethylene, which would result in the reaction of previously unburned fuel particles in the exhaust.

A final validation of the igniter characterization was accomplished by once again lighting JP-8 in the UCC. Multiple lighting trials all showed the igniter to consistently light the atomized fuel on the first try. Fuel pooling was minimal, and only occurred while the UCC was already lit when the incoming fuel flow rate was raised above a certain level.

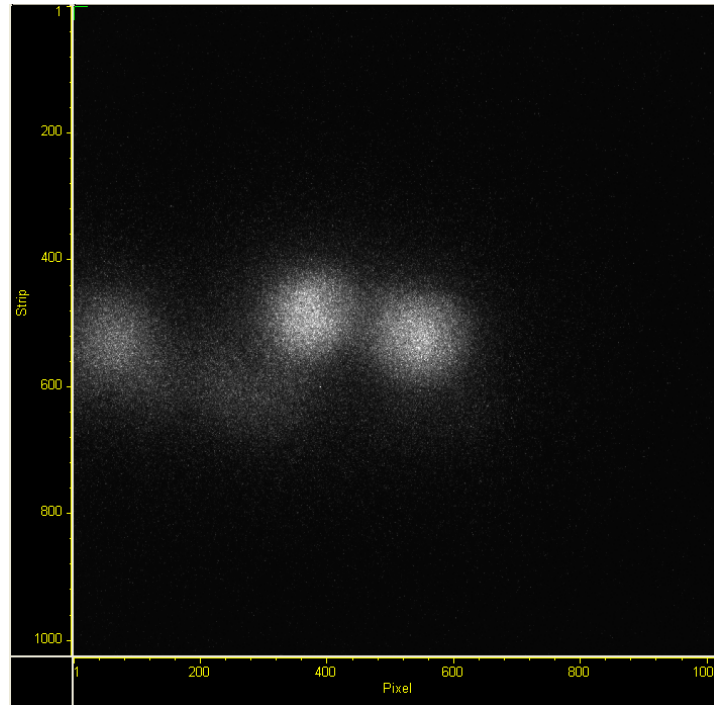
### 4.3 UCC Section Test Results

The results of the PLIF study of the cavity-vane area, as well as dual-vortex and combustor performance observations are presented below. The UCC was used with quartz windows in place and hydrogen as fuel for all three studies.

#### *OH PLIF in the Cavity-Vane Area*

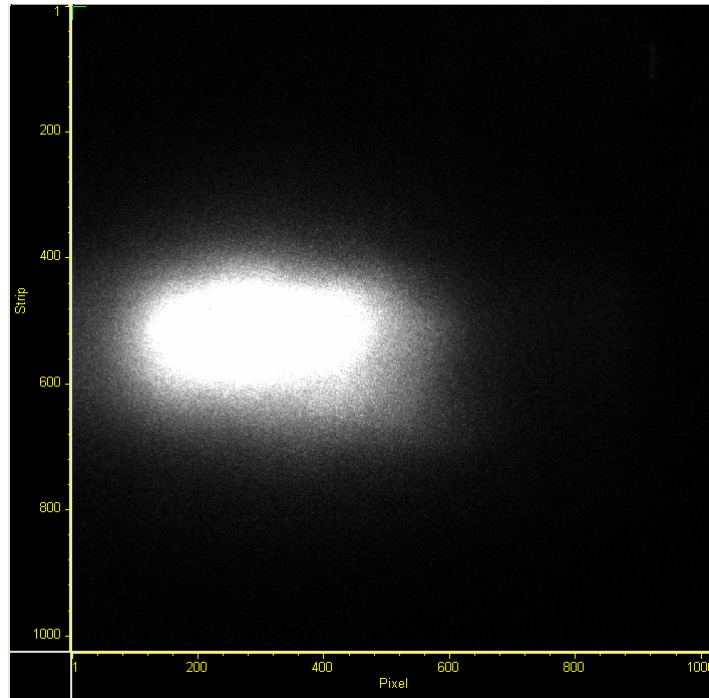
Because the UCC produces a turbulent flame, temperature measurements were not possible with only one laser. Instantaneous temperature measurements for turbulent flow require the use of two-color PLIF, which is not yet available in the COAL lab. However, single-color PLIF is useful for determining flame location, an important quality of any combustion device. Based on the results of the Hencken burner experiment, the temperature-insensitive  $Q_1(5)$  line was used in order to ensure good PLIF signal at any flame regime. For ease of reference, this line was experimentally determined to peak at 282.75 nm. Also, the camera filter configuration was changed to include a second WG-CG-295 glass filter. This further cut down on background signal, improving the single-exposure contrast between LIF signal and background.

As a result of flame turbulence, the image acquisition method was also changed. In order to capture instantaneous views of the flame, it was important to allow only one accumulation per image on the ICCD camera. Gate settings from the Hencken burner experiment were determined to be the best for this set-up, as well. However, one image alone did not provide a good enough sense of the extent of the entrainment of flame and hot products into the main vane, as shown in Figure 71.



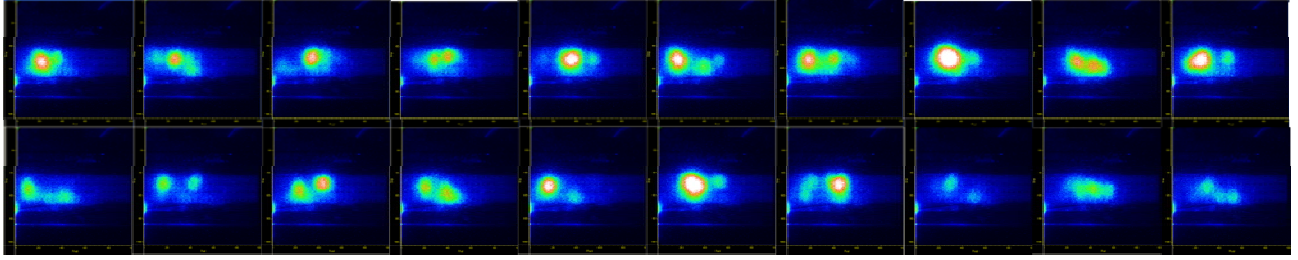
**Figure 71.** A single-accumulation image of OH PLIF in AFIT's flat-cavity UCC section using hydrogen as fuel. Screenshot produced using Win-View 32.

In order to gain a better idea of the full behavior of the flame at every test point, a 20-image average was used for processing. An example of this average is shown in Figure 72.



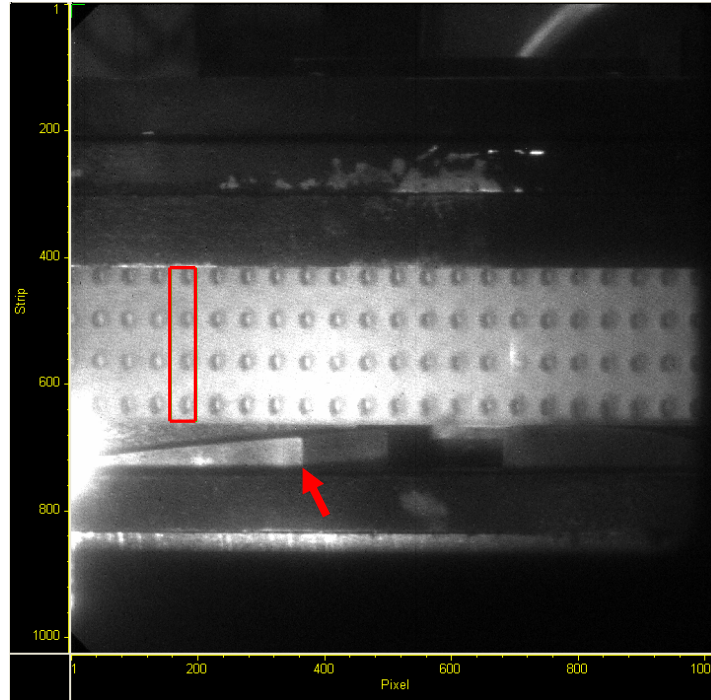
**Figure 72.** An average of 20 images of OH PLIF in AFIT's flat-cavity UCC section using hydrogen as fuel. Screenshot produced by Win-View 32.

This compilation image was created by collecting 20 individual images and subtracting a background image acquired with only the laser firing and no combustion. Win-View 32's average function was then used to create a single compiled image. By creating the average, it was possible to compare the extent of cavity entrainment at any test condition. An example of a 20-image series used to create one of these average images is shown in pseudo-color in Figure 73. This figure shows the impracticality of comparing single-shot images for different test points. It also shows the utility of the pseudo-color function for visual analysis.



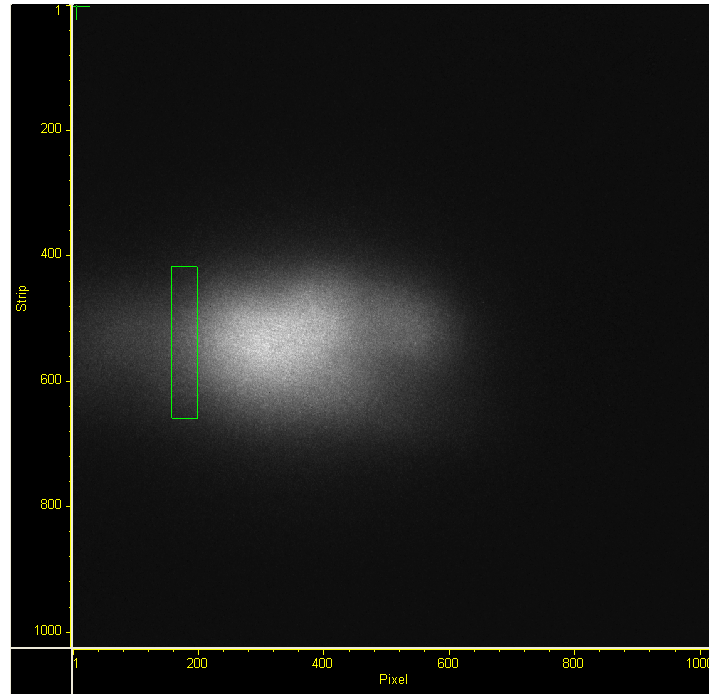
**Figure 73.** A 20-image series shown in pseudo-color of OH PLIF in AFIT's flat-cavity UCC section. For reference to combustor location, the images are overlaid on the focusing image used for camera tuning.

While visual analysis is important, a quantitative method for comparison between test conditions was needed. The ROI technique used for Hencken flame analysis worked well and provided data that closely matched theory, so it was employed again for this study. Since the quality of interest was flame and hot product entrainment into the main vane, an ROI halfway down the radial vane was selected and is shown in Figure 74. The pixel dimensions are as follows: x-axis = 158-198, y-axis = 417-658.



**Figure 74.** Win-View 32 screenshot showing the ROI used for image analysis in the UCC PLIF study. The image used is the camera-focus image, selected for the presence of the calibration aid. The red arrow points to the trailing edge of the RVC.

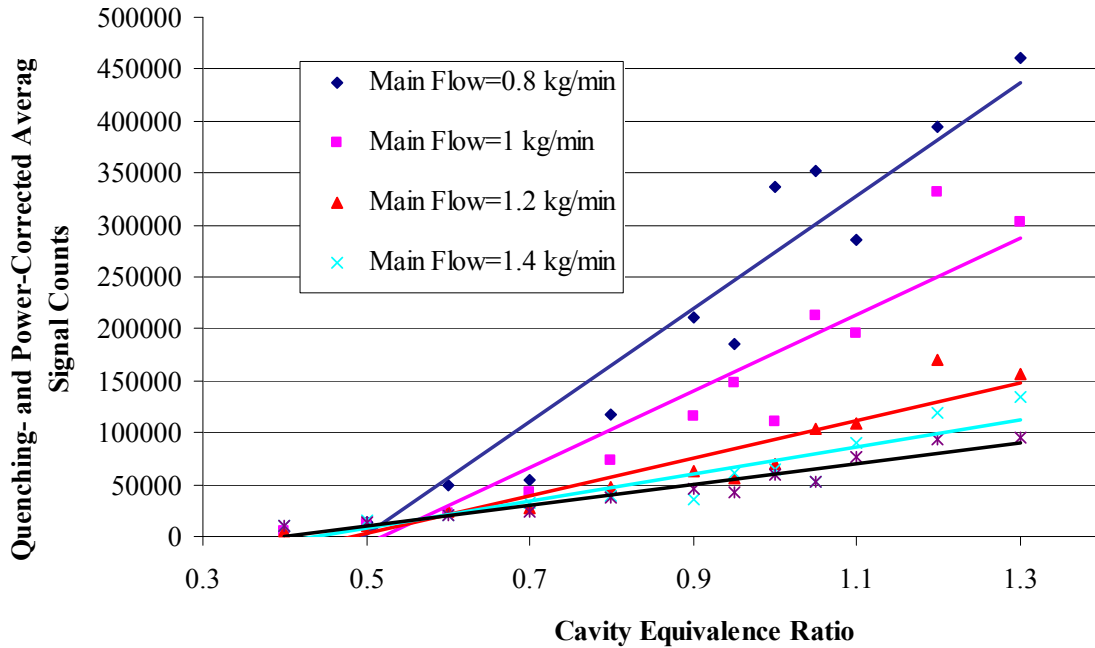
The camera-focus image was used for ROI selection because of the calibration aid's presence and the clarity with which the RVC can be seen. The ROI was placed just beyond the intermediate combustion zone inside the RVC, and was sufficient to provide a good sense of the amount of flame or hot gas leaving the zone. This quantity is extremely important, as it is an indication of the temperature distribution and behavior as the flow enters the turbine section. An average image with the ROI for analysis overlaid is shown in Figure 75.



**Figure 75.** Screenshot of an averaged image of OH PLIF in AFIT's flat-cavity UCC section using hydrogen fuel. The green box overlaid on the image is the ROI used for analysis and comparison. Produced using Win-View 32.

The evaluation of the cavity-vane area began with varying the equivalence ratio at a series of different main flow rates. Varying the cavity equivalence ratio also changes the overall equivalence ratio, which is an additional parameter of interest. The relationship between data points taken at the same main flow rate is an indicator of how quickly flame moves from the cavity into the main vane as overall equivalence ratio changes. The change in the data's trend for each main flow rate indicates the dependence on cavity-to-main flow ratio and overall equivalence ratio. For this test, the laser sheet was aligned just off the main vane wall closest to the cavity, and the cavity flow rate was held at 0.1 kg/min. The results are shown in Figure 76.



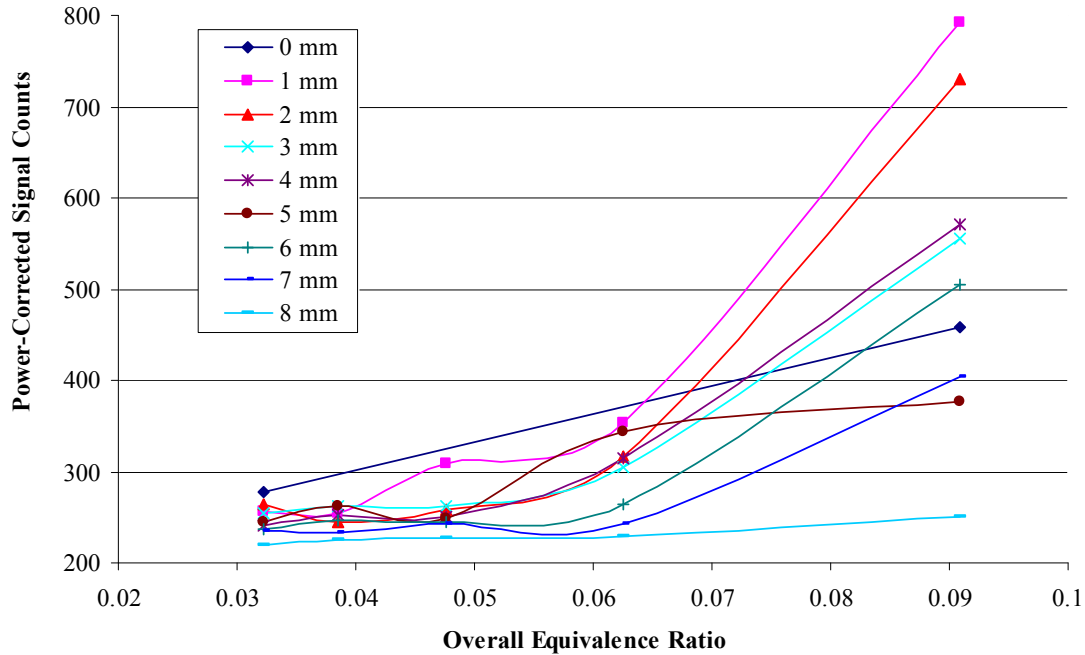


**Figure 76.** PLIF results of varying cavity equivalence ratio at several main flow rates in AFIT's flat-cavity UCC. Images taken in cavity-vane area.

Since the equivalence ratio was varied, both quenching and power corrections were applied to the data. These corrected values show the amount of fire and hot products exiting the RVC increases as cavity equivalence ratio is increased. The plot also indicates a rapid decrease in LIF intensity with increasing main air flow rate, or decreasing overall equivalence ratio. Since this was the property of interest, further study was needed.

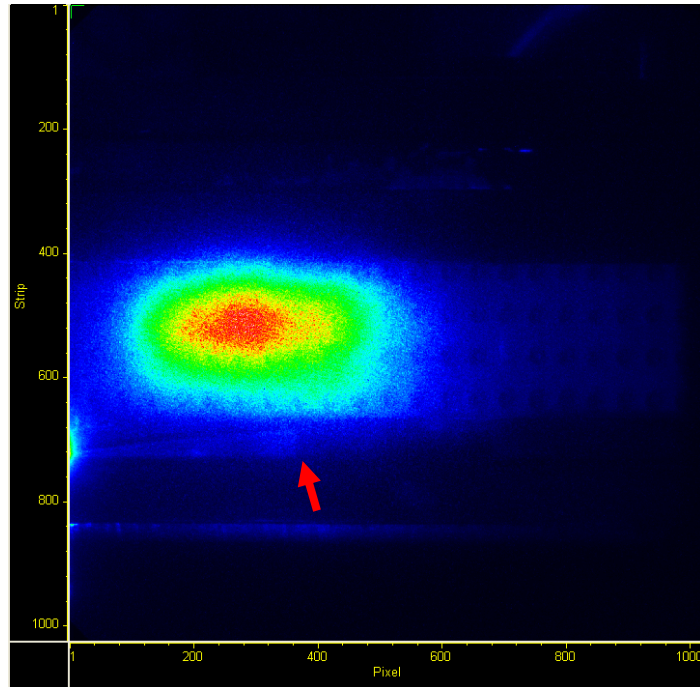
In order to investigate this trend, the cavity equivalence ratio was left at one and cavity flow rate was held constant as a series of main air flow rates were tested. It was also important to examine the temperature trend at different locations across the cavity-vane interaction area. This was accomplished by moving the laser sheet away from the

cavity one millimeter at a time, from one wall to the other, and testing each main flow rate at each laser location. Figure 77 shows the results.

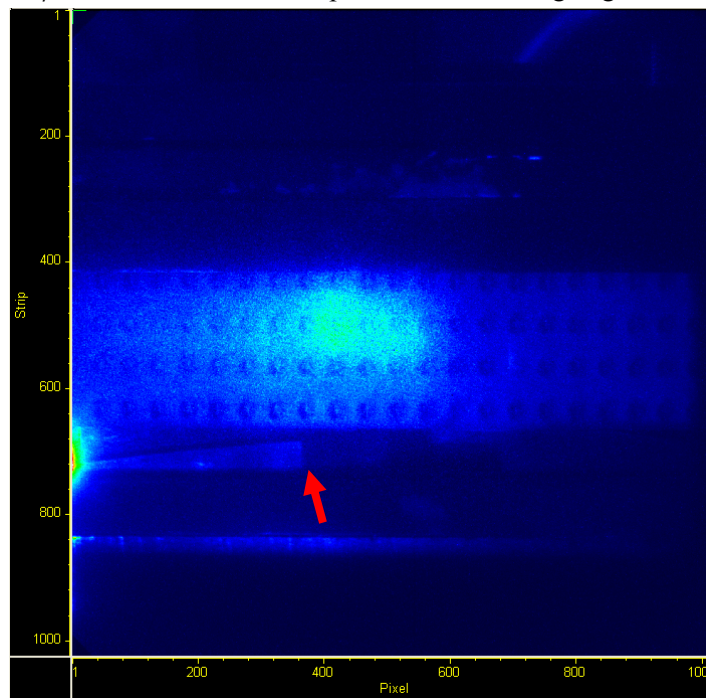


**Figure 77.** PLIF results of varying the main flow rate at several laser sheet locations across the cavity-vane area in AFIT’s flat-cavity UCC section. Test was conducted at  $\phi = 1$  with cavity flow rate held constant.

The plot shows that, for every location, the amount of flame and hot gas present in the ROI does rapidly increase as overall equivalence ratio increases (main flow decreases) between 0.06 and 0.09. This validates the indications seen in the previous test. The trend is roughly level below an overall equivalence ratio of 0.05, showing that the flame is best-trapped in the cavity and RVC below that point. The 0.05 condition corresponds to a cavity-to-main flow ratio of 5%, which is contrary to the TVC research mentioned earlier. The earlier research found that the best cavity-to-main flow relationships for vortex-trapping were 10-20%. Visual references for this behavior are provided in Figures 78 and 79.



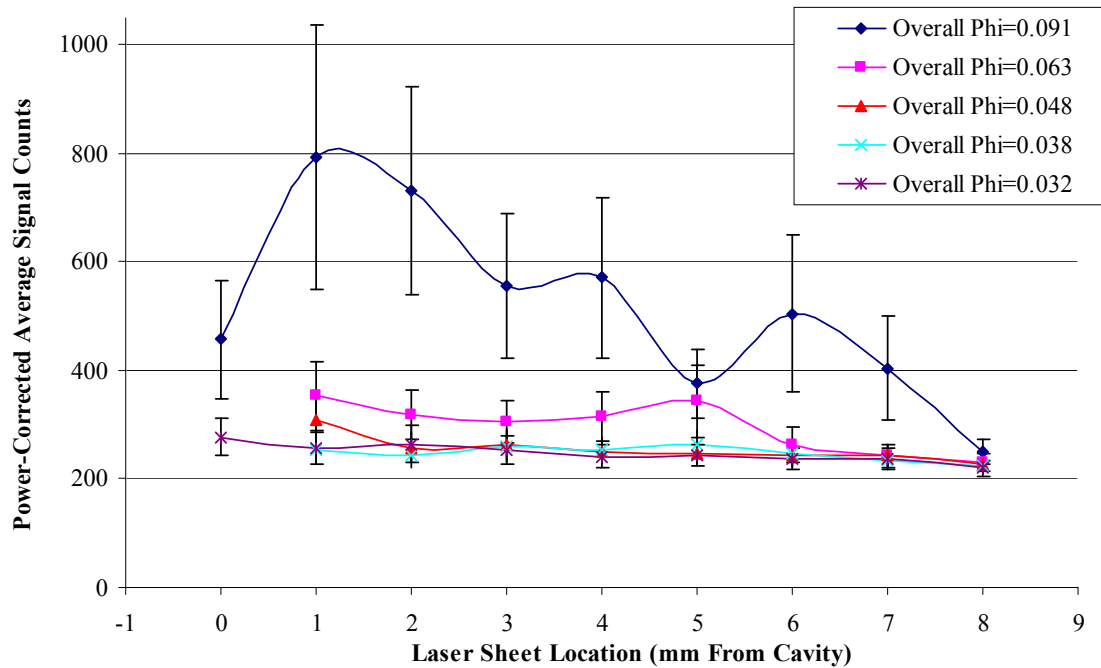
**Figure 78.** A pseudo-color 20-image average OH PLIF screenshot overlaid on the focusing image used for camera tuning. Main flow rate was 1 kg/min, cavity flow rate was 0.1 kg/min, and overall  $\phi = 0.091$ . The red line points to the trailing edge of the RVC.



**Figure 79.** A pseudo-color 20-image average OH PLIF screenshot overlaid on the focusing image used for camera tuning. Main flow rate was 3 kg/min, cavity flow rate was 0.1 kg/min, and overall  $\phi = 0.032$ . The red line points to the trailing edge of the RVC.

Both figures are 20-image averages taken 1 mm away from the cavity-side wall of the main vane superimposed on the camera focus image for reference. The first was taken at an overall equivalence ratio of 0.091, and the second at 0.032. The decrease in LIF signal is indicated by the difference in color scheme. Another important note is the flame's average location relative to the trailing edge of the RVC, indicated by the red arrows. The highest concentration of OH for the higher overall equivalence ratio and lower flow rate actually exists beyond the back edge of the RVC. The conflict in results may be due to the lack of G-load and buoyant forces in the flat-cavity section and future study into this characteristic is necessary.

To get a better idea of the physical location of the flame in the main vane, the same data was reorganized and plotted with laser location on the x-axis. This plot, shown in Figure 80, has physical significance. The 0 mm location represents the main vane wall closest to the cavity, and the 8 mm location represents the wall opposite the cavity.



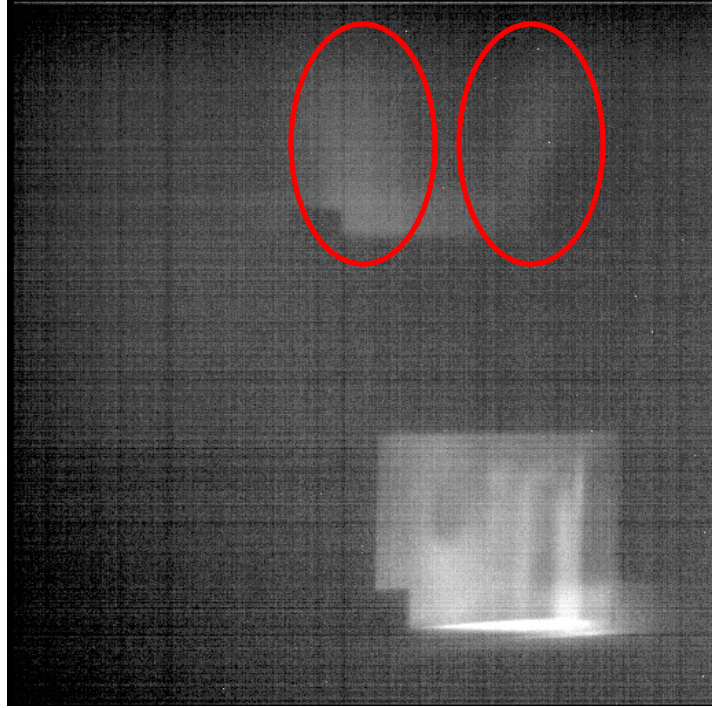
**Figure 80.** PLIF results of varying the laser location at several main flow rates in AFIT’s flat-cavity UCC section. Test was conducted at cavity  $\phi = 1$  with cavity flow rate held constant. Error bars represent one standard deviation from the mean.

Organized in this fashion, it is again clear that the flame and hot products escaping the RVC decrease sharply at overall equivalence ratios below 0.091, which correspond to main flow rates above 1 kg/min. What was not clear previously, however, was the distribution of OH across the main vane. The plot shows at high overall equivalence ratios, the most OH exists near the cavity. This represents an important temperature distribution that will move into the turbine, possibly heating the outer tips of the blades faster or to a higher temperature than the roots. Another important characteristic is that from an overall equivalence ratio of 0.048 down, the OH distribution is nearly constant across the main vane. This trend represents a more desirable, even heating condition for the turbine.

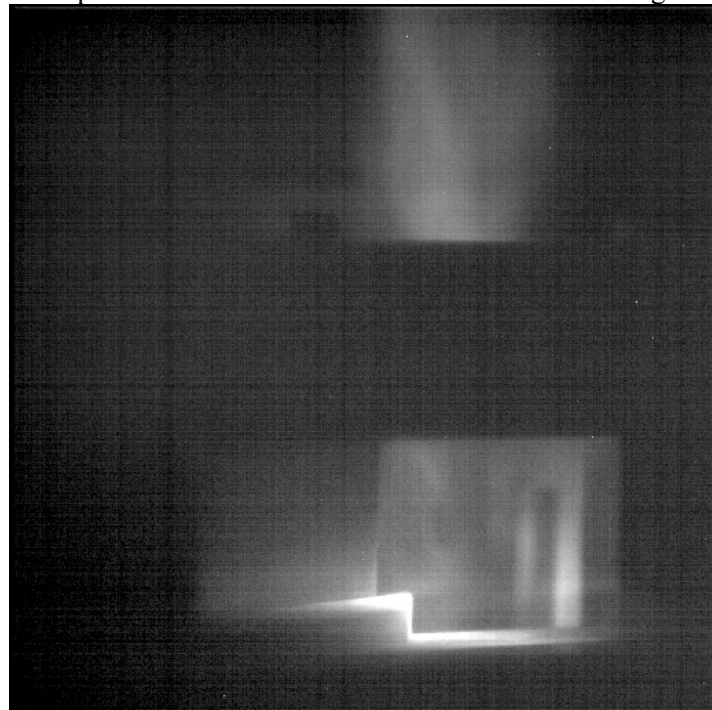
### *Dual-Vortex Observations*

The dual-vortex behavior of the UCC flame noted in the Hankins research was present in the current study, as well, and is shown in Figure 5. This indicates fuel selection has no bearing on the behavior and it is a result of flow dynamics, as expected. The behavior is difficult to characterize because it cannot be quantified, but a review of high-speed images taken during testing gave some insight into the possible cause.

Similar to the PLIF results for flame escaping the RVC, the behavior appears to be most dependent on overall equivalence ratio. Cavity air and equivalence ratio were held constant as in the previous studies, at 0.1 kg/min and cavity  $\phi = 1$ , respectively. As the main flow rate was increased from 0.8 kg/min to decrease the overall equivalence ratio, a transition from two distinct tongues of flame to one large flame exiting the cavity was evident. The change occurred with the main flow set to approximately 20 times the cavity flow (2 kg/min), or an overall equivalence ratio of 0.048. Screenshots of the high-speed video for a high overall equivalence ratio and one below 0.048 can be seen in Figures 81 and 82.



**Figure 81.** Screenshot of high-speed footage of the UCC exhibiting dual-vortex behavior at a high overall equivalence ratio. The red ovals circle the two tongues of flame.



**Figure 82.** Screenshot of high-speed footage of the UCC operating at a low overall equivalence ratio, with only one flame exiting the cavity.

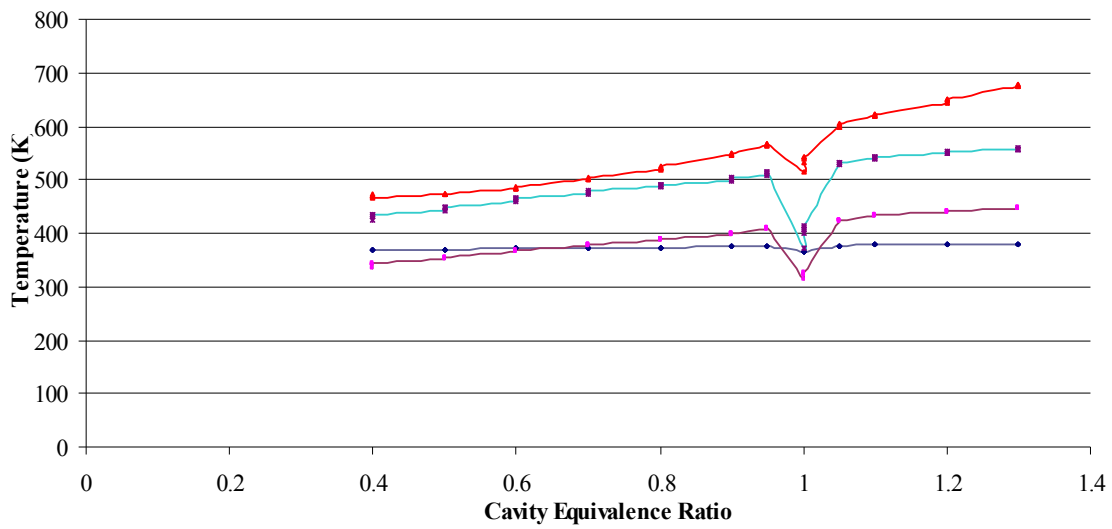
This result is important because, as described previously, it may indicate that the combustor is operating closer to optimum conditions. It is important to note the transition in flame behavior coincides with the drop in OH leaving the RVC found during the PLIF study. This connection and the effects of adding G-load to the flow should be investigated further.

### *Performance Analysis*

Even using hydrogen as fuel, a performance analysis of the UCC is still important as a reflection of the flow dynamics inside the combustor. However, this analysis was limited for the current study due to time considerations. Also, the differential pressure monitor for the main vane in the combustor appears to be malfunctioning. Despite these limitations, several important characteristics are noticeable in the data.

First, general temperature readings were compared with data taken during the Hankins study in order to confirm the equipment's functionality and ensure the data was reasonable. Figure 83 shows a plot of raw temperature data, which matches closely with similar plots in Hankins' thesis in both trend and value.





**Figure 83.** Raw temperature data taken from the UCC and compiled by Lab-View. Main flow and cavity flow were constant at 1 kg/min and 0.1 kg/min, respectively.

With measured data verified to be in the same range as in previous research, trends could be related to combustor performance. Important data recorded using Lab-View is presented in Table 9 by varying main flow rate followed by varying equivalence ratio.

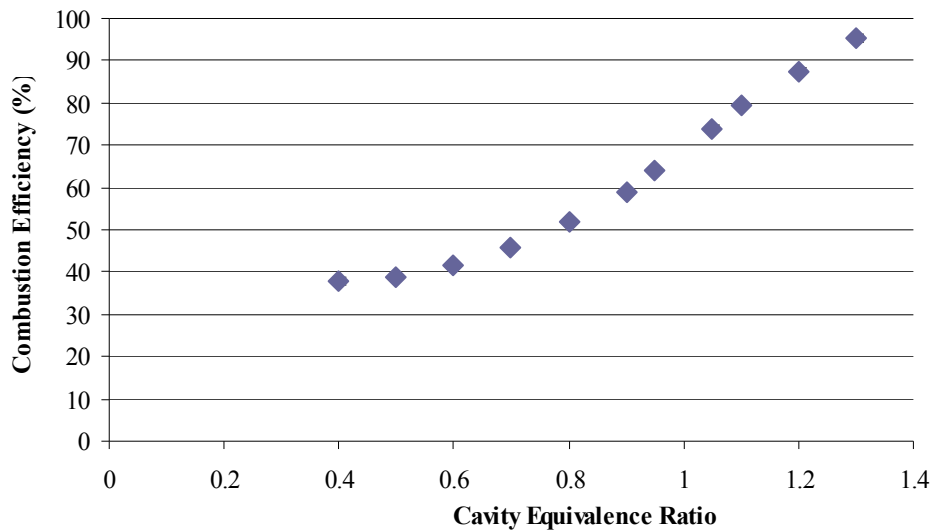
**Table 9.** UCC performance data recorded by Lab-View at a range of operational conditions.

Main Flow Rate (kg/min)	$\Phi$	$\dot{m}_{cav}/\dot{m}_{main}$	$\left(\frac{\Delta P}{P}\right)_{cav}$ (%)	$\eta_b$ (%)
0.80	1.00	0.13	3.85	80.19
1.00	1.00	0.10	3.84	57.08
1.50	1.00	0.07	3.85	83.19
2.00	1.00	0.05	3.84	73.40
2.50	1.00	0.04	3.83	64.39
3.00	1.00	0.03	3.81	61.40
1.00	0.40	0.10	3.79	38.00
1.00	0.50	0.10	3.80	38.66
1.00	0.60	0.10	3.81	41.61
1.00	0.70	0.10	3.82	46.02
1.00	0.80	0.10	3.83	51.75
1.00	0.90	0.10	3.84	58.91
1.00	0.95	0.10	3.85	64.05
1.00	1.00	0.10	3.84	57.08
1.00	1.05	0.10	3.86	74.02
1.00	1.10	0.10	3.87	79.43
1.00	1.20	0.10	3.88	87.42
1.00	1.30	0.10	3.89	95.33

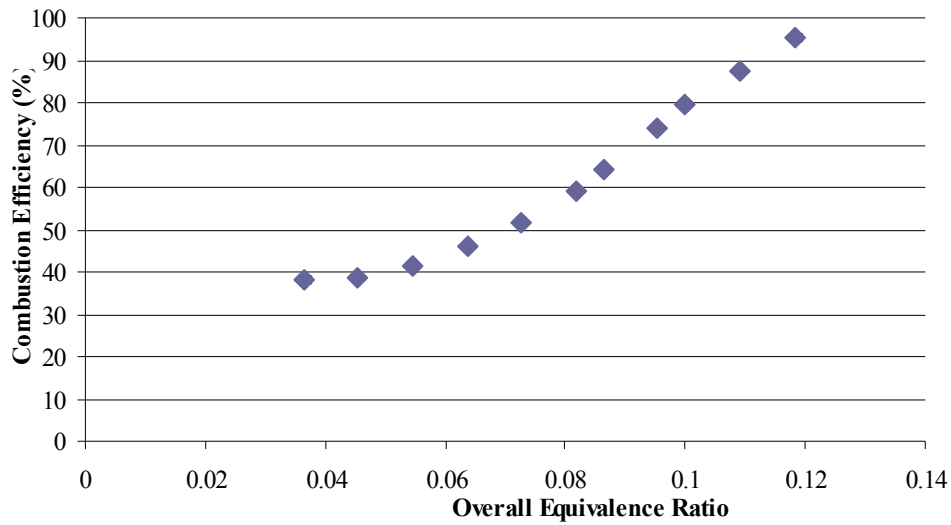
Some of the performance values above are within ranges predicted by Moenter's CFD work. Cavity pressure drop in this experiment ranges from 3.79-3.89%. This is a small fluctuation, but within the 1.15-7.86% range found in the CFD study (Moenter, 2006) and not unreasonable for the short distance between pressure taps. Efficiency data had a much wider range, however, dipping down to 38% at its lowest and only reaching Moenter's range (94.49-99.45%) at a cavity equivalence ratio of 1.3. This discrepancy in values was observed in the Hankins research as well, and is most likely due to inaccurate temperature measurement. The thermocouples are recessed into the steel walls of the

UCC section, and conduction and radiation are estimated to alter these measurements dramatically.

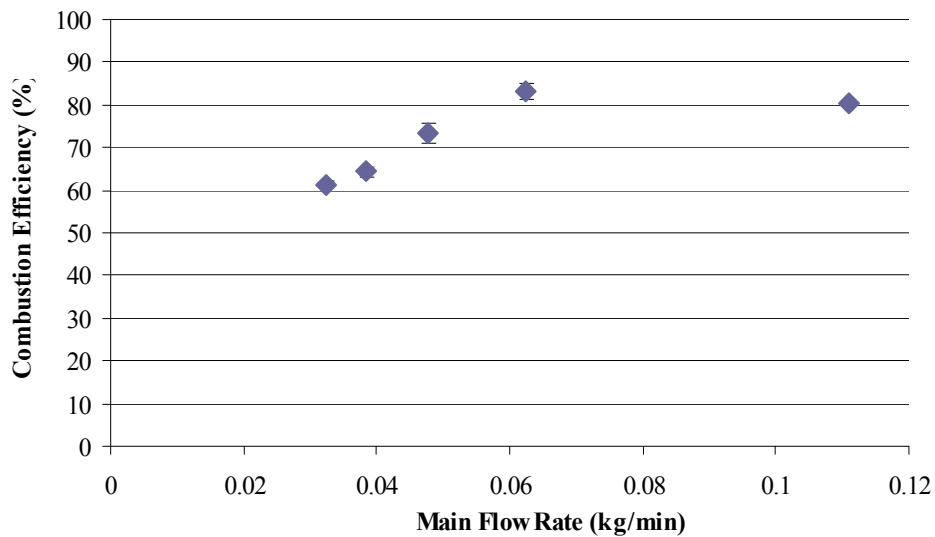
Despite the inaccuracy of the raw data, trends are sometimes more important and are still valid here since the thermocouples were not moved or altered between test runs. In order to examine trends in the combustor's performance, Figures 84, 85, and 86 show efficiency behavior with varying cavity equivalence ratio and overall equivalence ratio, which has an inverse relationship with main flow rate.



**Figure 84.** Combustion efficiency averages calculated from UCC performance data gathered by Lab-View at varying cavity equivalence ratios. Error bars represent one standard deviation from the mean.



**Figure 85.** Combustion efficiency averages calculated from UCC performance data gathered by Lab-View at varying overall equivalence ratios. Error bars represent one standard deviation from the mean.



**Figure 86.** Combustion efficiency averages calculated from UCC performance data gathered by Lab-View at varying overall equivalence ratios. Error bars represent one standard deviation from the mean.

Data gathered at an equivalence ratio and main flow rate of 1.0 depart from the trends, and were thrown out of the analysis. This may be due to that data point being taken first,

before the combustor had warmed up. However, the remaining data exhibits two important characteristics. The first is that performance improved with increasing cavity equivalence ratio. At a high level, this corresponds to increased performance at higher throttle settings, which would be a desirable characteristic if validated in future studies. Figure 85 is shown so that performance data can be referenced to overall equivalence ratio. The second important note is that performance peaks between overall equivalence ratios of 0.065 and 0.11. This corresponds with the transitions in measured data noted in both the PLIF and high-speed footage studies, emphasizing again the importance of the overall equivalence ratio.

## V. Conclusions

### 5.1 Project Overview

The COAL lab has been successfully enhanced, and is ready for all testing planned in the near future. The lab is modular, needing only the combustive apparatus and fuel feed lines to be changed for a variety of studies. Any major malfunctioning systems from previous research were repaired except for the main vane pressure transducers.

The calibration of the PLIF system has also been completed successfully. Temperature and concentration measurements were accomplished and resulted in empirical thermometry and concentration equations that can be used in future studies. Both the intensity ratio and excitation scan methods proved accurate for these measurements. Like previous research, the  $Q_1(14)/Q_1(5)$  line pair was found to be the most accurate set and provided the best signal-to-background contrast. It was also determined that the  $Q_1(5)$  line was the most successful for excitation scans. However, the intensity ratio method is recommended for future temperature studies because of the ability to cancel out several correction factors.

The ignition system for the UCC was also characterized successfully, and an optimum setting for the igniter was determined. The replacement of the spark plug and the addition of a flame holder were important additions to the system that will now make lighting the UCC with any fuel consistent and safe. Recommended settings for the igniter are 10 SLPM of air and an equivalence ratio of 2.1. The UCC operational procedures have been updated to include the 3-5 minute warm-up period, as well as the caution regarding valve operation with the flow controllers on.

For the first time, a non-intrusive laser diagnostic study was performed in a UCC section. Although not able to determine temperature and species concentration, the OH PLIF study conducted did reveal important information regarding flame location and behavior in the cavity-vane area. Results indicated improved vortex-trapping at lower overall equivalence ratios and higher main flow rates relative to the cavity flow rate, indicating a more consistent temperature distribution heading into the turbine. This differs from previous experimentation, and will provide a baseline study to evaluate the effects of adding G-loading to the flow.

Finally, a correlation was drawn between the UCC's dual-vortex behavior, performance characteristics, and overall equivalence ratio. The transition from dual-vortices to a single flame exiting the cavity, as well as a peak in performance, coincided with the drop in OH present in the main vane. This shift occurred with the main flow rate roughly 20 times that of the cavity at an overall equivalence ratio of 0.048.

## **5.2 Future Work and Recommendations**

The COAL lab would benefit from the addition of a larger flow controller. This would allow co-flow rates to maintain the needed relationship with fuel and air flow rates to improve calibration, and would also allow for increased flow rates in the UCC when using gaseous fuel. A 100 SLPM flow controller would fulfill this need. Also, it is very important to pay attention to the heaters for the air delivery system, which frequently overheated and led to inconsistent air temperatures. It is recommended that the air lines be set at high flow rates while the heaters initially warm up in order to prevent this problem. Additionally, repairing the main vane pressure transducers would enhance future research.




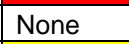

A characteristic of the flat-cavity UCC section that could not be analyzed was the presence of a flame trailing from the back edge of the RVC at most flow conditions. This flame was below the horizon of the laser sheet, and thus could not be studied. Firing the laser through different locations might provide insight into this behavior, and will allow the investigation of flame location, temperature, and species concentration in different areas of the combustor. For any future study using single-laser PLIF in either UCC section, it is recommended that more images be collected for each average shot created. This will increase signal-to-background contrast, and ensure the full extent of the turbulent flame is analyzed.

Future UCC studies should include two-color PLIF in order to measure temperature and species concentrations at a single instant with the turbulent flame. Other laser diagnostic techniques will be important to determine turbulence statistics and the shape of the flow field. Important issues that need to be addressed are the dual-vortex behavior and the drop in flame exiting the RVC with increased overall equivalence ratio. These trends should be evaluated with the curved-cavity UCC section attached, using this study as a baseline in order determine the effects of G-loading.




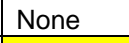



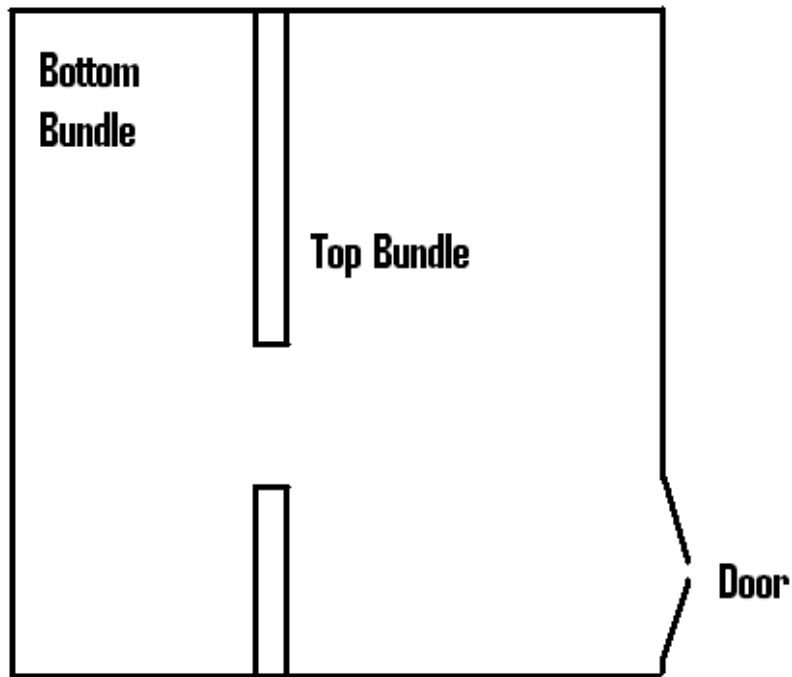
## Appendix A: Tank Farm Configuration

### Top Bundle

	Color	Gas	Name	Concentration	
Blue		H <sub>2</sub> /He	Hydrogen/Helium Blend	40% / 60%	S1
Green		C <sub>2</sub> H <sub>4</sub>	Ethylene		
Red		H <sub>2</sub>	Hydrogen	High	
Plain	None	None			
Yellow		N <sub>2</sub>	Nitrogen		
Black		None			
White		Zero Air	Air		

### Bottom Bundle

	Color	Gas	Name	Concentration	
Blue		CO	Carbon Monoxide	High	S2
Green		CO	Carbon Monoxide	Low	S1
Red		CO <sub>2</sub>	Carbon Dioxide	High	S2
Plain	None	CO <sub>2</sub>	Carbon Dioxide	Low	S1
Yellow		NO <sub>x</sub>	Nitrous Oxide	High	S2
Black		C <sub>3</sub> H <sub>8</sub>	Propane	High	S2
White		O <sub>2</sub>	Oxygen		S1



**Tank Farm**

## Appendix B: COAL Lab Operational Procedures

### Lab Equipment Start-Up:

1. Turn ON valve feeding black air tank for instrument air
2. Turn ON computer
  - a. Open LabView
  - b. Open “Combustion Lab- Anderson Final.vi”
3. Turn ON power strip in back of computer cabinet (powers the DC supply, SCXI 1100 and DAQPad 6508)
4. Turn ON DAQ pad
5. Press “Run” on “Combustion Lab- Anderson Final.vi”
  - a. Listen for fuel pumps to turn on (takes 5 sec)
6. Wait until pressure in control valve to IPT<sup>2</sup> reads 20-40psi and control valve to other equipment reads 80-90psi
7. Turn on “Equip” switch

### Hencken Flame Start-Up:

1. Turn on Fuel, Air, and Nitrogen in tank farm
2. Open valves for Fuel, Air, and Nitrogen on wall behind MOKON machine
3. Set desired mass flow rates on flow controller
  - a. Turn “On” controller
  - b. Turn “Display Channel” to desired channel
    - i. Channel 1- Fuel
    - ii. Channel 2- Air
    - iii. Channel 3- CO-Flow (Nitrogen)
  - c. Push Up and Hold “Set Pt.”
  - d. Turn screw to desired percentage
  - e. Desired Equivalence Ratios for Hydrogen can be found in “Equivalence Ratios for H2.xls” on desktop
4. Turn On “Fan” switch
5. Click On “Ethylene and Air Valves” and “Fuel Line Purge” toggle switch in LabView control panel. \*Valves must be opened before flow controllers are turned on\*
6. Turn On Channel 2 (Air) on mass flow controller and let stabilize
7. Turn On Channel 1 (Fuel) on mass flow controller
8. Light Flame
9. Once lit, turn On Channel 3 (CO-Flow) on mass flow controller
10. Equivalence ratios may be changed on the mass flow controller during operation

### UCC Start-Up Procedure

1. Run all steps in “Lab Equipment Start-Up” above
2. Turn on all bottles in the tank farm
3. Open manual ball valves on main and secondary rig air lines
4. Turn ON main and secondary Gaumer heater circuit breakers

- a. Turn the black lever to ON
  - b. Push the green button
5. Turn ON the “Fan” switch to turn on the exhaust
6. Set the desired main and secondary flow rates on the LabView control screen
7. Turn ON the main and secondary air lines on the control screen
  - a. It will take a few seconds for the air to reach a steady state condition
8. Once air is running, set the desired air line heater temperatures on the control screen
  - a. It will take approximately 30 mins for the rig to heat up
9. Turn ON Mokon oil machine
  - a. Check fluid level
  - b. Make sure bypass valve is open
  - c. Open chiller lines and ensure they are running
  - d. Turn Power ON
  - e. Press and Hold the “Start” button for 10 sec
  - f. Set temperature to 350°F
  - g. Check and make sure discharge pressure is below 40 psi
  - h. Close the bypass valve to allow the oil to reach the probe
  - i. Hold down the “Purge” button for a couple mins to get the air out of the lines
  - j. Make sure pressure does not get too high
  - k. It takes about 15 mins for the probe to heat up
10. Turn on California Analytical Instruments gas analyzer
  - a. Check that the VI reading match the analyzer output
  - b. Make sure emissions temperature is set to 340°F at control station
  - c. Make sure emissions temperature control is set to 350°F at gas analyzer
  - d. Make sure emissions filter is set to 200°F at gas analyzer
  - e. Make sure pressure, temperature, and humidistat readings are reasonable
11. Open valves for C<sub>2</sub>H<sub>8</sub>, Air, and Nitrogen on wall behind MOKON machine
12. Set desired mass flow rates on flow controller
  - a. Turn “On” controller
  - b. Turn “Display Channel” to desired channel
    - i. Channel 1- Fuel
    - ii. Channel 2- Air
  - c. Push Up and Hold “Set Pt.”
  - d. Turn screw to desired percentage
13. Click ON “Ethylene and Air Valves” in VI \*Valves must be opened before flow controllers are turned on\*
11. Turn On Channel 2 (Air) on mass flow controller and let stabilize
12. Turn On Channel 1 (Fuel) on mass flow controller
14. Turn on “Ignitor” and allow to warm-up for 3-5 mins
15. Open manual fuel line valve at combustor stand
16. Set the desired JP-8 fuel flow rates
17. Turn ON the “Fuel Valve” on the VI

18. Turn ON the “Fuel Pump” switch at the VI
19. Once the combustor is ignited turn OFF Channel 1 and Channel 2 on mass flow controller
20. Turn OFF “Ethylene and Air Valve” \*Do not close until flow controllers are off\*
21. Turn OFF “Igniter”
22. Turn OFF Mass Flow Controller
23. Change air and fuel flow to desired settings
24. Proceed with experiment

### **UCC Shutdown**

1. Turn OFF Fuel Pumps
2. Turn OFF “Fuel Valve”
3. Set air line heater temperatures to 0
  - a. It will take at least 30 mins for the heaters to cool down
  - b. Do NOT turn air or heaters off until below 150°F
4. Turn ON “Fuel Line Purge”
5. Once all fuel has been purged out of the system, turn OFF “Fuel Line Purge”
6. Turn ON “Probe Purge”
7. Once emission line is purged, turn OFF “Probe Purge”
8. Turn off California Analytical Instruments analyzer
9. Turn Mokon machine temperature to 0
  - a. It will take at least 15 mins for the Mokon machine to cool down
  - b. Do NOT turn off machine until below 150°F
10. Once air temperatures for main and secondary line are below 150°F, click OFF main and secondary air lines
11. Manually turn OFF electric heater circuit breakers
12. Once Mokon machine is below 150°F turn OFF machine
  - a. Close the chiller lines
  - b. Turn Power OFF
13. Close the ethylene, air, and nitrogen valves at the wall behind the Mokon machine
14. Close all bottles in the tank farm
15. Turn OFF “Fan”
16. Proceed to “Lab Shutdown”

### **Hencken Flame Shutdown:**

1. While running- turn off mass flow controller
2. Click off the “Fuel and Air Valve” and “Fuel Probe Purge” toggle switch in LabView control panel \*Do not close until flow controllers are turned off\*
3. Turn fuel, air, and nitrogen off out in tank farm
4. Close valves for Fuel, Air, and Nitrogen on wall behind MOKON machine
5. Turn off fan
6. Proceed to “Lab shutdown”

**Lab Shutdown:**

1. Turn off “Equip” switch
2. Push “Stop” on Labview
3. Turn off DAQ pad
4. Turn off power strip in back of cabinet
5. Turn off air valve to black tank

## Appendix C: Example STANJAN Calculation

As an example, how to calculate the adiabatic flame temperature of a hydrogen air flame at an equivalence ratio of 1.0 is given. Taken from Hankins' thesis (Hankins, 2008:129-135).

Pressing return or the enter key gives an answer of "no."  
Items in bold print are inputs required by the user.

Select a species data file or <return> if no file is desired.  
Species data file? **COMB.SUD**

Getting species data file COMB.SUD PLEASE WAIT!

C  
C(S)  
CH4  
CO  
CO2  
C12H26  
C3H8  
H  
HO  
H2  
H2O  
H2O(L)  
N  
NC8H18  
NO  
NO2  
N2  
O  
O2

Is this the file wanted? **Y**

Do you want to select REACTANTS or PRODUCTS (r/p)? **R**

Species data file: COMB.SUD

C C(S) CH4 CO CO2 C12H26 C3H8 H  
HO H2 H2O H2O(L) N NC8H18 NO NO2  
N2 O O2

REACTANTS selection: each PHASE is a homogeneous mixture of REACTANTS.  
Type the species in phase 1, separated by commas or blanks; <return> = done.  
\* = all gas species    # = all condensed species    ? = help!

**H2 N2 O2 CO2** (use all caps, when finished press enter)

Species data file: COMB.SUD

C C(S) CH4 CO CO2 C12H26 C3H8 H  
HO H2 H2O H2O(L) N NC8H18 NO NO2  
N2 O O2

REACTANTS selection: each PHASE is a homogeneous mixture of REACTANTS.

Type the species in phase 2, separated by commas or blanks; <return> = done.  
\* = all gas species    # = all condensed species    ? = help!

Do you want to CHECK the ATOMS in the molecules? <return>

Enter the mols of each SPECIES in phase 1 after its name:

H2 : **2** (for phi of 1)

N2 : **3.76**

O2 : **1**

CO2 : **.0016**

This is the CURRENT SETUP:

Reactant phase 1: mols

H2    2.00000E+00

N2    3.76000E+00

O2    1.00000E+00

CO2   1.60000E-03

Do you want to CHANGE the SETUP?<return>

Enter P (atm): **1**

Enter T (K): **298**

The sound speed can be calculated, but then the calculations take longer.

Do you want the SOUND SPEED?<return>

Do you want to SAVE the run OUTPUT in a file?<return>

Do you want to MONITOR the run (probably not)?<return>

Working; PLEASE WAIT!  
OUTPUT READY

Use ctrl-s to stop/start the screen display.

Do you want to see the JANNAF data used?

On IBM-PC, use <ctrl-PrtSc> to start printer (optional).

Computed properties

	atoms	population
C	1.60000000E-03	
H	4.00000000E+00	
O	2.00320000E+00	
N	7.52000000E+00	

Reactants at P = 1.000E+00 atmospheres

species	mol fraction in the phase	mol fraction in mixture	mass fraction in mixture	mols*
---------	------------------------------	----------------------------	-----------------------------	-------

phase 1: molal mass = 20.917 kg/kmol T = 298.00 K

H2	.29579E+00	.29579E+00	.28508E-01	2.00000E+00
N2	.55608E+00	.55608E+00	.74474E+00	3.76000E+00
O2	.14789E+00	.14789E+00	.22625E+00	1.00000E+00
CO2	.23663E-03	.23663E-03	.49788E-03	1.60000E-03

Calculations made using frozen composition.

\* Species mols for the atom populations in mols.

Mixture properties: molal mass = 20.917 kg/kmol

P = 1.0133E+05 Pa V = 1.1690E+00 m\*\*3/kg

U = -1.2308E+05 J/kg H = -4.6284E+03 J/kg S = 8.7750E+03 J/kg-K

Made 0 (T,P) iterations; 0 equilibrium iterations; v 3.96 IBM-PC

On IBM-PC, use <ctrl-PrtSc> to stop printer (optional).

This is the CURRENT SETUP:



Reactant phase 1: mols  
H2 2.00000E+00  
N2 3.76000E+00  
O2 1.00000E+00  
CO2 1.60000E-03

Do you want to CHANGE the SETUP? **Y**

Change options:

- 0 No changes; ready to select run option.
- 1 Select species from a DIFFERENT DATA FILE
- 2 Select DIFFERENT SPECIES (same data file)
- 3 Change REACTANT MOLLS (same reactants)
- 4 Quit STANJAN

Change option? **2**

Do you want to select REACTANTS or PRODUCTS (r/p)? **P**

Species data file: COMB.SUD

C C(S) CH4 CO CO2 C12H26 C3H8 H  
HO H2 H2O H2O(L) N NC8H18 NO NO2  
N2 O O2

PRODUCTS selection: each PHASE is a homogeneous mixture of PRODUCTS.

Type the species in phase 1, separated by commas or blanks; <return> = done.  
\* = all gas species # = all condensed species ? = help!

**H O N H2 HO CO NO O2 H2O CO2 N2**

Species data file: COMB.SUD

C C(S) CH4 CO CO2 C12H26 C3H8 H  
HO H2 H2O H2O(L) N NC8H18 NO NO2  
N2 O O2

PRODUCTS selection: each PHASE is a homogeneous mixture of PRODUCTS.

Type the species in phase 2, separated by commas or blanks; <return> = done.  
\* = all gas species # = all condensed species ? = help!

Do you want to CHECK the ATOMS in the molecules?<return>

This is the CURRENT SETUP:

Atom	population
C	1.60000000E-03
H	4.00000000E+00
O	2.00320000E+00
N	7.52000000E+00

Product phase 1:

H	O	N	H2	HO	CO	NO	O2
H2O	CO2	N2					

Do you want to CHANGE the SETUP?<return>

Run options:

- 0 Abort and redo setup
- 1 Specified T and P
- 2 Specified T and V
- 3 Specified T and S
- 4 Specified P and V
- 5 Specified P and H
- 6 Specified P and S
- 7 Specified V and U
- 8 Specified V and H
- 9 Specified V and S
- 10 A matrix of specified P,T cases (LOTUS file option)
- 11 P and H same as last run
- 12 V and U same as last run
- 13 Specified T, S same as last run
- 14 Specified P, S same as last run
- 15 Specified V, S same as last run
- 16 Chapman-Jouguet detonation of last-run mixture
- 17 One of the above at specified composition
- 18 One of the above under specified linear constraints

Enter run option: **11**

Enter estimated T (K): **2000**

The sound speed can be calculated, but then the calculations take longer.

Do you want the SOUND SPEED?<return>

Do you want to SAVE the run OUTPUT in a file? **Y** (this will put the file in the same directory STANJAN is located)

WARNING! Be sure a disk on which you want to write is in its drive BEFORE you give the file name. If you get an error message attempting to write, do NOT change disks because MS-DOS may destroy the new disk directory! Instead, Abort, or use ctrl-c to go to DOS and start over.

SAVE file name? **PHI 1** (name arbitrarily chosen)

Is this an existing file? **N**

Do you want to keep the data now in the file?<return>

Do you want to MONITOR the run (probably not)?<return>

Working; PLEASE WAIT!

Next time try the state iteration monitor!

OUTPUT READY

Use ctrl-s to stop/start the screen display.

Do you want to see the JANNAF data used?

On IBM-PC, use <ctrl-PrtSc> to start printer (optional).

Computed properties

Independent atom	population	element potential
C	1.60000000E-03	-26.2618
H	4.00000000E+00	-12.1080
O	2.00320000E+00	-17.3633
N	7.52000000E+00	-13.9866

Products at T = 2382.03 K P = 1.000E+00 atmospheres

2382.03 K is the adiabatic flame temperature

species	mol fraction in the phase	mol fraction in mixture	mass fraction in mixture	mols*
phase 1: molal mass = 24.277 kg/kmol				
H	.17968E-02	.17968E-02	.74603E-04	1.04678E-02
O	.54188E-03	.54188E-03	.35713E-03	3.15683E-03
N	.73555E-07	.73555E-07	.42441E-07	4.28509E-07

H2	.15286E-01	.15286E-01	.12693E-02	8.90500E-02
HO	.68379E-02	.68379E-02	.47902E-02	3.98352E-02
CO	.58724E-04	.58724E-04	.67754E-04	3.42108E-04
NO	.26621E-02	.26621E-02	.32905E-02	1.55085E-02
O2	.48100E-02	.48100E-02	.63398E-02	2.80215E-02
H2O	.32370E+00	.32370E+00	.24022E+00	1.88580E+00
CO2	.21592E-03	.21592E-03	.39142E-03	1.25789E-03
N2	.64409E+00	.64409E+00	.74320E+00	3.75225E+00

\* Species mols for the atom populations in mols.

Mixture properties: molal mass = 24.277 kg/kmol

T = 2382.03 K      P = 1.0133E+05 Pa      V = 8.0511E+00 m\*\*3/kg

U = -8.2040E+05 J/kg      H = -4.6287E+03 J/kg      S = 1.1075E+04 J/kg-K

Made 6 (T,P) iterations; 27 equilibrium iterations; v 3.96 IBM-PC

On IBM-PC, use <ctrl-PrtSc> to stop printer (optional).

## Bibliography

Anderson, W. S. *Design, Construction, and Validation of the AFIT Small Scale Combustion Facility and Sectional Model of the Ultra-compact Combustor*. MS thesis, AFIT/GAE/ENY/07-M01. Graduate School of Engineering and Management, Air Force Institute of Technology (AU), Wright-Patterson AFB OH, March 2007.

Anisko, J. *Numerical Investigation of Cavity-Vane Interactions Within the Ultra Compact Combustor*. MS thesis, AFIT/GAE/ENY/06-M01. Graduate School of Engineering and Management, Air Force Institute of Technology (AU), Wright-Patterson AFB OH, March 2006.

Anthenien, R. A., Mantz, R. A., Roquemore, W. M., & Sturgess, G. "Experimental Results for a Novel, High Swirl, Ultra Compact Combustor for Gas Turbine Engines." *2nd Joint Meeting of the United States Section of the Combustion Institute*. Oakland CA, 2001.

Dittman, E. R. *Design, Build and Validation of a Small Scale Combustion Chamber Testing Facility*. MS thesis, AFIT/GAE/ENY/06-M06. Graduate School of Engineering and Management, Air Force Institute of Technology (AU), Wright-Patterson AFB OH, March 2006.

Eckbreth, A. C. In Gupta A. K., Lilley D. G. (Eds.), *Laser diagnostics for combustion temperature and species*. Abacus Press, Tunbridge Wells Kentucky, 2<sup>nd</sup> ed., 1988.

Eckbreth, A. C., Bonczyk, P. A., & Verdieck, J. F. "Combustion diagnostics by laser raman and fluorescence techniques." *Progress in Energy and Combustion Science*, 5, 253-322. 1979.

Eckbreth, A. C. In Gupta A. K., Lilley D. G. (Eds.), *Laser Diagnostics for Combustion Temperature and Species*. Abacus Press, Tunbridge Wells Kentucky, 1998.

"Fuel Consumption by Mode of Transportation in Physical Units." U.S. Department of Transportation: Research and Innovative Technology Administration: Bureau of Transportation Statistics. 2006. < [http://www.bts.gov/publications/national\\_transportation\\_statistics/html/table\\_04\\_05.html](http://www.bts.gov/publications/national_transportation_statistics/html/table_04_05.html)>. May 2008.

Greenwood, R. T. *Numerical Analysis and Optimization of the Ultra Compact Combustor*. MS thesis, AFIT/GAE/ENY/05-M10. Graduate School of Engineering and Management, Air Force Institute of Technology (AU), Wright-Patterson AFB OH, March 2005.

Hancock, R. D., Bertagnolli, K. E., Lucht, R. P. Nitrogen and Hydrogen CARS Temperature Measurements in a Hydrogen / Air Flame Using a Near-Adiabatic Flat-Flame Burner. *Combustion and Flame* 109, pp. 323-331. 1997.

- Hankins, Terry. *Laser Diagnostic System Validation and Ultra-Compact Combustor Characterization*. MS thesis, AFIT/GAE/ENY/08-M14. Graduate School of Engineering and Management, Air Force Institute of Technology (AU), Wright-Patterson AFB OH, March 2008.
- Hill, Phillip G. and Carl R. Peterson. *Mechanics and Thermodynamics of Propulsion*. Addison-Wesley Publishing Company, 2<sup>nd</sup> ed. 1992.
- Hsu, K-Y, and Goss, L. P., "Characteristics of a Trapped-Vortex Combustor," *Journal of Propulsion and Power*, Vol. 14, No. 1. 1998.
- Hunecke, Klaus. *Jet Engines*. Biddles, Ltd. Great Britain, 1997.
- Koether, S. J. *Validation of the AFIT Small Scale Combustion Facility and OH Laser-Induced Fluorescence of an Atmospheric Laminar Premixed Flame*. MS thesis, AFIT/GAE/ENY/07-S03. Graduate School of Engineering and Management, Air Force Institute of Technology (AU), Wright-Patterson AFB OH, September 2007.
- Kohse-Hoinghaus, K. "Laser Techniques for the Quantitative Detection of Reactive Intermediates in Combustion Systems." *Prog. Energy Combust. Sci. Vol. 20 pp. 203-279*. 1994.
- Lefebvre, Arthur H., *Gas Turbine Combustion*, Hemisphere Publishing Corporation, McGraw-Hill Book Company. New York NY, 1999.
- Lefebvre, Arthur H. *Gas Turbine Combustion*. Hemisphere Publishing Corporation, McGraw-Hill Book Company. New York NY, 1983.
- Lewis, G. D. "Swirling flow combustion -- fundamentals and application." *AIAA/SAE 9th Propulsion Conference*. Las Vegas Nevada, 1973.
- Little, B.H. and R.R. Whipkey. "Locked Vortex Afterbodies". *Journal of Aircraft*, Volume 16, No. 5. May 1979.
- Liu, F., & Sirignano, W. A. "Turbojet and turbofan engine performance increases through turbine burners." *38th Aerospace Sciences Meeting and Exhibit*. Reno NV, 2000.
- Mattingly, J. D. *Elements of Gas Turbine Propulsion*. New York: McGraw-Hill, Inc. 1996.
- Mawid, M. A., Thornburg, H., Sekar, B., Zelina, J., "Performance of an Inter-Turbine Burner (ITB) Concept with Three-Different Vane Cavity Shapes," 42<sup>nd</sup> *AIAA/SAE/ASME/ASEE Joint Propulsion Conference & Exhibit*. AIAA-2006-4740. Sacramento CA, July 2006.

- Moenter, D. S. *Design and Numerical Simulation of Two-Dimensional Ultra Compact Combustor Model Sections for Experimental Observation of Cavity-Vane Flow Interactions*. MS thesis, AFIT/GAE/ENY/06-S07. Graduate School of Engineering and Management, Air Force Institute of Technology (AU), Wright-Patterson AFB OH, September 2006.
- Quaale, R. J. *Experimental Results for a High Swirl, Ultra Compact Combustor for Gas Turbine Engines*. MS thesis, AFIT/GAE/ENY/03-5. Graduate School of Engineering and Management, Air Force Institute of Technology (AU), Wright-Patterson AFB OH, 2003.
- Rea Jr., E.C., A.Y. Chang, R.K. Hanson. "Shock-Tube Study of Pressure Broadening of the  $A^2E^+ - X^2\pi (0,0)$  Band of OH by Ar and  $N_2$ ." *Journal of Quant. Spectroscopic Radiation Transfer*. Vol.37, No.2. pp. 117-127. 1987.
- Reynolds, William C. "STANJAN: Equilibrium solver." Stanford University CA, 1995.
- Roquemore, W. M., Shouse, D., Burrus, D., Johnson, A., Cooper, C., & Duncan, B., et al. "Trapped vortex combustor concept for gas turbine engines." *39th AIAA Aerospace Sciences Meeting & Exhibit*. Reno NV, 2001.
- Seitzman, J. M., R. K. Hanson, P. A. DeBarber, and C. F. Hess. "Application of quantitative two-line OH planar laser-induced fluorescence for temporally resolved planar thermometry in reacting flows." *Applied Optics*, Vol. 33, No. 18. June 1994.
- Sirignano, W.A., Delplanque, J.P., and Liu, F. "Selected Challenges in Jet and Rocket Engine Combustion Research." *33<sup>rd</sup> AIAA/ASME/SAE/ASEE Joint Propulsion Conference*. AIAA-97-2701. Seattle WA, 1997.
- Sirignano, W.A. and F. Liu. "Performance Increases for Gas-Turbine Engines Through Combustion Inside the Turbine." *Journal of Propulsion and Power*, Volume 15, No. 1. January-February 1999.
- Spectra-Physics Lasers & Photonics. *Quanta-Ray Lab-Series Pulsed Nd:YAG Lasers User's Manual*. Mountain View CA, 2001.
- Straub, D.L., T.G. Sidwell, D.J. Maloney, K.H. Casleton, and G.A. Richards. "Simulations of a Rich Quench Lean (RQL) Trapped Vortex Combustor." Presented at the AFRC International Symposium, Sept 2000.
- Sturgess, G.J. and Hsu, K.-Y. "Combustion Characteristics of a Trapped Vortex Combustor." Innovative Scientific Solutions, Inc. Beavercreek OH.
- Tamura, Masayuki, Pamela A. Berg, Joel E. Harrington, Jorge Luque, Jay B. Jefferies, Gregory P. Smith, and David R. Crosley. "Collisional Quenching of CH(A), OH(A),

and NO(A) in Low Pressure Hydrocarbon Flames.” *Combustion and Flame*. Vol 114, pp. 502-514. 1998.

Thornburg, H., Sekar, B., Zelina, J., and Greenwood, R. “Numerical Study of an Inter-Turbine Burner (ITB) Concept with Curved Radial Vane.” 45<sup>th</sup> *AIAA Aerospace Sciences Meeting and Exhibit*. AIAA-2007-649. Reno NV, January 2007.

Turns, S. R. *An Introduction to Combustion* (2<sup>nd</sup> Ed.). New York: McGraw-Hill, Inc., 1996.

“United States.” *The CIA World Factbook*. May 2008. < <https://www.cia.gov/library/publications/the-world-factbook/geos/us.html>>. May 20, 2008.

Yonezawa, Y., Toh, H., Goto, S., & Obata, M. “Development of the jet-swirl high loading combustor.” *AIAA/SAE/ASME/ASEE 26th Joint Propulsion Conference*, Orlando FL, 1990.

Zelina, J., Shouse, D. T., & Neuroth, C. *High Pressure Tests of a High-g Ultra-Compact Combustor*. 2005.

Zelina, J., Sturgess, G. J., Manour, A., & Handcock, R. D. *Fuel injector design for an ultra-compact combustor*. No. ISABE-2003-1141. 2003.

Zelina, J., Sturgess, G. J., & Shouse, D. T. *The Behavior of an Ultra-Compact Combustor (UCC) Based on Centrifugally-Enhanced Turbulent Burning Rates*. 2004.



## VITA

Ensign Patrick J. Lakusta graduated from Flower Mound High School in Flower Mound, Texas. He reported to the U.S. Naval Academy in July of 2003 and was commissioned on May 25, 2007 with a B.S. in Aerospace Engineering. Upon graduating, he entered the Air Force Institute of Technology's Graduate School of Engineering and Management. His next assignment will take him to Naval Air Station Pensacola, Florida to begin the pipeline as a Student Naval Aviator.

## REPORT DOCUMENTATION PAGE

*Form Approved*  
*OMB No. 074-0188*

The public reporting burden for this collection of information is estimated to average 1 hour per response, including the time for reviewing instructions, searching existing data sources, gathering and maintaining the data needed, and completing and reviewing the collection of information. Send comments regarding this burden estimate or any other aspect of the collection of information, including suggestions for reducing this burden to Department of Defense, Washington Headquarters Services, Directorate for Information Operations and Reports (0704-0188), 1215 Jefferson Davis Highway, Suite 1204, Arlington, VA 22202-4302. Respondents should be aware that notwithstanding any other provision of law, no person shall be subject to a penalty for failing to comply with a collection of information if it does not display a currently valid OMB control number.

**PLEASE DO NOT RETURN YOUR FORM TO THE ABOVE ADDRESS.**

<b>1. REPORT DATE (DD-MM-YYYY)</b> 19-06-2008		<b>2. REPORT TYPE</b> Master's Thesis		<b>3. DATES COVERED (From – To)</b> June 2007 – June 2008	
<b>4. TITLE AND SUBTITLE</b>  Laser-Induced Fluorescence and Performance Analysis of the Ultra-Compact Combustor				<b>5a. CONTRACT NUMBER</b>	
				<b>5b. GRANT NUMBER</b>	
				<b>5c. PROGRAM ELEMENT NUMBER</b>	
<b>6. AUTHOR(S)</b>  Lakusta, Patrick J., ENS, USN				<b>5d. PROJECT NUMBER</b>	
				<b>5e. TASK NUMBER</b>	
				<b>5f. WORK UNIT NUMBER</b>	
<b>7. PERFORMING ORGANIZATION NAMES(S) AND ADDRESS(S)</b> Air Force Institute of Technology Graduate School of Engineering and Management (AFIT/EN) 2950 Hobson Way WPAFB OH 45433-7765				<b>8. PERFORMING ORGANIZATION REPORT NUMBER</b>  AFIT/GAE/ENY/08-J03	
<b>9. SPONSORING/MONITORING AGENCY NAME(S) AND ADDRESS(ES)</b> AFOSR Dr. Julian Tishkoff 4015 Wilson Blvd. Room 713 Arlington, VA 22203-1954				<b>10. SPONSOR/MONITOR'S ACRONYM(S)</b>  <b>11. SPONSOR/MONITOR'S REPORT NUMBER(S)</b>	
<b>12. DISTRIBUTION/AVAILABILITY STATEMENT</b> APPROVED FOR PUBLIC RELEASE; DISTRIBUTION UNLIMITED.					
<b>13. SUPPLEMENTARY NOTES</b>					
<b>14. ABSTRACT</b> The AFIT Combustion Optimization and Analysis Laser (COAL) lab's modular design and precision diagnostic systems make it an important facility for analyzing combustion processes. The objectives of this research are to install lab enhancements, validate the laser diagnostic system, characterize the igniter for AFIT's Ultra-Compact Combustor (UCC) sections, and perform a laser diagnostic, performance, and video analysis of a flat-cavity UCC section. Laser system validation was accomplished using OH Planar Laser-Induced Fluorescence (PLIF) in a laminar hydrogen-air flame produced by a Hencken burner. Results are compared to previous research. Ratios of intensities and excitation scans in the OH (A-X) (1-0) electronic transition system are used to measure temperature and species concentrations. Igniter characterization was accomplished using open-air flammability and flame height observations to select an operating condition and validated by attaching the igniter to the UCC section. An operating procedure is recommended. A PLIF flame location study using quartz windows on the combustor was performed in the cavity-vane area. Performance measurements and video footage were acquired in order to analyze the system. Results are compared to previous experimental and CFD research. Future work will include two-color PLIF and other laser studies of different locations inside flat- and curved-cavity UCC sections.					
<b>15. SUBJECT TERMS</b> Combustion, Combustors, Experimental Data, Laboratories, Laser Induced Fluorescence					
<b>16. SECURITY CLASSIFICATION OF:</b>		<b>17. LIMITATION OF ABSTRACT</b>		<b>18. NUMBER OF PAGES</b>	
REPORT	ABSTRACT	c. THIS PAGE	UU	169	<b>19a. NAME OF RESPONSIBLE PERSON</b> Major Richard Branam, ENY
U	U	U			<b>19b. TELEPHONE NUMBER (Include area code)</b> (937) 255-3636 x7485,

**Standard Form 298 (Rev. 8-98)**  
Prescribed by ANSI Std. Z39-18